

©2017

Vincent Alexander DeLucca

ALL RIGHTS RESERVED

EVALUATING THE EFFECT OF POWDER OXYGEN CONTENT ON THE
MICROSTRUCTURE AND MECHANICAL PROPERTIES OF SILICON CARBIDE
DENSIFIED BY SPARK PLASMA SINTERING

by

VINCENT ALEXANDER DELUCCA

A dissertation submitted to the
Graduate School – New Brunswick
Rutgers, The State University of New Jersey

In partial fulfillment of the requirements

For the degree of

Doctor of Philosophy

Graduate Program in Materials Science and Engineering

Written under the direction of

Dr. Richard A. Haber

And approved by

New Brunswick, New Jersey

October, 2017

ABSTRACT OF THE DISSERTATION

Evaluating the Effect of Powder Oxygen Content on the Microstructure and Mechanical

Properties of Silicon Carbide Densified by Spark Plasma Sintering

By VINCENT ALEXANDER DELUCCA

Dissertation Director:

Richard A. Haber

Silicon carbide (SiC) is an important material in industry due to its favorable mechanical, thermal, chemical, and electrical properties. While it has been mainly used as an abrasive material in the past, more modern applications like armor and other structural applications, often require densified ceramic bodies. SiC powders can be densified in a number of ways, but one common method is solid-state sintering, either with or without applied pressure. It is well known that in the presence of oxygen, pure SiC will form a passivating oxide layer of silica (SiO₂) on its surface. This poses a problem in sintering as SiO₂ can inhibit the densification of solid state sintered SiC. This thesis examines the effects of varying oxygen content levels in silicon carbide powders on the microstructure and mechanical properties of the resulting densified bodies after solid state sintering via the spark plasma sintering (SPS) method.

Two commercial SiC powders were obtained, characterized, and treated to introduce a range of different oxygen content levels. These powders were then densified via the spark plasma sintering method using boron carbide and carbon additives to produce dense samples. Three series of samples were made using each powder, one varying the amount of carbon added as a particulate, one varying the amount of carbon added as a liquid resin, and one where the oxygen content of the powder was directly manipulated by HF washing, aging, or heat treating.

The dense SiC samples were then characterized to determine the effect of the powder's oxygen content on the microstructure and mechanical properties. The samples were examined using scanning electron microscopy (SEM), electron backscatter diffraction (EBSD), Knoop microhardness testing, and nondestructive ultrasonic evaluation techniques including acoustic spectroscopy and conventional NDE methods.

SEM and EBSD analysis revealed that changes in the powder oxygen content can result in a number of microstructural effects. At intermediate oxygen levels, exaggerated grain growth can occur resulting in large plate-like grains, accompanied by a transformation from the 6H to 4H SiC polytype. At higher oxygen levels, densification may be inhibited and at very high oxygen contents formation of an oxygen rich secondary phase can occur.

Varying the oxygen content of the SiC powder also significantly affects the mechanical properties of the dense ceramic. Ultrasonic measurements of the elastic properties showed a clear decrease in the elastic moduli as the oxygen content is increased. Knoop microhardness measurements show similar behavior with a reduction in hardness with increased powder oxygen content.

Acknowledgements

I would like to thank my advisor, Dr. Richard Haber for all his help, guidance, understanding, and patience over the years. I would also like to thank my committee members, Dr. Matthewson, Dr. Lehman, Dr. Rafaniello, and Dr. Domnich for their help and advice.

Thanks to the members of the Haber group, past and present. After all these years, there are too many grad students, undergrads, and post-docs to name individually, but they have all contributed in one way or another to the work that I've done and made my time here enjoyable. One person I will single out is Michelle Sole. Nothing would ever get done without her, and she was always available to talk about work or life in general.

Thanks to others in the MSE department, particularly Dr. Klein and Claudia Kuchinow for their help navigating through the graduate school bureaucracy, and my other friends and colleagues in the department, especially Dr. Nie for his guidance with formatting.

Financial support from the CCOMC and DARPA made this work possible and is greatly appreciated.

Last, but not least, I would like to thank my family, especially my parents, for their constant support and encouragement.

Table of Contents

ABSTRACT OF THE DISSERTATION	ii
Acknowledgements	iv
Table of Contents	v
List of Tables	xi
List of Figures	xiii
1. Introduction	1
2. Literature Review	2
2.1. Silicon Carbide	2
2.1.1. Properties	2
2.1.2. Structure	3
2.1.3. Production	6
2.1.4. Oxidation	8
2.2. Sintering of Silicon Carbide	9
2.2.1. Solid State Sintering	10
2.2.2. Spark Plasma Sintering	14
2.2.3. Liquid Phase Sintering	16
2.2.4. Reaction Bonding	17
2.3. Ultrasound	17
2.4. Motivation	20

3. Method of Attack	22
3.1. Objective 1: Selection, Treatment, and Characterization of Powders	22
3.1.1. Task 1: Powder Selection.....	22
3.1.2. Task 2: Powder Treatment	23
3.1.3. Task 3: Powder Characterization	24
3.2. Objective 2: Production of Dense SiC Samples	25
3.2.1. Task 1: Selection of Optimum Sintering Conditions.....	25
3.2.2. Task 2: Powder Preparation	27
3.2.3. Task 3: Fabrication of Dense Samples.....	29
3.3. Objective 3: Characterization of Dense Samples.....	29
3.3.1. Task 1: Ultrasound Analysis.....	30
3.3.2. Task 2: Microstructure Characterization	32
3.3.3. Task 3: Mechanical Properties Evaluation	32
3.3.4. Task 4: Data Analysis	33
4. Experimental Procedures	34
4.1. Powder Characterization.....	34
4.1.1. Particle Size Analysis	34
4.1.2. X-Ray Diffraction	34
4.1.3. Electron Microscopy.....	34
4.1.4. Chemical Analysis	35

4.2. Powder Preparation	35
4.2.1. Initial preparation	35
4.2.2. Acid Washing.....	35
4.2.3. Aging.....	36
4.2.4. Heat Treatment.....	36
4.2.5. Mixing.....	36
4.2.6. Drying	37
4.3. Sintering	38
4.3.1. Spark Plasma Sintering	38
4.4. Dense Sample Preparation	38
4.4.1. Sand Blasting and Grinding	38
4.4.2. Sectioning	39
4.4.3. Polishing	40
4.4.4. Ion Milling	41
4.4.5. Etching	42
4.5. Dense Sample Characterization	43
4.5.1. Density Measurements.....	43
4.5.2. Ultrasound Measurements	44
4.5.3. Hardness Testing.....	45
4.5.4. Electron Microscopy	46

4.5.5. Electron Backscatter Diffraction.....	46
4.5.6. X-Ray Diffraction	47
5. Results and Discussion	49
5.1. Selection, Treatment, and Characterization of Powders	49
5.1.1. Powder Selection	49
5.1.2. Powder Treatment.....	49
5.1.3. Powder Characterization	49
5.1.3.1. Chemical Analysis	49
5.1.3.2. X-Ray Diffraction	52
5.1.3.3. Particle Size Analysis	54
5.1.3.4. FESEM Imaging	56
5.2. Production of Dense Silicon Carbide Samples	58
5.2.1. Selection of Optimum Sintering Conditions.....	58
5.2.1.1. HC-SiC Sintering Study.....	58
5.2.1.2. SG-SiC Sintering Study	69
5.2.2. Powder Preparation.....	80
5.2.3. Fabrication of Dense Samples	83
5.2.3.1. Samples Made Using LBC Carbon Source.....	83
5.2.3.2. Samples Made Using PRC Carbon Source.....	83
5.3. Characterization of Dense Silicon Carbide Samples	84

5.3.1. SG-LBC-Series	84
5.3.1.1. Microstructure Characterization	84
5.3.1.2. Mechanical Properties.....	88
5.3.1.3. Ultrasound Analysis.....	91
5.3.2. SG-PRC-Series	92
5.3.2.1. Microstructure Characterization	92
5.3.2.2. Mechanical Properties.....	96
5.3.2.3. Ultrasound Analysis.....	99
5.3.3. SG-AW-Series	100
5.3.3.1. Microstructure Characterization	100
5.3.3.2. Mechanical Properties.....	104
5.3.3.3. Ultrasound Analysis.....	108
5.3.4. HC-LBC-Series.....	109
5.3.4.1. Microstructure Characterization	109
5.3.4.2. Mechanical Properties.....	113
5.3.4.3. Ultrasound Analysis.....	116
5.3.5. HC-PRC-Series	117
5.3.5.1. Microstructure Characterization	117
5.3.5.2. Mechanical Properties.....	121
5.3.5.3. Ultrasound Analysis.....	124

5.3.6. HC-AW-Series	125
5.3.6.1. Microstructure Characterization	125
5.3.6.2. Mechanical Properties.....	130
5.3.6.3. Ultrasound Analysis.....	134
6. Conclusions.....	136
6.1. Microstructure.....	136
6.2. Mechanical Properties.....	138
7. Future Work	141
8. References	143

List of Tables

Table 1. Silicon Carbide Sample Matrix.....	29
Table 2. SiC polishing schedule.....	41
Table 3. Aztec software autolock parameters	47
Table 4. Oxygen contents of powders used to create dense samples.....	52
Table 5. SiC powder initial polytype compositions.....	54
Table 6. RGST Series sintering temperature and dwell time.....	60
Table 7. SPS conditions used for each sample and resulting sample density.....	72
Table 8. Silicon Carbide Sample Matrix.....	80
Table 9. LBC-Series sample compositions	81
Table 10. AW-Series sample compositions	81
Table 11. PRC-Series sample compositions	82
Table 12. SG-LBC-Series average grain sizes measured by the linear intercepts method	86
Table 13. SG-LBC-Series phase fractions	88
Table 14. SG-LBC-Series elastic properties	89
Table 15. SG-PRC-Series average grain sizes measured by the linear intercepts method	94
Table 16. SG-PRC-Series phase fractions	96
Table 17. SG-PRC-Series elastic properties	97
Table 18. SG-AW-Series average grain sizes measured by the linear intercepts method	102
Table 19. SG-AW-Series phase fractions	104
Table 20. SG-AW-Series elastic properties	105

Table 21. HC-LBC-Series average grain sizes measured by the linear intercepts method	111
Table 22. HC-LBC-Series phase fractions.....	113
Table 23. HC-LBC-Series elastic properties	114
Table 24. HC-PRC-Series average grain sizes measured by the linear intercepts method	119
Table 25. HC-PRC-Series phase fractions.....	121
Table 26. HC-PRC-Series elastic properties.....	122
Table 27. HC-AW-Series average grain sizes measured by the linear intercepts method	127
Table 28. HC-AW-Series phase fractions.....	129
Table 29. HC-AW-Series elastic properties.....	130

List of Figures

Figure 1. Stacking of SiC tetrahedra showing parallel (a) and anti-parallel (b) stacking [5]	4
Figure 2. Crystal structures of some common SiC polytypes [6]	5
Figure 3. FESEM image of Saint Gobain SiC powder particles showing the jagged, irregularly shaped morphology typical of Acheson processed SiC	8
Figure 4. Model of the stages of sintering showing (a) initial particle packing, (b) initial stage of sintering, (c) intermediate stage of sintering, and (d) final stage sintering [33]	11
Figure 5. Mass transport mechanisms that do not contribute to densification (a) including (1) evaporation and condensation, (2) Surface diffusion, (3) volume diffusion from surface to neck. Mass transport mechanisms that contribute to densification (b) including (4) grain boundary diffusion, and (5) volume diffusion from grain boundary to neck. [33]	12
Figure 6. Schematic of a typical SPS system [44]	14
Figure 7. Heating effects in the SPS process	15
Figure 8. SPS sample cutting procedure	40
Figure 9. FESEM images of a SiC sample after mechanical polishing (A), and after ion milling (B)	42
Figure 10. Oxygen content growth curves for acid washed and unwashed SG-SiC powder	50
Figure 11. Oxygen content growth curve for acid washed HC-SiC powder	51
Figure 12. SG-SiC powder X-ray diffraction pattern	53
Figure 13. HC-SiC powder X-ray diffraction pattern	54

Figure 14. SG-SiC particle size distribution	55
Figure 15. HC-SiC particle size distribution.....	56
Figure 16. SG-SiC powder micrograph showing primary particles 1 - 3 μ m in size with smaller particle fragments.....	57
Figure 17. HC-SiC powder micrograph showing uniform submicron particle size	58
Figure 18. RGST sample matrix	61
Figure 19. RGST 1 – 4 FESEM images.....	63
Figure 20. RGST 5 – 8 FESEM images.....	64
Figure 21. RGST 8 – 15 FESEM images.....	66
Figure 22. RGST 16 – 20 FESEM images.....	67
Figure 23. RGST 21 – 23 FESEM images.....	68
Figure 24. SPS conditions used for each sample	71
Figure 25. FESEM images of samples sintered with 50 MPa (A), 40 MPa (B), 30 MPa (C), 20 MPa (D), and 10 MPa (E) of applied uniaxial pressure at 5000x magnification	74
Figure 26. FESEM images at 5000x magnification of samples sintered at 1900°C (A), 1925°C (B), 1950°C (C), 1975°C (D), and 2000°C (E) for 5 minutes	76
Figure 27. FESEM images at 5000x magnification of samples sintered at 1900°C for 5 (A), 15 (B), 25 (C), 35 (D), 45 (E), 55 (F), and 65 (G) minutes.....	78
Figure 28. Optimum spark plasma sintering conditions	79
Figure 29. VARCUM phenolic resin TGA data	82
Figure 30. SG-LBC-Series microstructures at 5000x magnification.....	85
Figure 31. SG-LBC-Series EBSD Maps.....	87

Figure 32. SG-LBC-Series elastic properties vs. carbon content	89
Figure 33. SG-LBC-Series Knoop Hardness curves.....	90
Figure 34. SG-LBC-Series Knoop Hardness at 1000 g load	91
Figure 35. SG-LBC-Series ultrasound attenuation spectra.....	92
Figure 36. SG-PRC-Series microstructures at 10000x magnification.....	94
Figure 37. SG-PRC-Series EBSD Maps.....	95
Figure 38. SG-PRC-Series elastic properties vs. carbon content.....	97
Figure 39. SG-PRC-Series Knoop Hardness curves.....	98
Figure 40. SG-PRC-Series Knoop Hardness at 1000 g load	99
Figure 41. SG-PRC-Series ultrasound attenuation spectra.....	100
Figure 42. SG-AW-Series microstructures at 2500x magnification.....	101
Figure 43. SG-AW-Series EBSD Maps.....	104
Figure 44. SG-AW-Series elastic properties vs. oxygen content.....	105
Figure 45. SG-AW-Series Knoop Hardness curves.....	106
Figure 46. SG-AW-Series Knoop Hardness at 1000 g load	107
Figure 47. SG-AW-Series fracture surface images at 5000x magnification (top row) and 1000x magnification (bottom row)	108
Figure 48. SG-AW-Series ultrasound attenuation spectra.....	109
Figure 49. HC-LBC-Series microstructures at 5000x magnification	111
Figure 50. HC-LBC-Series EBSD Maps	113
Figure 51. HC-LBC-Series elastic properties vs. carbon content.....	114
Figure 52. HC-LBC-Series Knoop Hardness curves	115
Figure 53. HC-LBC-Series Knoop Hardness at 1000 g load.....	116

Figure 54. HC-LBC-Series ultrasound attenuation spectra	117
Figure 55. HC-PRC-Series microstructures at 10000x magnification.....	119
Figure 56. Sample HC-PRC-4.5C showing a large cluster of carbon inclusions (5000x and 50000x magnification)	120
Figure 57. HC-PRC-Series EBSD Maps	121
Figure 58. HC-PRC-Series elastic properties vs. carbon content	122
Figure 59. HC-PRC-Series Knoop Hardness curves	123
Figure 60. HC-PRC-Series Knoop Hardness at 1000 g load.....	124
Figure 61. HC-PRC-Series ultrasound attenuation spectra.....	125
Figure 62. HC-AW-Series microstructures at 5000x magnification	127
Figure 63. EDS maps of HC-AW-3.36% showing oxygen rich second phase.....	128
Figure 64. HC-AW-Series EBSD Maps	129
Figure 65. HC-AW-Series elastic properties vs. oxygen content	131
Figure 66. HC-AW-Series Knoop Hardness curves	132
Figure 67. HC-AW-Series Knoop Hardness at 1000 g load.....	133
Figure 68. HC-AW-Series fracture surface images at 5000x magnification (top row) and 1000x magnification (bottom row)	134
Figure 69. HC-AW-Series ultrasound attenuation spectra	135

1. Introduction

Silicon carbide (SiC) is an important material in industry due to its favorable mechanical, thermal, chemical, and electrical properties. While it has been mainly used as an abrasive material in the past, more modern applications like armor and other structural applications, often require densified ceramic bodies. SiC powders can be densified in a number of ways, but one common method is solid-state sintering, either with or without applied pressure. It is well known that in the presence of oxygen, pure SiC will form a passivating oxide layer of silica (SiO_2) on its surface. This poses a problem in sintering as SiO_2 can inhibit the densification of solid state sintered SiC. Evidence also suggests that elevated levels of oxygen on the surface, present as SiO_2 , can lead to exaggerated, anisotropic grain growth in silicon carbide containing boron carbide and carbon additives densified by spark plasma sintering (SPS).

This thesis examines the effects of varying oxygen content levels in silicon carbide powders on the microstructure and mechanical properties of the resulting densified bodies after solid state sintering via the SPS method. Several SiC powders were obtained, characterized, and treated to introduce a range of different oxygen content levels. These powders with varying oxygen contents were densified via the spark plasma sintering method using boron carbide and carbon additives to produce samples with different microstructures. The densified samples were then characterized to determine the effect of the powder's oxygen content on the microstructure and mechanical properties. The samples were subjected to a full range of characterization techniques, including chemical analysis, SEM, XRD, EBSD, and nondestructive ultrasonic evaluation including acoustic spectroscopy and conventional NDE methods.

2. Literature Review

2.1. Silicon Carbide

Silicon carbide was first mass produced by Acheson in the late 1800's [1] and has been used in many industrial applications ever since. First used mainly as an abrasive, in the years since SiC has become widely used in a number of different applications such as refractories, heating elements, wear resistant parts, structural ceramics, lightweight mirrors for use in aerospace applications, electronic devices and semiconductors, and even as an armor ceramic. Many of these more specialized uses require SiC that is high in purity and near full density in order to take advantage of its unique mechanical, electrical, and thermal properties.

2.1.1. Properties

Silicon carbide is notable for its excellent mechanical properties and many of its most common uses take advantage of these properties. Silicon carbide has high hardness, strength, and elastic moduli [2], with a relatively low theoretical density of 3.21 g/cm^3 , less than half that of typical steel alloys. This combination of properties makes silicon carbide desirable as a structural material. Silicon carbide does not melt and has a high sublimation temperature as well as a very low thermal expansion coefficient of $3.3 \times 10^{-6}/\text{K}$, making it useful as a material in high temperature applications. SiC is also highly inert and resistant to chemical attack. The combination of these properties makes silicon carbide useful in such environments as kiln furniture and diesel particulate filters. A great deal of effort was put into developing silicon carbide as a material for use in high temperature dynamic environments such as gas turbine blades and engine components, but these efforts never really panned out because of the low fracture toughness of silicon

carbide.[3] As a brittle ceramic material, if silicon carbide fails, it will fail suddenly and catastrophically. Because of this, the dynamic environments where silicon carbide is used are limited to applications where this behavior is acceptable, such as in personnel and vehicle armor, or where the risk is minimal, such as in seals and wear parts. Silicon carbide is also a semiconductor and has been used in a number of electronic applications such as LEDs and transistors, and due to its high thermal conductivity, it is of interest for high power electronics applications.[4]

2.1.2. Structure

The properties of silicon carbide arise from the crystal structure of the material. The structure of the silicon carbide lattice consists of layers of hexagonally packed atoms, alternating between layers of carbon atoms and silicon atoms. Another way of looking at this would be as a close packed lattice of Si-C tetrahedra, where one atom of Si is bonded to four C atoms or vice versa. The vertices of each of these Si-C tetrahedra are shared with their neighbors and repeating stacks of these tetrahedra form the crystal structure of SiC.[5] The tetrahedra can be stacked such that the bases are either parallel or anti-parallel. This is shown below in Figure 1.

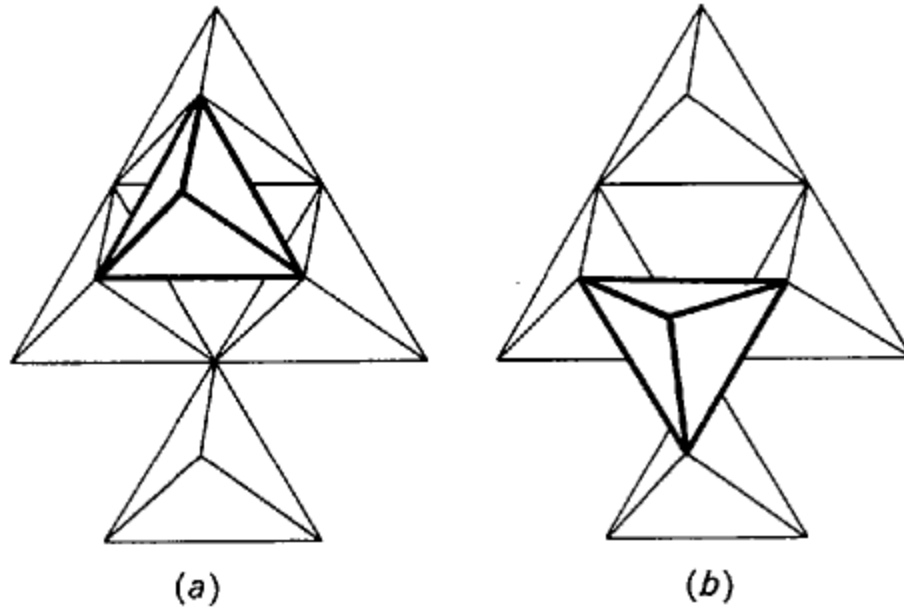


Figure 1. Stacking of SiC tetrahedra showing parallel (a) and anti-parallel (b) stacking [5]

Depending on how the tetrahedra are stacked SiC will form a number of differently ordered crystal structures with the same stoichiometry, or polytypes. These polytypes are typically described using Ramsell notation which uses a number to describe the number of tetrahedral layers in the unit cell, and a letter to describe the crystal symmetry. A few common examples would be 3C, 6H, and 15R, where C refers to a cubic structure, H refers to a hexagonal structure, and R refers to a rhombohedral structure. The 3C polytype is the only cubic polytype and is known as β -SiC, while the rest of the hexagonal and rhombohedral polytypes are collectively known as α -SiC. The crystal structures of some selected SiC polytypes are shown below in Figure 2.

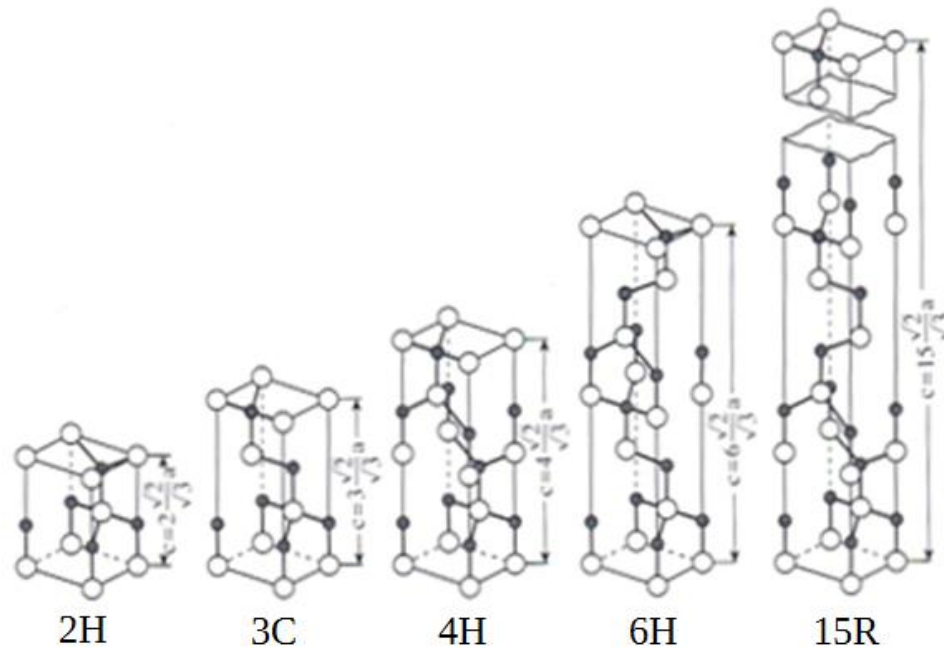


Figure 2. Crystal structures of some common SiC polytypes [6]

Which polytype of SiC is present is usually determined by the temperature at which the material was produced. The shorter period polytypes like 2H and 3C are stable at lower temperatures while higher period polytypes like 6H and 15R are more stable at higher temperatures.[7] As such, the method used for powder production will have a great effect on the polytype content. Additionally, the impurity content can also influence the polytype of the produced silicon carbide.[8]

The different polytypes of silicon carbide can be distinguished in a number of ways, but the most common is by x-ray diffraction methods. Due to the similarity in structure between the different polytypes, x-ray peaks often overlap making quantitative analysis difficult. There are some simple x-ray methods for using relative peak intensities to calculate the polytype concentrations, but more complex methods like Rietveld refinement and Raman spectroscopy can give more accurate results. [9-13]

During the firing process, as silicon carbide is exposed to high temperatures and possibly different dopants, the original polytype(s) present in the powder can transform into other forms that are more stable in that environment. This transformation process is often accompanied by exaggerated, anisotropic grain growth. This is commonly seen in the sintering of the lower temperature β -SiC, where it transforms to the higher temperature α -SiC, and typically displays microstructures with large, elongated grain structures.[14-18] Additionally, impurities or dopants can cause transformations between the various SiC polytypes. It has been shown that doping with group III elements like boron or aluminum can stabilize hexagonal polytypes while doping with group V elements like nitrogen can stabilize the cubic structure.[19]

2.1.3. Production

Silicon carbide is produced in a number of different ways for a number of different purposes.[7] The most common method is by the Acheson process, where silica and carbon are mixed and heated using a graphite electrode at high temperatures for long periods of time.[1] The precursor materials react to form silicon carbide by the following reaction:



This process typically results in huge ingots of several tons or more which are then separated by purity or crystallinity and crushed to size. The purity and polytype composition of the ingot will vary with distance from the electrode and the accompanying difference in temperature. Material closer to the electrode will be higher in purity while materials from further away will be lower in purity and may contain some unreacted precursor materials. Due to the high temperatures involved, the Acheson

process typically produces primarily 6H polytype SiC with some smaller amounts of other polytypes.[7]

Other methods for producing SiC include the carbothermal reduction of silica to form β -SiC powders, siliconization of carbon, chemical vapor deposition processes, liquid phase methods, and various single crystal growth methods.[7] However, these methods tend to be much more expensive or too small in scale so the Acheson process remains the preferred method for large scale production.

Powders produced by the Acheson process are available commercially over a wide range of particle sizes and specific surface areas. Due to the crushing process, the morphology of these powders tends to be quite jagged and irregularly shaped. A scanning electron micrograph of a typical SiC powder produced by the Acheson process is shown below in Figure 3 highlighting this type of morphology.

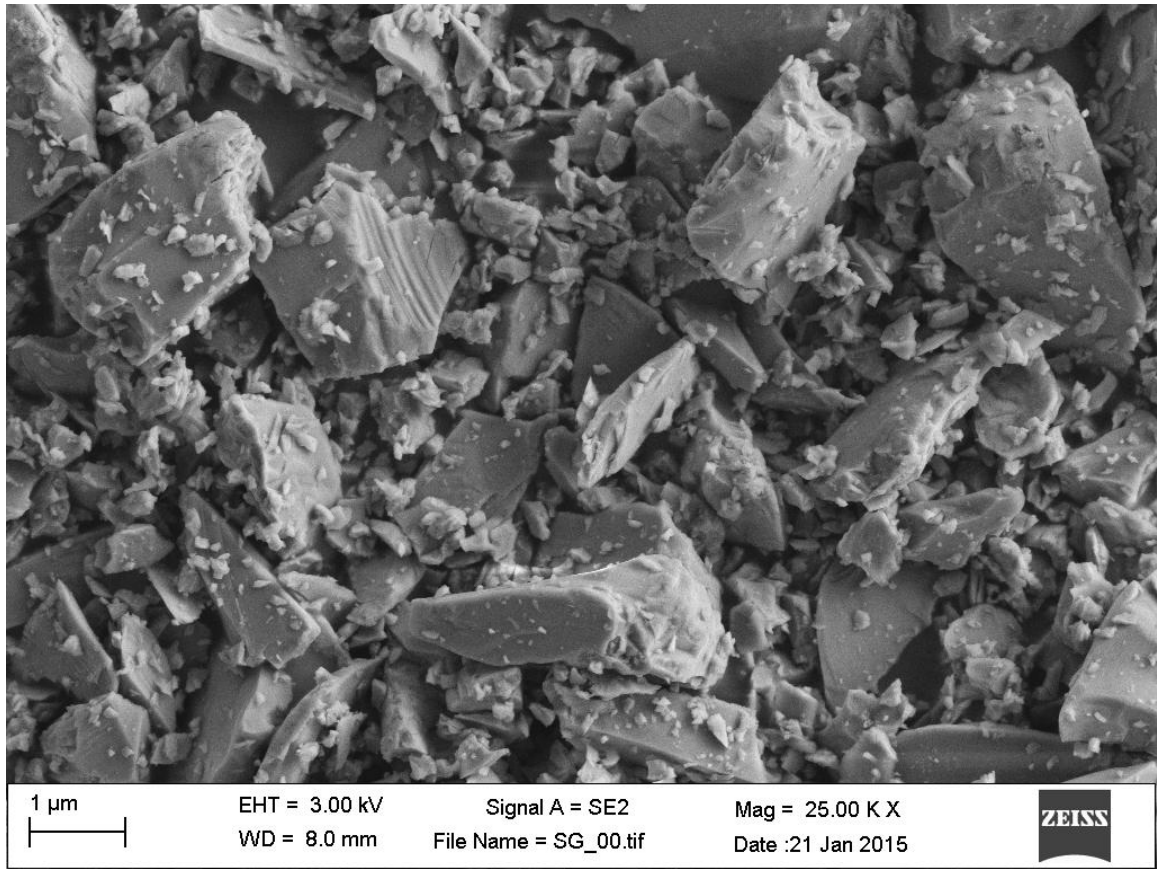


Figure 3. FESEM image of Saint Gobain SiC powder particles showing the jagged, irregularly shaped morphology typical of Acheson processed SiC

2.1.4. Oxidation

Like many non-oxide ceramics, including B_4C , TiB_2 , Si_3N_4 , SiC will react to form an oxide passivating layer on its surfaces when exposed to oxygen. In the case of silicon carbide, silicon dioxide, or silica (SiO_2), is the species that forms this layer. The amount of silica that forms and the speed at which it accumulates is dependent on the size of the SiC particle.[20] While most studies on the oxidation behavior of SiC have been conducted at high temperatures,[21] the oxidation process still occurs at lower temperatures, just not as quickly. The passive oxidation of silicon carbide is controlled by the diffusion of oxygen through the thin oxide layer on the SiC surface.[22, 23] At low

temperatures, the process is dominated by transport of O_2 molecules through this layer while at higher temperatures, above 1300°C , transport of ionic oxygen becomes more important.[24, 25]

The oxygen content of non-oxide ceramics can also increase during processing. Even when processed in an “ideally inert” environment, oxidation can occur. This was shown to occur in the milling of fine TiB_2 powders, where the oxygen content of the powder increased significantly after milling even when conducted in a nonpolar organic solvent in an inert gas environment.[26]

There are several ways to remove the oxide layer from the surfaces of silicon carbide. One of the most common ways to do this is by etching using hydrofluoric acid. Several studies have been conducted on etching of SiO_2 on SiC wafer surfaces for semiconductor applications.[27-30] While some of these studies have shown that the oxide grown on different SiC polytypes and crystal faces will etch at the same rate in HF,[27] these factors do play a role in the final surface chemistry.[28] When comparing the etching of SiO_2 films on SiC and Si surfaces, Correa found that while the etching rates were the same for both, the SiC surfaces had much higher residual oxygen content and attributed this to the presence of silicon oxycarbides present at the SiC- SiO_2 interface region.[30]

2.2. Sintering of Silicon Carbide

In order to take advantage of the unique properties of silicon carbide for practical uses, it is often necessary to produce large, dense bodies. While large pieces can be made using CVD processes or single crystal growth methods, it is generally easier and cheaper to make silicon carbide parts by sintering powders.

Sintering is the coalescence of a powder material by diffusional processes by firing at an elevated temperature.[31] Thus, the powder particles become joined together to form a single body with some finite strength. In general, sintering implies that the body has densified, but that is not always the case as in the sintering of porous refractories for insulation purposes.[32] There are a number of ways to sinter silicon carbide, including solid state sintering, liquid phase sintering, and reaction bonding. Included in these ways are a number of methods, for example, normal pressureless sintering, hot pressing, or spark plasma sintering. In this work, silicon carbide will primarily be densified by solid state sintering using the spark plasma sintering method. As such, more background will be presented on these topics and only a brief overview will be provided on liquid phase sintering and reaction bonding.

2.2.1. Solid State Sintering

Solid state sintering is when consolidation occurs without any component of the system melting. Sintering in the solid state occurs in three main stages. In the initial stage, the powder particles smooth and begin to form necks between adjacent particles. Pores begin to become rounded, but remain open and interconnected. In the intermediate stage, significant densification begins as matter diffuses towards the pore channels and the pore volume shrinks. In the final stage of sintering, the pores close off and become isolated while slowly shrinking and ideally disappearing. At this stage, significant grain growth can also occur. Figure 4 shows a model description of the three stages of sintering. Normal solid state sintering of SiC is generally conducted under vacuum or in an inert atmosphere without any applied pressure. Solid state sintering can also be

conducted with applied pressure, as in hot pressing, hot isostatic pressing, or spark plasma sintering, which enhances desiccation.

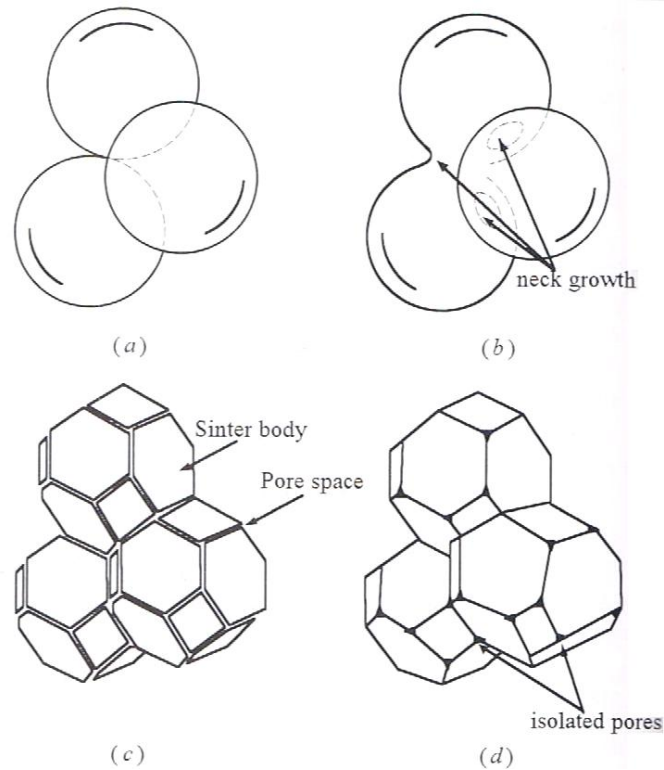


Figure 4. Model of the stages of sintering showing (a) initial particle packing, (b) initial stage of sintering, (c) intermediate stage of sintering, and (d) final stage sintering [33]

Mass transport occurs by diffusion and is driven by the decrease in free energy associated with reduction in surface area and the replacement of solid-gas interfaces with solid-solid interfaces. A number of diffusion mechanisms are possible, including surface diffusion, evaporation and condensation, grain boundary diffusion, lattice diffusion, and plastic flow.[32] Surface diffusion and evaporation-condensation do not contribute to densification and can cause coarsening, where larger particles grow at the expense of smaller ones without decreasing pore volume. The other mechanisms of grain boundary diffusion and lattice diffusion do contribute to volume shrinkage, while plastic flow is

effective densification mechanism when an external pressure is applied. A schematic of the various mass transport mechanisms during the sintering process is shown in Figure 5.

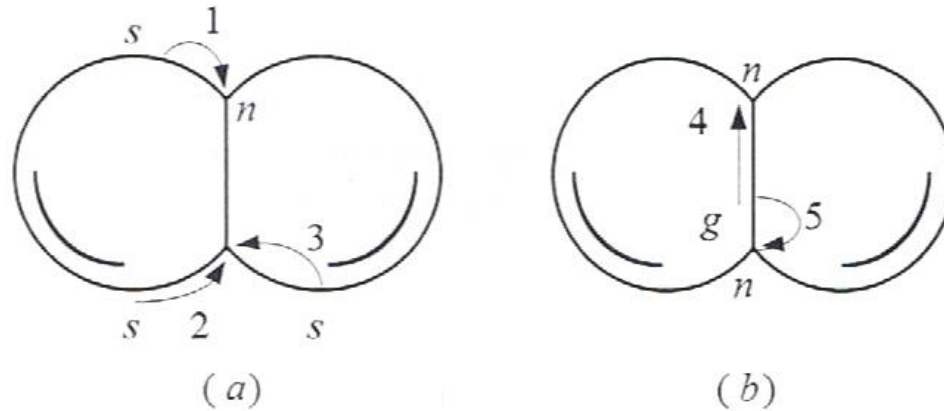


Figure 5. Mass transport mechanisms that do not contribute to densification (a) including (1) evaporation and condensation, (2) Surface diffusion, (3) volume diffusion from surface to neck. Mass transport mechanisms that contribute to densification (b) including (4) grain boundary diffusion, and (5) volume diffusion from grain boundary to neck. [33]

The SiO_2 layer present on the surfaces of SiC powders can inhibit the densification of solid state sintered SiC, especially in pressureless sintering. SiC can react with the SiO_2 resulting in the formation of Si, SiO, and CO vapors.[34] This can fracture interparticle necks and lead to coarsening rather than densification.[35] These effects can be remedied by removing the oxide surface layer, either by treating the powder to remove the oxygen beforehand, or by removing the oxide during the sintering process. This is typically done by adding carbon and holding for a period of time at an intermediate temperature under vacuum to reduce the SiO_2 and remove the oxygen as CO gas by the same reaction as in Equation 1.

Because of the highly covalent nature of silicon carbide and the resulting low self diffusion coefficients, it is difficult to densify pure SiC and often requires sintering aids

to fully densify under practical conditions.[36] Pioneering work by Prochazka in the 1970s first demonstrated solid state sintering of silicon carbide to near theoretical density was possible by the addition of boron and carbon.[37] Common additives used as sintering aids in solid state sintered silicon carbide include aluminum or aluminum containing compounds, boron or boron containing compounds, carbon, and other metals and metal oxides including Fe, Ca, Li, Cr, etc.[7, 38, 39] The boron containing species serve to enhance diffusion mechanisms that promote densification and create vacancies which increase the self diffusion coefficients of Si and C.[40] Carbon additives serve to remove the SiO₂ layers on the SiC surfaces preventing SiC from reacting with the SiO₂, enhances bulk self diffusion, and may play a role in preventing large grain growth by forming inclusions.[34, 35, 41-43] Aluminum functions as a sintering aid in much the same way as boron,[36] although adding too much can cause the formation of a liquid phase.

In his work on the effects of carbon and boron on the sintering of silicon carbide, Stobierski concluded that carbon serves to block the mass transport mechanisms that are ineffective in densification and prevents grain growth.[34] He also found that there were three regimes in which the effects of boron additions are different.[40] At very low concentrations, boron is not very effective because of the competing processes of dissolution of boron into the SiC and activation of transport mechanisms. In the optimal concentration range of 0.2 – 0.5%, boron will lead to the highest densification in the solid state without exaggerated grain growth. Above this concentration range, their samples showed evidence of the formation of a liquid phase and was accompanied by exaggerated grain growth.

2.2.2. Spark Plasma Sintering

Spark plasma sintering (SPS), also known as FAST (field assisted sintering technique), EFAS (electric field assisted sintering), or DCS (direct current sintering), is a process by which direct current and uniaxial pressure are applied to a powder compact in a conductive die set to induce sintering.[44] The advantages of SPS over other traditional sintering methods are that it can sinter materials at lower temperatures and with shorter hold times.[45] It has been shown that SPS is effective at producing dense silicon carbide more quickly and at lower temperatures than pressureless sintering and hot pressing.[46] This is desirable as it can limit grain growth in the final stage of sintering. A diagram of the SPS system is shown in Figure 6 and the heating mechanisms are shown in Figure 7.

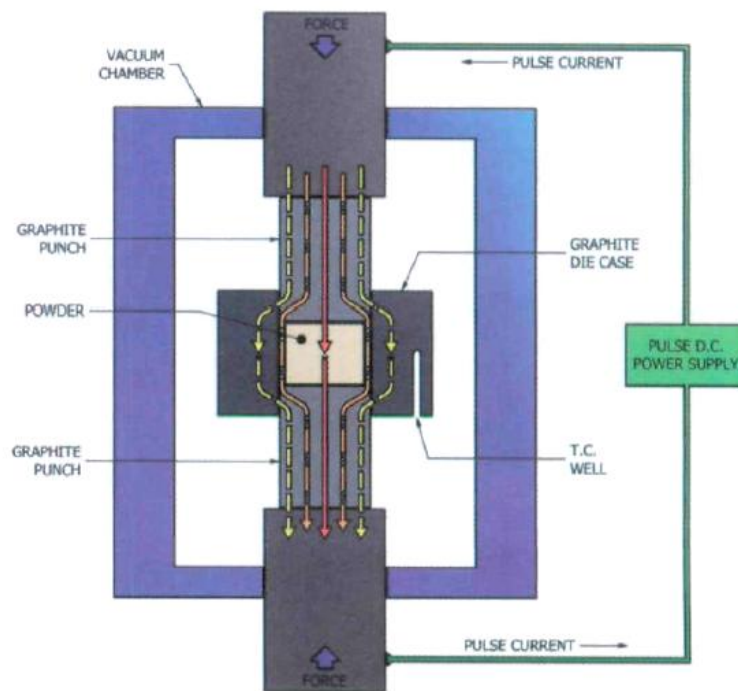


Figure 6. Schematic of a typical SPS system [44]

Many researchers have shown that it is possible to fully densify both α - and β -SiC by the SPS method. Yamamoto showed that the SPS method could be used to densify

pure β -SiC without additives and retain a nanoscale grain size.[47] Maitre and coworkers showed that commercial α -SiC powders sintered with boron and carbon additives had higher densification rates without abnormal grain growth.[48] In their study, Zhou, et al, found that both oxide and nonoxide additives were effective dopants when sintering sub-micron α - and β -SiC powders.[49]

Heating of the sample in SPS occurs mainly by Joule heating, also known as resistive heating. The conductive die and punches heat as current is passed through them, and this heat is transferred to the powder inside. Joule heating also occurs in the powder itself as current passes between conducting particles. Because Joule heating can support much higher heating rates than induction or convection heating, SPS processing times can be much shorter than normal sintering or hot pressing, making SPS much more convenient for quick lab-scale work.[44, 46]

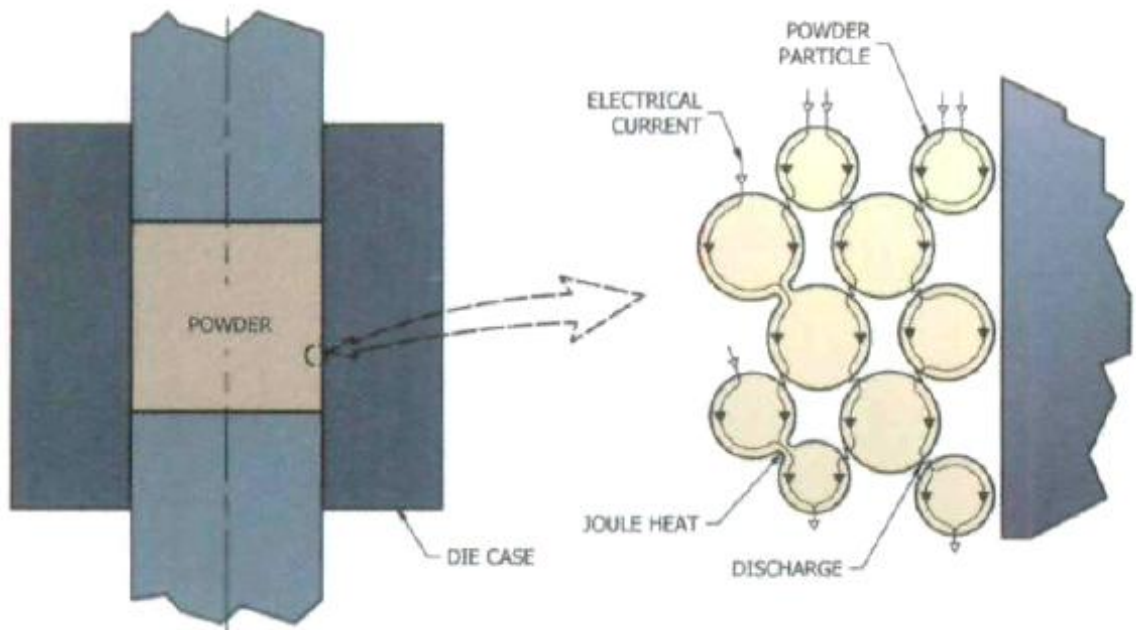


Figure 7. Heating effects in the SPS process

When the spark plasma sintering method was first developed by Inoue in the 1960s, [50, 51] it was thought that the applied direct current caused plasma formation and/or sparking between powder particles, hence the name, which would facilitate heating and densification. More recent studies have found little evidence for this and have essentially disproven the existence of sparking or plasma in SPS, [52-55] though the name has stuck.

2.2.3. Liquid Phase Sintering

Liquid phase sintering (LPS) is when components are added to the system that will melt at a lower temperature than the matrix phase. When heated, the additives melt and capillary forces draw the liquid into pores and sharp particle edges can dissolve enabling the matrix phase particles to rearrange into a closer packed structure.[33] Densification occurs initially by particle rearrangement, followed by solution and reprecipitation through the liquid phase, and finally by solid phase sintering of the rigid skeleton.[32, 33, 56] Depending on the amount of liquid phase additives, the final microstructure can have the liquid forming phase isolated at the grain junctions or as an interconnected phase along the grain boundaries. Some common liquid forming additives used in LPS of silicon carbide include Al_2O_3 , Y_2O_3 , and other rare earth oxides.[7, 57] When using oxide additives in LPS, the silica layer on the surfaces of the SiC particles will not inhibit densification as it does in solid state sintering since it reacts with the other oxide additives to help form the liquid phase.[7] Like solid state sintering, LPS can also be conducted with applied pressure by hot pressing, hot isostatic pressing, or spark plasma sintering.

2.2.4. Reaction Bonding

Reaction bonding is a process by which a porous preform is densified by chemically reacting it with another component to form a dense body of the desired material.[58] In the case of reaction bonded silicon carbide, a porous preform of graphite or a graphite and SiC mixture is infiltrated with molten silicon. The silicon reacts with the graphite to form silicon carbide. The benefits of this method are that parts can be made in complex shapes with almost zero change in dimensions from the preformed piece.[58] Although this process results in a dense body, there is usually a significant amount of free silicon left over, making these materials unsuitable for very high temperature applications.[36] Because machining of the porous preform is much easier than machining dense SiC, the reaction bonding process is useful for making SiC parts with more complex shapes than traditional sintering methods. This is exemplified by the use of this method in producing mirrors for high energy laser and space based applications.[59]

2.3. Ultrasound

One of the characterization techniques that will be used in this thesis is ultrasound nondestructive evaluation (NDE). Ultrasound NDE uses high frequency ultrasonic sound waves to probe the material. This technique is well established for determining the elastic properties and locating large flaws in a wide range of materials and ASTM standards have been established for these methods.[60, 61]

Because the ultrasound wave passes through and interacts with the bulk of the material under investigation, there is the potential for ultrasound to be used as a more detailed characterization technique. As the ultrasound wave travels through the material, it attenuates, that is, it loses energy, by various mechanisms. Different types of

microstructural features will have different attenuation mechanisms. For example, small second phase inclusions will cause attenuation by thermoelastic absorption while the matrix phase grains will tend to attenuate the ultrasound by scattering.

These different attenuation mechanisms will be active over different ultrasound frequencies as well, depending on the material properties of the features causing the attenuation. By measuring the attenuation over a wide range of frequencies, it is possible to generate an attenuation spectrum and this technique is called acoustic spectroscopy. This technique had been extensively used for many years in colloidal suspensions, but had not been widely applied to dense ceramic materials.

In their work at Rutgers, Portune and Bottiglieri demonstrated the potential for ultrasound to be used as a method for characterizing the microstructure of dense ceramic materials.[62, 63] They demonstrated the feasibility of using ultrasound acoustic spectroscopy to measure grain size and secondary phase particle size distributions in silicon carbide and aluminum oxide ceramics, respectively. In doing so, they showed that ultrasound could potentially be used as a tool to nondestructively characterize the microstructures of dense ceramic materials.

In their work, Portune and Bottiglieri showed that in dense ceramic materials, there are two primary attenuation mechanisms – thermoelastic absorption and scattering. Thermoelastic absorption is caused by small temperature differences created by the propagating acoustic wave and treats particles as damped driven harmonic oscillators. In the case of dense ceramics like silicon carbide and aluminum oxide, this type of attenuation is primarily caused by second phase particles in the microstructure pinned by the primary phase matrix. Scattering attenuation occurs in an analogous fashion to light

scattering and is primarily caused by the primary phase grains in three regimes: Rayleigh scattering, stochastic scattering, and diffuse scattering. Rayleigh scattering occurs when the scattering features, i.e. the primary phase grains, are much smaller than the wavelength of the ultrasound in that material. Stochastic scattering is dominant when the length scale of the scattering features is on the same order as the wavelength, and diffuse scattering is dominant when the scattering features are much larger than the wavelength.

The attenuation due to scattering is given by [64]

$$\alpha = C_R a^3 f^4 \quad \text{Equation 2a}$$

$$\alpha = C_S a f^2 \quad \text{Equation 2b}$$

$$\alpha = C_D a^{-1} f^0 \quad \text{Equation 2c}$$

for Rayleigh, stochastic, and diffuse scattering respectively, where α is the attenuation coefficient, C_i ($i = R, S$, or D) is a constant that is determined by the properties of the system, a is the average scattering feature size (average grain size), and f is the ultrasound frequency.

In equations 2a – c, it is assumed that the scattering features are spherical, while in reality, the grains of a polycrystalline material are not. In some cases, like the alumina materials Bottiglieri studied, it is a reasonable assumption as the grains are typically equiaxed with a narrow grain size distribution. However, in materials that show grains that are not equiaxed, this assumption does not hold. Under certain conditions, silicon carbide materials can show extremely anisotropic grain growth, resulting in very high aspect ratio grains. Thus, in order to determine the scattering constants in the SiC system, it is important to be able to tune the microstructures to generate equiaxed grains of varying sizes.

2.4. Motivation

While most SiC producers are content to just remove all of the oxygen from their parts before or during firing, few studies have actually examined the effects of the powder oxygen content on the microstructure and properties of the resulting silicon carbide bodies. Work at Rutgers has shown that exaggerated, anisotropic grain growth can occur in SiC even at relatively low firing temperatures. This phenomenon has been attributed to the transformation of 6H polytype SiC grains to 4H polytype during the firing process.[65]

In pressureless sintering studies, Tanaka *et al.* claimed that this transformation was caused by metal impurities, specifically aluminum, in the powder.[66] In their study, they sintered three different 6H SiC powders with varying size and impurity levels with B and C additions. They observed that the powder with the greatest aluminum content showed larger, elongated grains than the other powders. However, the powder that showed this effect also had a greater SiO₂ content.

In a study by Maitre, it was shown that α -SiC powders sintered by SPS with only boron carbide as an additive showed abnormal grain growth with lath-like texture.[48] They claimed that the boron carbide additive reacted with the native oxide layer on the surfaces of the silicon carbide powder to form a vitreous borosilicate phase. This resulting liquid phase would result in enhanced grain growth kinetics by solution and precipitation which may have led to the abnormal grain growth they observed.

This effect of exaggerated grain growth has been observed in some cases and not others, at Rutgers in parts made with the same SiC powders, which should have the same impurity contents. Knippenberg also showed that there was no clear correlation between

aluminum impurity content and structure in crystals grown at fixed temperatures.[19] Additionally, examination of SiC samples by SEM at Rutgers and TEM at Johns Hopkins has not shown any clear evidence of borosilicate glassy phase inclusions. EBSD analysis has shown that, while the samples that show exaggerated grain growth do contain a much higher ratio of 4H to 6H SiC, the elongated grains themselves can be of either polytype. Anecdotal evidence also suggests that SiC powders may have a “shelf life,” with parts made with older powders sintering to lower densities than those made with fresh powders. This suggests that the cause of the 6H to 4H transformation and associated exaggerated grain growth could be the oxygen content of the powder.

3. Method of Attack

The aim of this thesis was to understand the role of oxygen content in silicon carbide powders on the microstructure, hardness, and elastic moduli of dense, solid state sintered silicon carbide materials produced by the spark plasma sintering method. In meeting this goal, three primary objectives had to be completed. First, several silicon carbide powders had to be obtained, characterized, and treated to introduce a range of different oxygen content levels. Then these powders were solid state sintered via the spark plasma sintering method using boron carbide and carbon additives to produce dense samples with varying microstructures and mechanical properties. Finally, the densified samples were characterized using a number of different techniques to determine what effects the powder oxygen content has on the microstructure and mechanical properties of silicon carbide produced in this manner.

3.1. Objective 1: Selection, Treatment, and Characterization of Powders

In order to examine the role of the oxygen content of silicon carbide powders on the properties of dense bodies made using them, powders with varying oxygen contents had to be obtained. This objective was split into three separate tasks: the selection of starting powders, the treatment of these powders to change the oxygen content, and the characterization of these powders.

3.1.1. Task 1: Powder Selection

For this thesis, two commercial silicon carbide powders obtained from H.C. Starck and Saint Gobain were investigated. These powders were chosen for their similar processing histories as they are both Acheson processed materials that were then ground to size. The primary difference between these powders was in the particle size and the

condition in which they were received. The H.C. Starck powder was received as a dry powder, while the Saint Gobain powder was coarser and was acid washed in a proprietary process and arrived as a wet slurry which inhibited oxygen growth.

3.1.2. Task 2: Powder Treatment

Prior to this study, the silicon carbide powders had been in storage for a long period of time. In the case of the H.C. Starck powder, which had been stored without any special considerations for years, the oxygen content was measured to be relatively high at 1.69%. For the Saint Gobain powder, which was stored as a slurry in water, the oxygen content after drying was measured to be quite low at 0.22%. To modify the amount of oxygen present on the surface of the SiC powder particles, the powders were treated in three different ways – acid washing, aging, and heat treatment.

To reduce the oxygen content, the powders were treated with hydrofluoric acid. This acid washing process removes the native oxide layer from the particle surfaces and thereby lowers the oxygen content of the powder. In the acid treatment process, 30 g of silicon carbide powder is mixed with 100 mL of 50% HF solution (48 – 51% solution, Acros Organics). This mixture is then stirred for one hour in a Nalgene HDPE beaker using a Teflon coated magnetic stir bar. Afterwards, the mixture is neutralized with ammonium hydroxide (reagent ACS grade, Acros Organics) until it reaches a pH of 7. The silicon carbide is then washed with deionized water and centrifuged to separate the silicon carbide from the water. The water is removed and this washing step is repeated three more times and the powder is dried.

After washing the powders with hydrofluoric acid, they should have the lowest possible oxygen content. To create powders with oxygen contents in the range between

the pre-treatment maximum and post-washing minimum, some of the washed powders were aged to reintroduce oxygen to the powder surfaces. A powder aging study was conducted in order to determine how quickly the oxide layer reforms on the powder surfaces. To accomplish this, the washed powders were left in air. At varying intervals of time, powder samples were taken and analyzed to determine the oxygen content and an oxidation time curve was established.

To increase the oxygen content above the baseline level, the powders were either aged or heat treated. As the Saint Gobain powder was stored wet, it could be dried and aged to increase the oxygen content. After drying, the oxygen content of the SG-SiC powder would increase over the course of a few days to a 0.30% when stored in room temperature air. As the HC-SiC had been stored in this way for years already, the room temperature aging had no effect. When stored in a drying oven in air at 100°C, the oxygen content of the SG-SiC powder would rise over the course of several months to an increased level of 0.38%.

The heat treatment of the powders was conducted by heating the powder in a tube furnace at 600°C over night with the end caps removed so that air could flow through during the treatment. Approximately 50 grams of each powder was treated in this way. After heat treatment the oxygen content increased to 0.98% for the SG-SiC powder and 3.36% for the HC-SiC powder.

3.1.3. Task 3: Powder Characterization

To quantify the differences between the SiC powders, a full range of powder characterization tests were conducted both before and after the acid treatment and aging steps. Chemical analysis of the powders was performed using a LECO TC600

oxygen/nitrogen analyzer to determine the powder oxygen content. XRD analysis using a PANalytical X-Pert x-ray diffractometer was used to determine the initial polytype compositions of the two SiC powders. Particle size was measured by dynamic light scattering using a Malvern Mastersizer 2000 with Hydro 2000S cell. FESEM image analysis was also performed on the powders to confirm the measured particle sizes and to examine the morphology of the powder particles.

Powder characterization was also conducted on the boron carbide and carbon additives. The boron carbide powder that was used is a commercial powder, H.C. Starck HD20, while one of the carbon additives that was used is a lamp black supplied by Fisher Scientific. These powders were chosen for their ease of use and availability.

3.2. Objective 2: Production of Dense SiC Samples

To examine the role of the oxygen content of silicon carbide powders on the properties of dense bodies made using them, the powders with varying oxygen contents had to be densified. This objective can be split into three tasks: the selection of the optimum sintering conditions, powder preparation, and the fabrication of samples using the optimal conditions.

3.2.1. Task 1: Selection of Optimum Sintering Conditions

To isolate the effect of the powder oxygen content on the microstructure and mechanical properties of dense silicon carbide samples, they must be made in such a way as to minimize the effects of other variables. Because the conditions during sintering play a large role in determining the microstructural properties of silicon carbide materials, the sintering conditions should be kept constant for all samples. The chosen sintering conditions should be able to fully densify the different silicon carbide powders while

limiting grain growth. In light of these requirements, a sintering study was conducted where samples of each powder were densified using varying time, temperature, and pressure profiles in order to find the optimal SPS sintering parameters for producing dense samples with both powders. These samples used the baseline composition of 0.5% B₄C and 1.5% C additions.

After completion of this sintering study, the optimal SPS parameters that were selected are as follows. The samples were densified in a Thermal Technology SPS 10-4 spark plasma sintering unit in a 20 mm graphite die lined with graphite foil. The temperatures of the samples in the SPS were measured using an optical pyrometer aimed at a hole drilled into the side of the graphite die. Because the pyrometer cannot detect temperatures lower than about 550°C, each sintering cycle started by ramping up to 600°C and 10 MPa of pressure and holding there until the pyrometer started to read the actual temperature of the die. The samples were then heated under vacuum to an intermediate dwell temperature of 1400°C at 200°C per minute, ramping up to 50 MPa of uniaxial pressure at 10 MPa per minute and holding for 30 minutes. After this intermediate dwell step, the chamber will be backfilled with argon. The furnace is then ramped to 1900°C at 200°C per minute and held at that temperature for 15 minutes, maintaining 50 MPa of pressure. Afterwards, the power supplies are shut off and the sample allowed to cool for 30 – 45 minutes so that it can be safely removed from the unit. For samples made with phenolic resin as the carbon source, an additional dwell step was added for 30 minutes at 800°C and 20 MPa in order to burn out the phenolic resin and convert it to carbon.

3.2.2. Task 2: Powder Preparation

After the powders were treated to adjust the oxygen content and characterized, they were prepared for sintering. The powders were prepared by first mixing the SiC powder with the boron carbide and carbon additives. Two different types of carbon additives were used – the particulate lampblack, and a liquid phenolic resin (VARCUM 29353, Durez Corp.). The SiC was combined with 0.5% by weight of boron carbide, and varying amounts of carbon between 0% and 4.5%. The combined powders were then mixed by ball milling in ethanol for 24 hours in a polyethylene container with silicon carbide media. After milling, the powders were sieved to remove the ball mill media, dried, and ground to uniformity with a mortar and pestle. Afterwards, oxygen measurements were again taken to see how much of an effect the powder preparation process has on the oxygen content.

To examine the effects of oxygen content, the amount of oxygen had to be manipulated between different samples. There are two main ways of doing this – the oxide can be removed prior to sintering or it can be removed during sintering. Removing the oxide before sintering involves the acid washing procedure described previously. Removing the oxide during sintering involves adding excess carbon and heat treating the sample at an intermediate temperature under vacuum before heating to the final sintering temperature. This allows the carbon to react with the oxide to form CO gas which is then evacuated from the system. The drawbacks to this method are that it often requires a significant excess of carbon to completely remove the oxide, leaving extra carbon behind in the dense microstructure resulting in reduced mechanical properties. This excess

carbon can also cause mixing issues, gas pressure buildup and cracking of samples in pressureless sintering, and other problems.

In this work, the oxide was removed using both methods. Samples were made with powder that had been acid washed according to the previously described procedure, as well as incrementally increasing amounts of added carbon, from 0% to 4.5% in samples with untreated SiC powders. The carbon was added as one of two sources – a particulate lampblack and a liquid phenolic resin. The lampblack is easier to use but may have issues with uniformity of mixing, while the phenolic resin requires additional processing steps but should result in a more intimate mixture with the silicon carbide. Samples made with the different types of carbon additive were compared to see how much the carbon source affects the oxygen removal and properties of the dense SiC. The matrix of samples that were produced is shown below in Table 1.

Table 1. Silicon Carbide Sample Matrix

Sample Series	SiC Powder	Oxygen Content	Carbon Added	Notes
HC-AW- series	HC Starck	0.5% - 3.36%	1.5%	HC Starck powder washed and aged to different O ₂ content
SG-AW- series	Saint Gobain	0.2% - 0.98%	1.0%	St. Gobain powder washed and aged to different O ₂ content
HC-LBC- series	HC Starck	1.7%	0% - 5%	HC Starck powder with different C amounts added (lamp black)
SG-LBC- series	Saint Gobain	0.3%	0% - 2%	St. Gobain powder with different C amounts added (lamp black)
HC-PRC- series	HC Starck	1.7%	0% - 5%	HC Starck powder with different C amounts added (phenolic resin)
SG-PRC- series	Saint Gobain	0.3%	0% - 2%	St. Gobain powder with different C amounts added (phenolic resin)

3.2.3. Task 3: Fabrication of Dense Samples

After the silicon carbide powder samples were prepared, they were densified using the previously described sintering procedure. Using Specview software, the SPS unit is able to record a number of parameters in real time during the sintering process, including temperature, pressure, ram displacement, and chamber pressure. Comparing differences in the shrinkage and chamber pressure profiles between samples can shed light on the effect that different oxygen levels have on the densification process.

3.3. Objective 3: Characterization of Dense Samples

To understand the role of the oxygen content of silicon carbide powders on the properties of dense bodies made using them, the samples made using the powders with

different oxygen contents needed to be characterized. The SiC samples were subjected to a full range of characterization techniques. This objective can be split into four tasks: ultrasound analysis, microstructural characterization, mechanical properties evaluation, and data analysis.

3.3.1. Task 1: Ultrasound Analysis

Ultrasound analysis was conducted in order to measure the elastic properties of each of the dense silicon carbide samples. Since ultrasound analysis is a nondestructive technique, it was performed before the other characterization methods. Pulse-echo, immersion based ultrasound was used for this analysis. This means that one transducer was used to both emit and receive the ultrasound energy and the transducer and sample were immersed in water as a transmission medium. Point measurements using 20 MHz central frequency transducers were made to measure the elastic properties of each sample according to ASTM standard E494. Additionally, acoustic attenuation spectroscopy was conducted for each sample in the range of approximately 10 – 150 MHz. For all point measurements, the average of five measurements was used. Acoustic spectroscopy has been demonstrated to be a viable method for examining microstructures in some dense ceramic systems by previous work conducted at Rutgers. The attenuation spectra can give insight to a number of properties of a ceramic material including grain size and secondary phase distributions without harming the sample.

The attenuation coefficient is calculated by first measuring the intensity of the ultrasound from two successive bottom surface reflections. The attenuation coefficient is then calculated by

$$\alpha = \frac{8.686}{2d} \left[-2 \ln \frac{I}{I_0} + \ln R^2 \right] \quad \text{Equation 3}$$

where α is the attenuation coefficient, d is the thickness of the sample, I_0 and I are the ultrasound intensity of the first and second bottom surface reflections, respectively, and R is the reflection coefficient of the material.

In addition to using the ultrasound measurements to characterize and compare the samples made for this study, the measurements will help contribute to a library of samples for future ultrasound characterization. This work created samples with varied microstructures at the same compositions which will allow for the determination of the acoustic absorption and scattering coefficients in these systems. By comparing the ultrasound attenuation spectra to the microstructural features found in each sample, these coefficients can be determined and calibrated. The lack of reference samples has long been a roadblock to using ultrasound acoustic spectroscopy for quantitative microstructural measurements and while it was not a primary objective of this thesis, producing samples that can serve as references was a beneficial side-effect.

Several transducers were used including an Olympus V316 20 MHz central frequency transducer, an Olympus V222-BA-RM 20 MHz central frequency shear contact transducer, an Ultratran 75 MHz central frequency transducer, and a Valpey-Fisher VF418 150 MHz central frequency transducer. Although each transducer has an indicated central frequency, they emit ultrasound over a much wider range, or bandwidth. The bandwidth of each transducer is determined by the -6 dB range, that is, the frequency range where the signal is half as strong as the maximum. While the bandwidth can change depending on the material being examined, in silicon carbide, with these three transducers, the range from approximately 10 – 150 MHz is covered. These transducers are paired with JSR RP-L2, RP-H2, and RP-U2 remote pulsers and a JSR DPR500 dual

pulser-receiver. These together with a Techno-Isel iMove Gantry 500 scanning frame and iMove C10 motion controller are interfaced with a PC and custom software developed using MATLAB for control and data acquisition.

3.3.2. Task 2: Microstructure Characterization

After ultrasonic evaluation, the samples were sectioned and three pieces were polished to a 0.25 μm finish for imaging using a Zeiss Sigma field emission scanning electron microscope. One polished piece from each sample was etched in boiling Murakami's reagent (20 g KOH and 20 g $\text{K}_3\text{Fe}(\text{CN})_6$ in 50 mL H_2O) in order to better view the sample microstructure. Microstructural imaging was conducted to examine the grain size and morphology of the dense silicon carbide samples. Image analysis software (Lince 2.4.2e) was used with the micrographs to determine average grain size by the linear intercepts method and average aspect ratio. An unetched, polished and ion milled piece of each sample was used for EBSD analysis using an Oxford Instruments Nordlys Nano. The EBSD technique was used to determine grain orientation and phase and polytype composition. Pieces of the dense samples were also used for XRD analysis to confirm the polytype composition determined by EBSD.

3.3.3. Task 3: Mechanical Properties Evaluation

Because silicon carbide ceramics are often used in high performance applications including structural and armor applications, its mechanical properties are extremely important. In particular, the elastic moduli, hardness, and compressive strength are vital in these types of applications. The elastic properties of the dense silicon carbide samples, including longitudinal and shear sound velocities, Poisson's ratio, Young's modulus, shear modulus, and bulk modulus were measured by the ultrasound method described

above. Additional polished specimens were used for hardness testing using a LECO M-400-G3 microhardness tester to determine Knoop hardness using a diamond tipped indenter over a range of loads from 100 – 2000 g.

3.3.4. Task 4: Data Analysis

After characterizing the powders and densified samples, the data was analyzed in order to find correlations between the oxygen content in the starting powders and microstructural features like grain size and shape, as well as polytype composition. Correlations to the mechanical properties like elastic properties and hardness were also investigated. These results are used to determine the effects of the oxygen content of silicon carbide powders on the microstructure and mechanical properties of SiC materials solid state sintered via spark plasma sintering.

4. Experimental Procedures

4.1. Powder Characterization

4.1.1. Particle Size Analysis

Particle size analysis of the silicon carbide powders was conducted using a Malvern Mastersizer 2000 with Hydro 2000S cell (Malvern Instruments, Malvern, UK) using the dynamic light scattering method.

4.1.2. X-Ray Diffraction

X-ray diffraction analysis was performed on the silicon carbide powders using a Panalytical X'Pert Pro (PANalytical, Almelo, Netherlands) system with a Cu x-ray source at 45 kV and 40 mA over a continuous scan range of 10° to $90^\circ 2\theta$; at a virtual step size of 0.0131° and counting time of 200 seconds. An anti-scatter slit of 1° and divergent slit of $1/2^\circ$ were used in the incident beam path. The diffracted beam path also had an anti-scatter slit of 9.1 mm. The sample was rotated at 15 rpm to randomize particle orientation.

4.1.3. Electron Microscopy

Electron microscopy of the SiC powders was performed using a Zeiss Sigma field emission scanning electron microscope (Carl Zeiss Microscopy GmbH, Jena, Germany). The powder samples were prepared by placing a circle of carbon tape on an aluminum stud and pressing the carbon tape onto a small amount of powder. Excess powder was blown off of the carbon tape using a canned compressed air duster. The powder samples were examined with a 3 kV accelerating voltage using a 30 micron aperture. The working distance for each image was set to approximately 8 mm. Images of the samples were taken at 25000 times magnification using the SE2 detector.

4.1.4. Chemical Analysis

Chemical analysis of the oxygen and nitrogen content of the SiC powders was performed using a LECO TC600 oxygen/nitrogen analyzer (LECO Corporation, St. Joseph, MI, USA). The instrument was calibrated using the LECO 502-399 oxygen standard and LECO 501-996 nitrogen standard. Three runs using 0.1000 grams of powder each were analyzed for each sample.

4.2. Powder Preparation

4.2.1. Initial preparation

The HC-SiC powder was ready to be used as received without any initial preparation. For the SG-SiC, it was necessary to first dilute the slurry and sieve it to remove large SiC particles. Approximately 200 grams of the slurry was diluted with 1 liter of deionized water and stirred until it reached an even, paint-like consistency. It was then passed through a 45 μ m mesh sieve to remove the large particles. The slurry was then dried in the sieve collection pan on a hotplate. The dried powder was stored in a sealed Nalgene container until used.

4.2.2. Acid Washing

To reduce the oxygen content, the powders were treated with hydrofluoric acid. This acid washing process removes the native oxide layer from the particle surfaces and thereby lowers the oxygen content of the powder. In the acid treatment process, 30 g of silicon carbide powder was mixed with 100 mL of 50% HF solution (Acros Organics 48 – 51% solution, Thermo Fisher Scientific, Geel, Belgium). This mixture is then stirred for one hour in a Nalgene HDPE beaker using a Teflon coated magnetic stir bar. Afterwards, the mixture is neutralized with ammonium hydroxide (reagent ACS grade, Acros

Organics) until it reaches a pH of 7. The silicon carbide is then rinsed with deionized water and centrifuged to separate the silicon carbide from the water. The water is removed and this rinsing step is repeated three more times and the powder is dried.

4.2.3. Aging

Powders were aged in Nalgene bottles with the cap loosely placed on top. This was to prevent airborne dust or debris from falling into the container while still allowing air to enter the container. For samples aged at room temperature, the bottles were placed in a closed drawer and allowed to sit there for a specified period of time. For samples aged at elevated temperatures, the bottle was placed in a drying oven at 100°C for the specified period of time.

4.2.4. Heat Treatment

Powders were heat treated in a tube furnace at 600°C in air overnight. For the HC-SiC, 50 g of powder was placed in a glass boat in the hot zone of the tube furnace with the end caps removed to let air flow through. The temperature was ramped at 240°C/h to 600°C and held there for 10 hours before allowing the furnace to cool naturally. For the SG-SiC, 55 g of powder was placed in a glass boat in the hot zone of the tube furnace with the end caps removed to allow air to flow through. The temperature was again ramped at 240°C/h to 600°C and held there for 12 hours before allowing the furnace to cool naturally.

4.2.5. Mixing

In general, the samples used in this work were mixed by ball milling the powders in ethanol. When using all dry powders, the SiC, lamp black carbon, and boron carbide were measured and put into a 250 mL HDPE Nalgene container. When measuring small

amounts, like with the carbon and boron carbide, it was easier to use a metal weighing dish instead of plastic as the static on the plastic ones can make accurate measurement difficult. Ethanol was then added to the container and manually stirred to wet all of the powder. About 150 g of 3 mm SiC ball milling media was added and the container was sealed and left to roll on the ball mill for approximately 24 hours. In the case of the samples made using phenolic resin as the carbon source, the SiC and boron carbide powders were mixed with a liquid mixture of phenolic resin and water with ammonium hydroxide as a dispersant.

4.2.6. Drying

After 24 hours on the ball mill, the slurries were removed and passed through a 1.4 mm mesh sieve to remove the SiC media. For the slurries made using dry powders and ethanol, the liquid was removed by pan drying the slurry in the sieve pan on a hotplate set at 275°C. Once all the liquid had evaporated, the powder was collected in a Nalgene container and left to dry completely in an oven set to 100°C. For the slurries made with the phenolic resin, the liquid was removed by filter pressing in a Baroid filter press at 30 – 40 psi. Once liquid stopped flowing from the press, the pressure was released and the filter cake was removed. The filter cake was then broken up and placed in a glass beaker in an oven set to 100°C to dry completely. Periodically during drying, the pieces of the filter cake were manually broken apart to speed the drying process. The powder was typically completely dry within an hour.

4.3. Sintering

4.3.1. Spark Plasma Sintering

Samples were densified using a Thermal Technology SPS 10-4 spark plasma sintering unit (Thermal Technology, LLC, Santa Rosa, CA, USA) using 6.5 grams of powder in a 20 mm inner diameter graphite die lined with graphite foil. During the sintering process, the temperature of the sample is measured using an optical pyrometer aimed at a small hole drilled halfway into the side of the graphite die. Because the pyrometer cannot detect temperatures lower than about 550°C, the sintering cycle starts by ramping up to 600°C and 10 MPa of pressure and holding there until the pyrometer starts to read the actual temperature of the die. The samples made using lamp black as the carbon source were heated under vacuum to an intermediate dwell temperature of 1400°C at 200°C per minute while increasing to 50 MPa of uniaxial pressure at 10 MPa per minute. After 30 minutes at 1400°C, the chamber was backfilled with argon and then the samples were heated to 1900°C at 200°C per minute and held for 15 minutes, maintaining 50 MPa of pressure. After 15 minutes at the sintering temperature, the pressure was released and the system was allowed to cool for approximately 45 minutes before removing the sample. For samples made using phenolic resin as the carbon source, the same procedure was followed, but an additional hold under vacuum at 800°C and 20 MPa for 30 minutes was added in order to burn out the resin and convert it to carbon.

4.4. Dense Sample Preparation

4.4.1. Sand Blasting and Grinding

After densification in the SPS unit, the dense samples are covered in the remnants of the graphite foil. To remove the excess graphite on the surfaces, the samples are sand

blasted using garnet blasting media. After sand blasting, the samples are ground flat using a surface grinder with a 600 grit diamond wheel to prepare the surfaces for ultrasonic evaluation. Due to the imperfect fit of the punches and die, there can sometimes be small protrusions along the edges on the samples. These must be removed prior to surface grinding so that the sample can sit flat in the chuck holding it in the surface grinder. To remove these protrusions, the edges are manually flattened using a 125 micron grit diamond grinding pad on an automatic polisher. When grinding the samples on the surface grinder, the sample is ground by 0.001 inches of thickness at a time under a constant stream of lubricant solution. The lubricant solution was a 1:20 mix of Cimstar 540 in water. After the first side is ground flat, the sample is flipped over in the chuck and the other side is ground flat.

4.4.2. Sectioning

To make smaller samples for FESEM imaging, EBSD, and hardness testing, the dense samples are sectioned into several smaller pieces using a LECO VC-50 diamond saw (LECO Corporation, St. Joseph, MI, USA). To get each piece as close to the center of the sample as possible, the disk is cut as shown below in Figure 8. A cut is made on a dressing stick before cuts 1, 2, and 3. To ensure a thin, flat surface for EBSD, cuts 1 and 2 were made as parallel as possible, and approximately 2 – 3 mm apart.

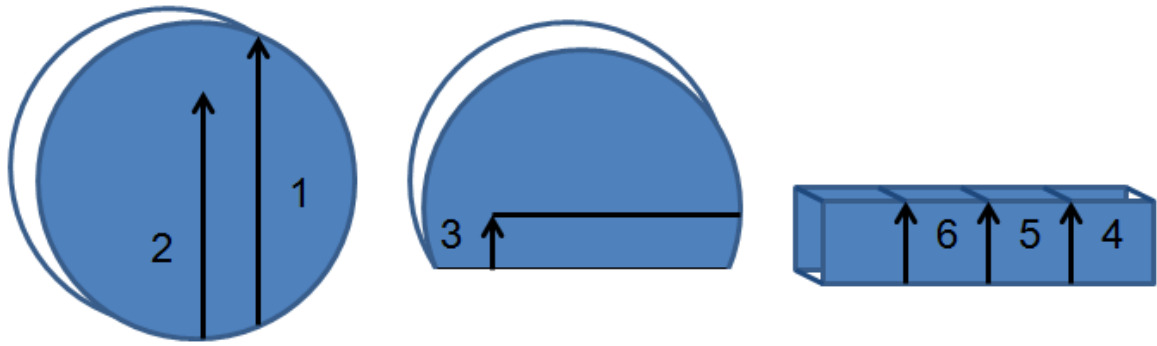


Figure 8. SPS sample cutting procedure

4.4.3. Polishing

To prepare the samples for FESEM imaging, EBSD, and hardness testing, they were polished using successively finer diamond grit sizes. The samples were first mounted in Buehler Epomet F epoxy resin using a Buehler SimpliMet 1000 automatic mounting press (Buehler, Lake Bluff, IL, USA). The mounted samples were then polished using a Buehler EcoMet 250 automatic grinder/polisher with AutoMet 250 automatic head. The polishing schedule typically used for silicon carbide samples is shown below in Table 2. In each case, the time shown is a starting point. If after that step, there were still larger scratches, the step was repeated until a consistent polish was achieved. After each step, the samples and sample holder were cleaned to remove any residual diamond before moving to the next step to prevent contamination of the pads. Because the diamond saws use a smaller grit size, 125 and 70 micron diamond pads were redundant and were not used unless there was a need to quickly grind a lot of material from the sample. After the sample was polished it was removed from the mounting material if it was to be used for FESEM imaging or EBSD. Samples used for hardness testing remained in the mounting material.

Table 2. SiC polishing schedule

Step	Diamond Grit Size (μm)	Pad Type	Head Speed (rpm)	Platen Speed (rpm)	Force (lb)	Time	Fluids	Rotation Direction
1	125	Diamond Embedded	60	200	5	30s	Water	Opposite
2	70	Diamond Embedded	60	200	5	30s	Water	Opposite
3	45	Diamond Embedded	60	200	5	30s	Water	Opposite
4	15	Diamond Embedded	60	200	5	30s	Water	Opposite
5	9	Cloth	60	170	5	20m	9 μm diamond suspension	Opposite
6	6	Cloth	60	170	5	20m	6 μm diamond suspension	Opposite
7	1	Cloth	60	170	5	20m	1 μm diamond suspension	Opposite
8	0.25	Cloth	60	170	5	10m	0.25 μm diamond suspension	Same

4.4.4. Ion Milling

To better prepare the surface of the samples for EBSD analysis, polished samples were ion milled using a Hitachi IM4000 broad ion beam ion mill (Hitachi High-Technologies Corporation, Tokyo, Japan). Each sample was fixed to the ion mill sample holder using carbon tape so that the surface of the sample was level with the rim of sample stage. The samples were milled using the flat-milling mode with 3kV acceleration voltage, 80° tilt angle, no offset, and 25rpm rotation speed for 10 minutes. After ion milling, the samples were cleaned using isopropyl alcohol. Figure 9 below shows the

difference in surface quality between a SiC sample that had been mechanically polished and the same sample after ion milling. The number and severity of scratches is greatly reduced after the ion milling procedure.

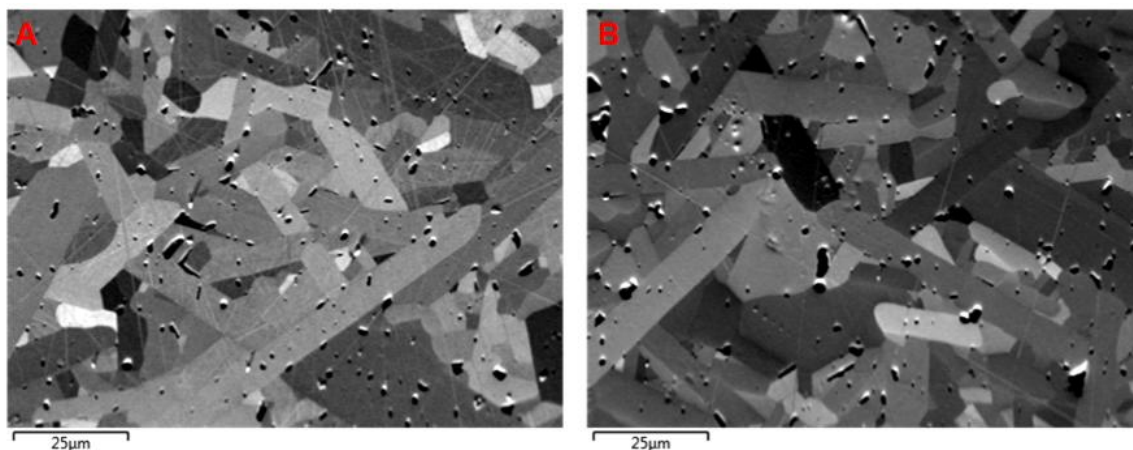


Figure 9. FESEM images of a SiC sample after mechanical polishing (A), and after ion milling (B)

4.4.5. Etching

In order to better view the sample microstructure during FESEM imaging, the polished samples were etched using a modified Murakami etching procedure, where the samples were boiled in a solution of potassium hydroxide and potassium ferricyanide in water. To prepare the etching solution, first 20 g of potassium ferricyanide was added to a small beaker with 30 mL of DI water and stirred. At this point the, potassium ferricyanide was not completely dissolved and there was a lot of orange powder left on the bottom of the beaker. In another beaker, 20 g of potassium hydroxide was slowly added to 30 mL of DI water. The potassium hydroxide was added slowly, about 3 or 4 grams at a time and stirred to dissolve completely before more was added. Once all of the potassium hydroxide was dissolved in the water, the hydroxide solution was poured into the beaker with the potassium ferricyanide mixture. The beaker with the combined mixture was then

covered with a watch glass and heated on a hot plate at 275°C. As the solution heated up and started to boil, the potassium ferricyanide on the bottom dissolved completely and the solution turned a consistent, dark yellow color. Once the etching solution reached a rolling boil, the sample or samples were placed in the beaker. If several samples were to be etched at the same time, it was helpful create some sort of distinguishing marks so that they could be told apart after removal from the etching solution. The etching time varies between different materials and compositions. For the samples discussed in this thesis, the etching time varied between 5 and 7 minutes. After the allotted etching time has passed, the sample was removed from the etching solution using tweezers and dunked in a beaker of DI water to stop the etching process. If several samples were being etched at the same time, it was helpful to dump the etching solution into a separate, empty beaker before removing the samples so that it was easier to remove the samples. Also, this would help to prevent differences in etching severity between the first and last sample removed in this way. The sample was then rinsed and cleaned by sonicating in DI water and then sonicating in isopropyl alcohol.

4.5. Dense Sample Characterization

4.5.1. Density Measurements

The densities of the samples made for this thesis were determined using the Archimedes method. All sample densities were measured after surface grinding. First the sample was washed to remove any residue from the grinding process and dried. Five measurements of the dry weight were then recorded, zeroing the balance between each measurement. The sample suspension apparatus was then put into place to measure the weight of the sample when suspended in water, making sure that the sample was fully

submerged in the water and that it did not come into contact with the beaker. Five measurements of the suspended weight were recorded, again zeroing the balance between each measurement. The density of the sample was then calculated by dividing the dry weight by the difference between the dry weight and the suspended weight.

4.5.2. Ultrasound Measurements

Ultrasound measurements were conducted on each sample to measure the elastic properties and the frequency dependent acoustic attenuation coefficients. The elastic properties measurements were performed using single transducers in pulse-echo configuration, where the same transducer both emits and receives the ultrasound energy. Longitudinal time of flight (LTOF) was measured using an Olympus V316 transducer (Olympus Corporation, Tokyo, Japan) with the transducer and sample both immersed in water. Shear time of flight (STOF) was measured using an Olympus V222-BA-RM shear contact transducer with Sonotech Shear Gel as a couplant. The TOF values were used to calculate the longitudinal (c_L) and shear (c_S) sound speeds by the following equations:

$$c_L = \frac{2d}{LTOF} \quad \text{Equation 4}$$

$$c_S = \frac{2d}{STOF} \quad \text{Equation 5}$$

where d is the thickness of the sample. The other elastic properties are then calculated using the following equations where ν is the Poisson's ratio, E is the Young's modulus, G is the shear modulus, K is the bulk modulus, and ρ is the density:

$$\nu = \frac{1 - 2\left(\frac{c_S}{c_L}\right)^2}{2 - 2\left(\frac{c_S}{c_L}\right)^2} \quad \text{Equation 6}$$

$$E = \frac{(1 - 2\nu)(1 + \nu)\rho c_L^2}{(1 - \nu)} \quad \text{Equation 7}$$

$$G = \frac{E}{2(1+\nu)} \quad \text{Equation 8}$$

$$K = \frac{E}{3(1-2\nu)} \quad \text{Equation 9}$$

Attenuation coefficient spectra were also taken for each sample from five points and averaged. Several transducers were used including an Olympus V316 20 MHz central frequency transducer, an Ultratran 75 MHz central frequency transducer (The Ultratran Group, State College, PA, USA), and a Valpey Fisher VF418 150 MHz central frequency transducer (Valpey Fisher Corporation, Hopkinton, MA, USA). Although each transducer has an indicated central frequency, they emit ultrasound over a much wider range, or bandwidth. The bandwidth of each transducer is determined by the -6 dB range, that is, the frequency range where the signal is half as strong as the maximum. The bandwidth can change depending on the material being examined and in silicon carbide, with these three transducers, the range from approximately 10 – 150 MHz was covered. These transducers were paired with JSR RP-L2, RP-H2, and RP-U2 remote pulsers and a JSR DPR500 dual pulser-receiver (Imaginant Inc., Pittsford, NY, USA). These together with a Techno-Isel iMove Gantry 500 (Isel USA Inc., Hicksville, NY, USA) scanning frame and iMove C10 motion controller were interfaced with a PC and custom software developed using MATLAB for control and data acquisition.

4.5.3. Hardness Testing

Hardness testing was performed using a LECO microhardness tester. Polished samples were indented using a Knoop diamond indenter at loads of 100, 200, 500, 1000, and 2000 grams, each applied for 10 seconds. Ten indents were made at each load. For loads less than 1000 grams, the indents were spaced at least 50 μm away from each other along the short axis and 200 μm away on the long axis. For higher loads, the spacing was

increased to 100 μm and 400 μm , respectively. Measurements of the indent sizes were made using a Keyence VHX5000 digital microscope (Keyence Corporation, Osaka, Japan) using a 500-5000x magnification lens. Indents that displayed large cracks, spalling, or large pores at the tips were not included in the measurements.

4.5.4. Electron Microscopy

Electron microscopy of the sample microstructures was performed using a Zeiss Sigma field emission scanning electron microscope. Polished and etched samples were examined with a 3kV accelerating voltage using a 30 micron aperture. The working distance for each image was set to approximately 8.5mm. Images of the samples were taken at magnifications of 1000, 2500, 5000, and 10000 times using both SE2 and inlens detectors. The grain size of each sample was measured by the linear intercepts method using Lince 2.42e software and a conversion factor of 1.56 to convert the intercept length to grain size.[67]

4.5.5. Electron Backscatter Diffraction

Electron backscatter diffraction (EBSD) was performed on each sample using an Oxford Instruments Nordlys Nano EBSD detector (Oxford Instruments, Abingdon, UK) on the Zeiss Sigma FESEM. Conductive carbon tape and silver paint was applied to the polished and ion milled samples surrounding the area of interest to mitigate charging effects. The samples were mounted on a 70° tilted specimen holder and placed in the second mounting point on the sample stage. The stage was then rotated 63.3° counter clockwise to align the sample with the EBSD detector. The EBSD detector was fully inserted to 199.5 mm and the accelerating voltage on the FESEM was increased to 20 kV. The 60 micron aperture was used and high current mode was enabled. The working

distance used was typically between 7 and 10 mm. EBSD data collection was performed using Oxford Aztec software. Automatic drift correction was applied using the Autolock feature in the Aztec software using the custom parameters shown below in Table 3.

Table 3. Aztec software autolock parameters

Reference/Tracking Image	
Image Scan Size	512
Dwell Time	5 μ s
Frame Time	1.0 s
Input Signal	FSE
Scan Settings	
Use Automatic Measurement Interval	Unchecked
Measurement Interval	5 s
Autolock Mode	
In-field	Unselected
Extended Field	Selected
Maximum Drift	50% (2x Zoom)
Maintain Subject Size	Checked
Use Predictive Correction	Checked
Reference Interval	10 s

4.5.6. X-Ray Diffraction

X-ray diffraction analysis was performed on the dense samples using a Panalytical X'Pert Pro system with a Cu x-ray source at 45 kV and 40 mA over a continuous scan range of 10° to 90° 2 θ ; at a virtual step size of 0.0131° and counting time

of 200 seconds. An anti-scatter slit of 1° and divergent slit of $1/2^\circ$ were used in the incident beam path. The diffracted beam path also had an anti-scatter slit of 9.1 mm. The sample was rotated at 15 rpm to randomize particle orientation.

5. Results and Discussion

5.1. Selection, Treatment, and Characterization of Powders

5.1.1. Powder Selection

For this work, silicon carbide powders with different properties were required to examine the effects of oxygen content on the properties of dense SiC materials made with those powders. Two commercial powders were selected for these studies, one from H.C. Starck (HC-SiC) and one from St. Gobain (SG-SiC). These powders were chosen because they had similar processing histories as Acheson process materials that were crushed and ground to size, and were available in the quantities needed for this work. The biggest differences between the two powders were in the particle size and the conditions in which they were received. The HC-SiC has a finer particle size and was received as a dry powder. The SG-SiC has a coarse particle size and was received as a wet slurry.

5.1.2. Powder Treatment

To prepare the powders used in this study for sintering, the powders were treated as described in section 4.2.

5.1.3. Powder Characterization

5.1.3.1. Chemical Analysis

Chemical analysis was performed on the two silicon carbide powders SG-SiC and HC-SiC using a LECO TC600 oxygen/nitrogen analyzer to determine the powder oxygen content as described in section 4.1.4. Figure 10 shows the oxygen content growth curves for the SG-SiC. The unwashed SG-SiC was powder that had been removed from storage, dried, and left to age at ambient conditions. Three samples were taken over the course of a week and measured for oxygen content. The acid washed SG-SiC was powder that had

been treated using the HF washing procedure, dried, and again left to age at ambient conditions. In this case, six samples were taken over the course of two weeks and measured for oxygen content. For the SG-SiC, the oxygen content of the washed powder starts slightly lower than the unwashed powder and grows over time to reach the same maximum value of about 0.3%. However, the rate at which the oxygen content rises in the washed powder is slower than the unwashed powder, rising over a period of almost two weeks rather than a few days.

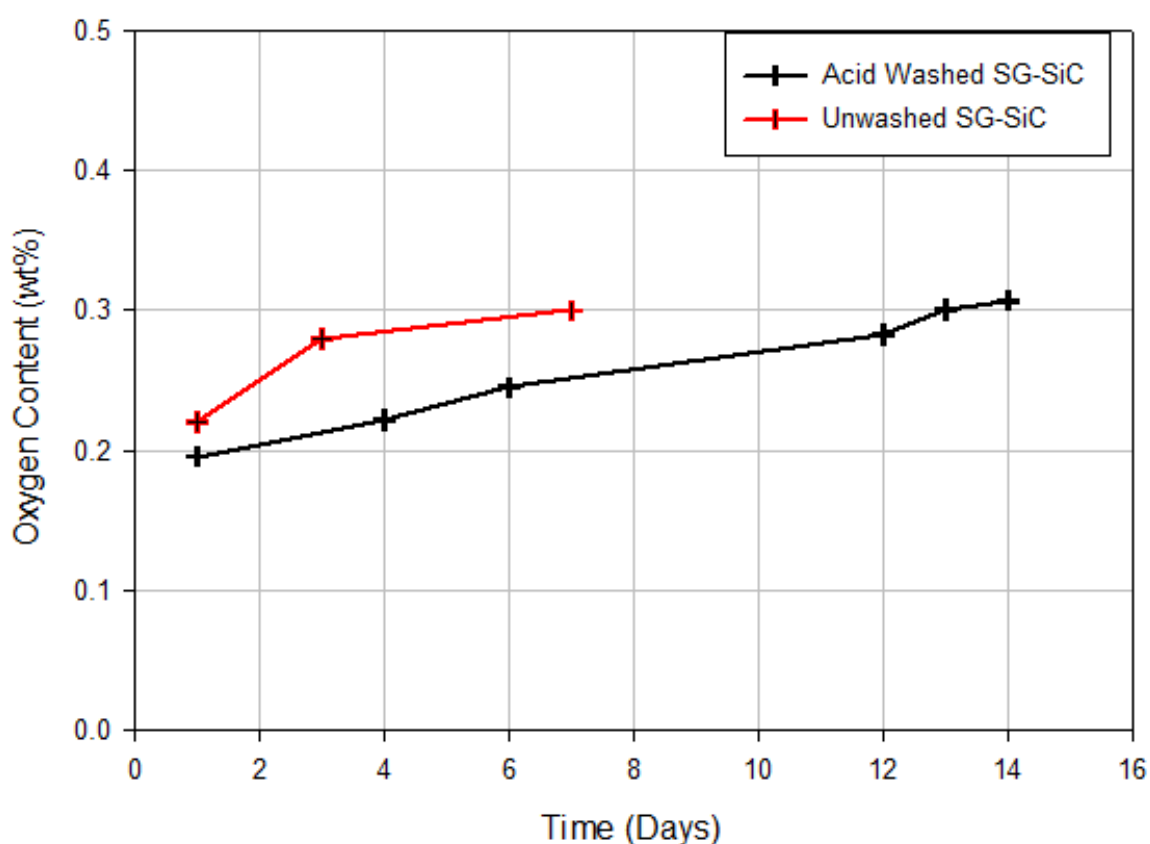


Figure 10. Oxygen content growth curves for acid washed and unwashed SG-SiC powder

Figure 11 shows the oxygen content growth curve for the acid washed HC-SiC. For the HC-SiC, acid washing the powder results in a dramatic decline in oxygen content from 1.69% in the unwashed powder down to about 0.60% immediately after washing.

Over several weeks, ten samples were taken and measured for oxygen content. In this powder, the oxygen content slowly rose to a value of 0.85%.

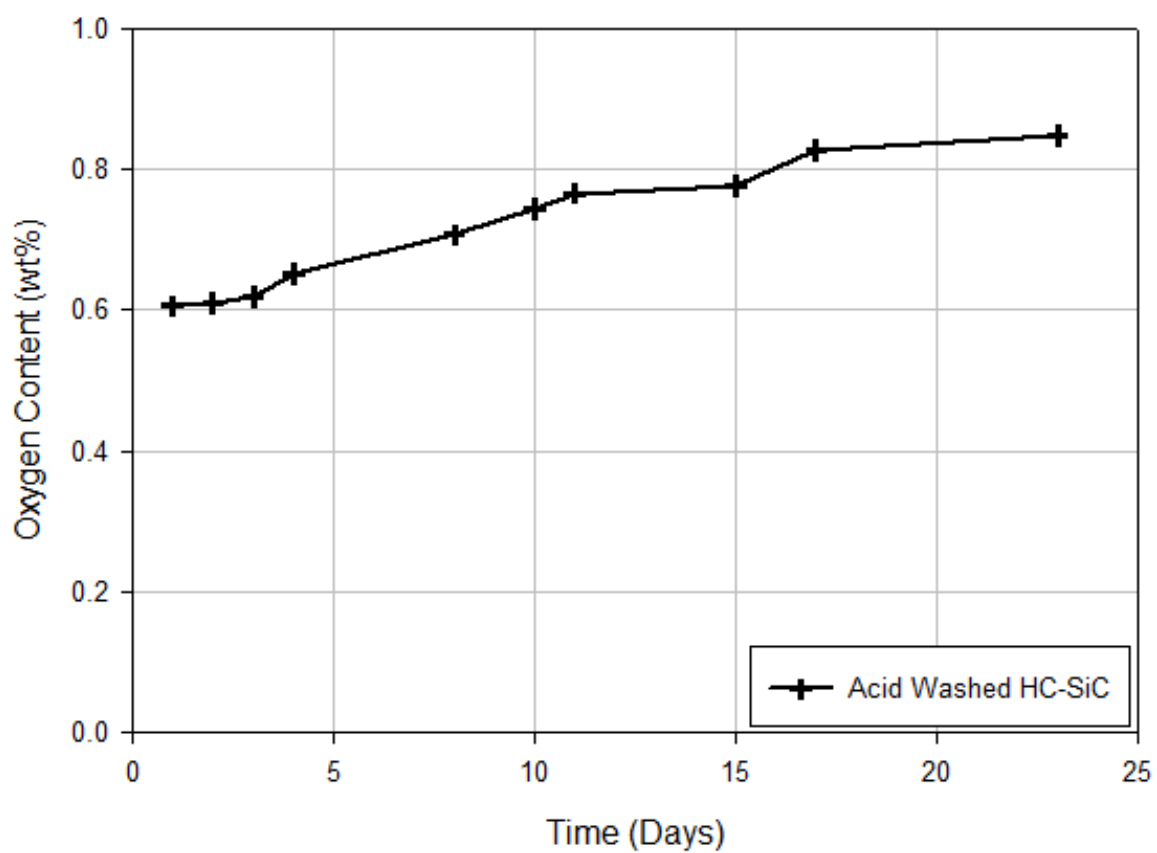


Figure 11. Oxygen content growth curve for acid washed HC-SiC powder

Table 4 below shows the oxygen contents of all of the powders used in this thesis, including the acid washed, aged, and heat treated SG-SiC and HC-SiC powders.

Table 4. Oxygen contents of powders used to create dense samples

Sample	Treatment	Oxygen Content (wt%)
SG-SiC	As received	0.22
SG-SiC	Aged @ RT	0.30
SG-SiC	3 months @ 100°C	0.38
SG-SiC	12 hrs @ 600°C	0.98
HC-SiC	HF Acid wash	0.60
HC-SiC	Aged >20 months @ RT	1.69
HC-SiC	12 hrs @ 600°C	3.36

5.1.3.2. X-Ray Diffraction

XRD analysis was performed using the procedure described in section 4.1.2. on the two SiC powders using a PANalytical X-Pert x-ray diffractometer to determine their initial polytype compositions. The diffraction patterns for the SG-SiC powder and HC-SiC powder are shown in Figure 12 and Figure 13, respectively. Rietveld refinement was performed to determine the initial concentrations of the 6H and 4H polytypes in the SiC powders and the calculated compositions are shown in Table 5.

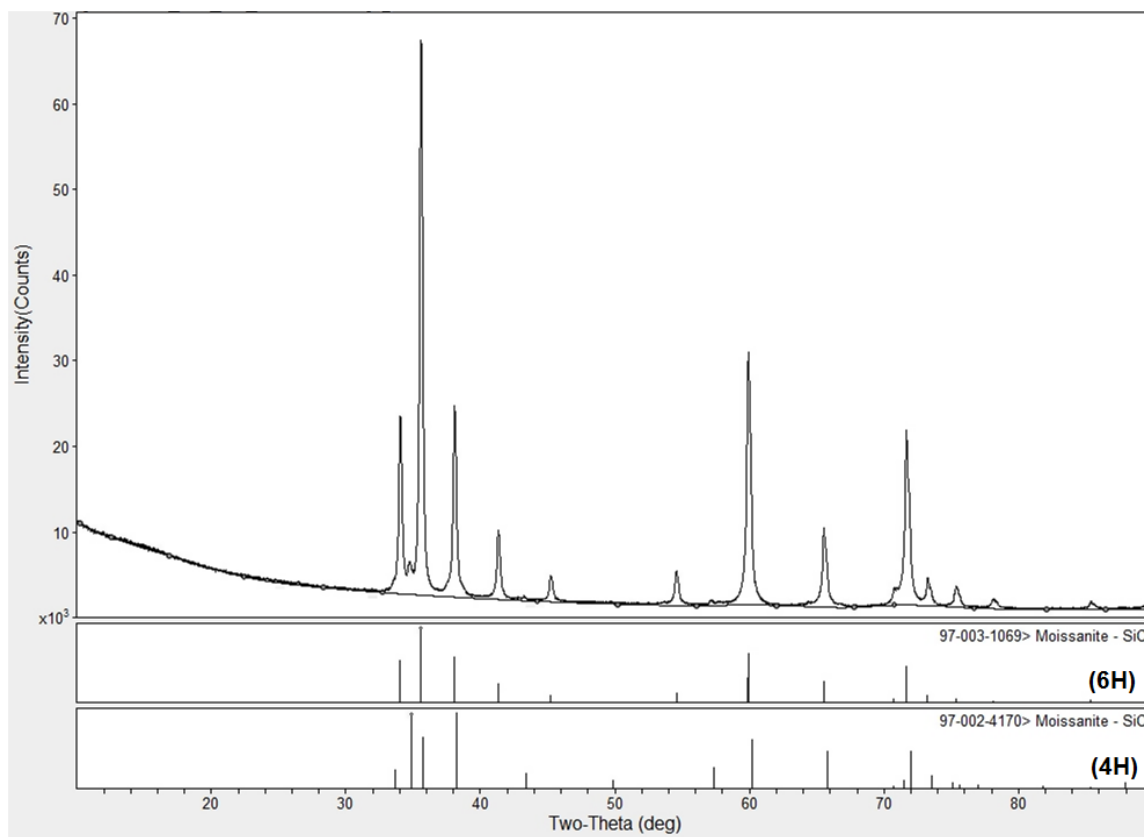


Figure 12. SG-SiC powder X-ray diffraction pattern

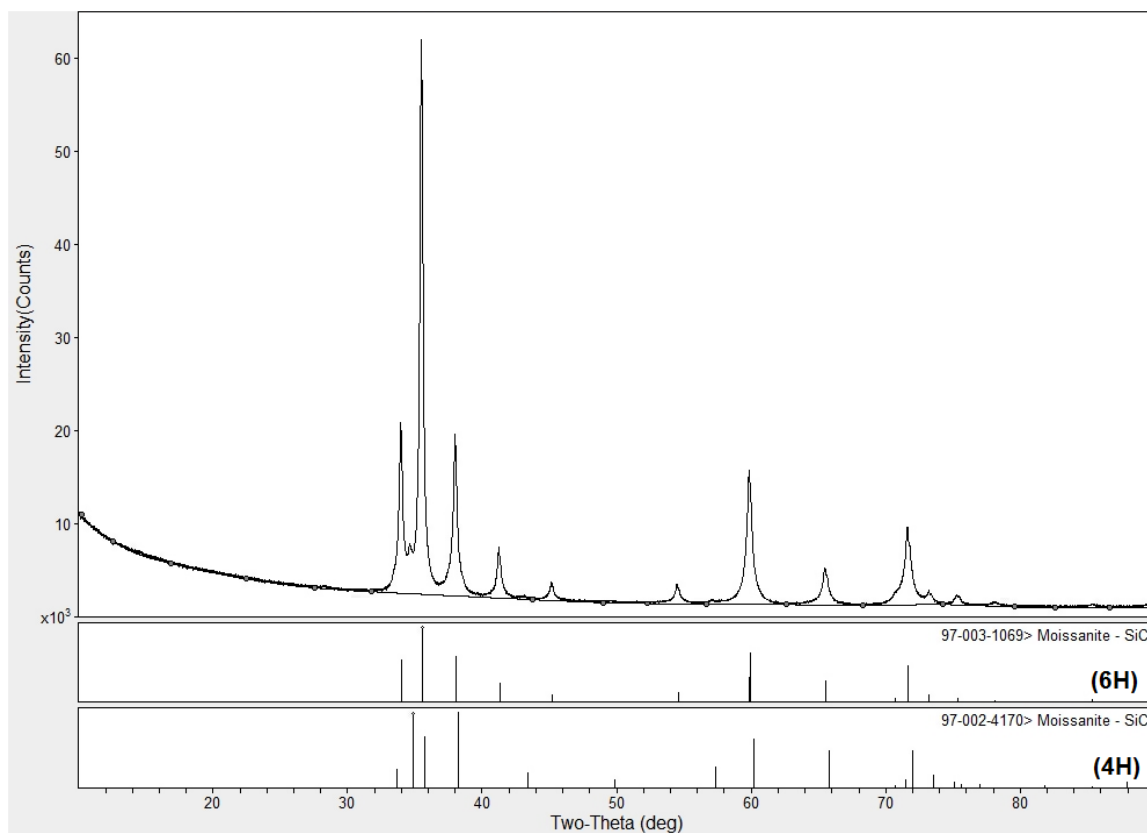


Figure 13. HC-SiC powder X-ray diffraction pattern

Table 5. SiC powder initial polytype compositions

Sample	6H	4H	Other	4H/6H Ratio
SG-SiC	90.2%	9.8%	Trace (<0.1%)	0.11
HC-SiC	86.8%	13.2%	Trace (<0.1%)	0.15

5.1.3.3. Particle Size Analysis

Particle size of the silicon carbide powders was measured by dynamic light scattering using a Malvern Mastersizer 2000 with Hydro 2000S cell. The particle size distribution for the SG-SiC is shown below in Figure 14. Two features are apparent in the particle size measurement. There is a peak at around 1.5 – 2 microns with a long tail on the smaller end and another peak between 40 – 50 microns. The sizes below 10 microns

are the primary particles while the larger ones are likely large agglomerates formed by the pan drying process. This is corroborated by FESEM imaging of the powder, which shows primary particles in the 1 – 2 micron size range with many smaller particle fragments which contribute to the long tail at the lower size range. Because the SiC powders are mixed with additives by ball milling, the large agglomerates will be broken up during that process.

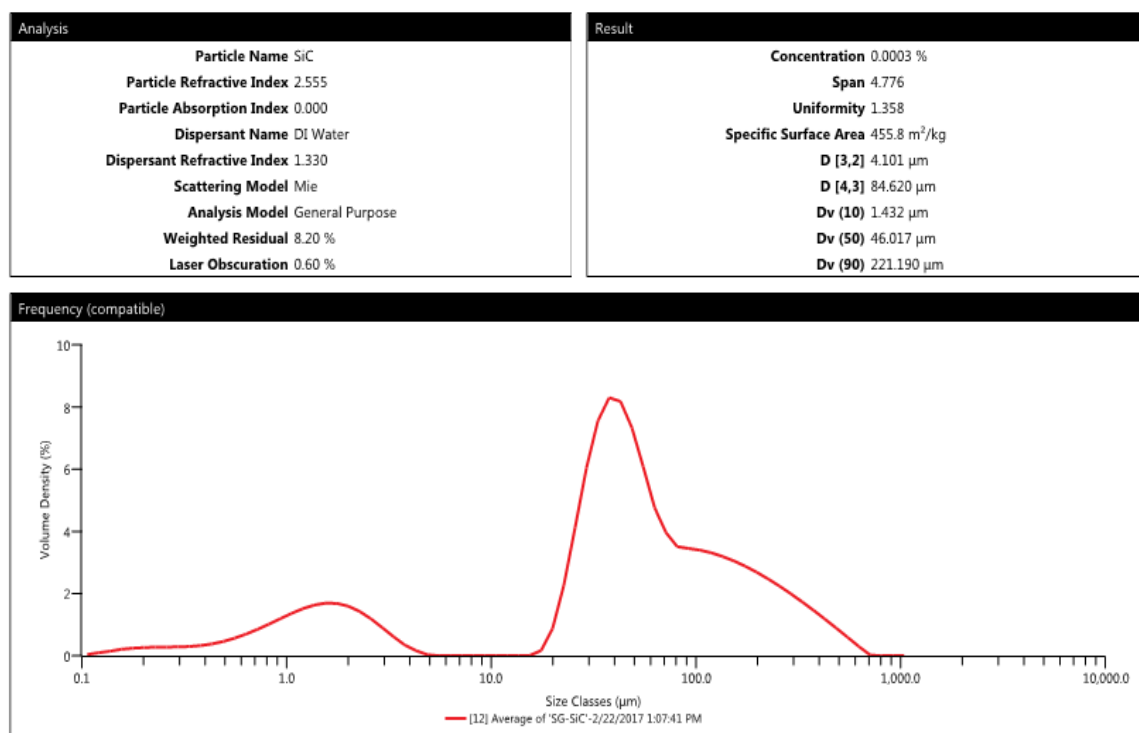


Figure 14. SG-SiC particle size distribution

The particle size distribution for the HC-SiC is shown below in Figure 15. Again, two features are apparent in the particle size measurement. There is a peak at 0.5 microns and another peak between 8 – 9 microns. The sizes below 1 micron are the primary particles while the larger ones are likely agglomerates that formed as the powder sat in storage. This is corroborated by FESEM imaging of the powder, which shows primary

particles in the 0.5 micron size range. Because the SiC powders are mixed with additives by ball milling, the larger agglomerates will be broken up during that process.

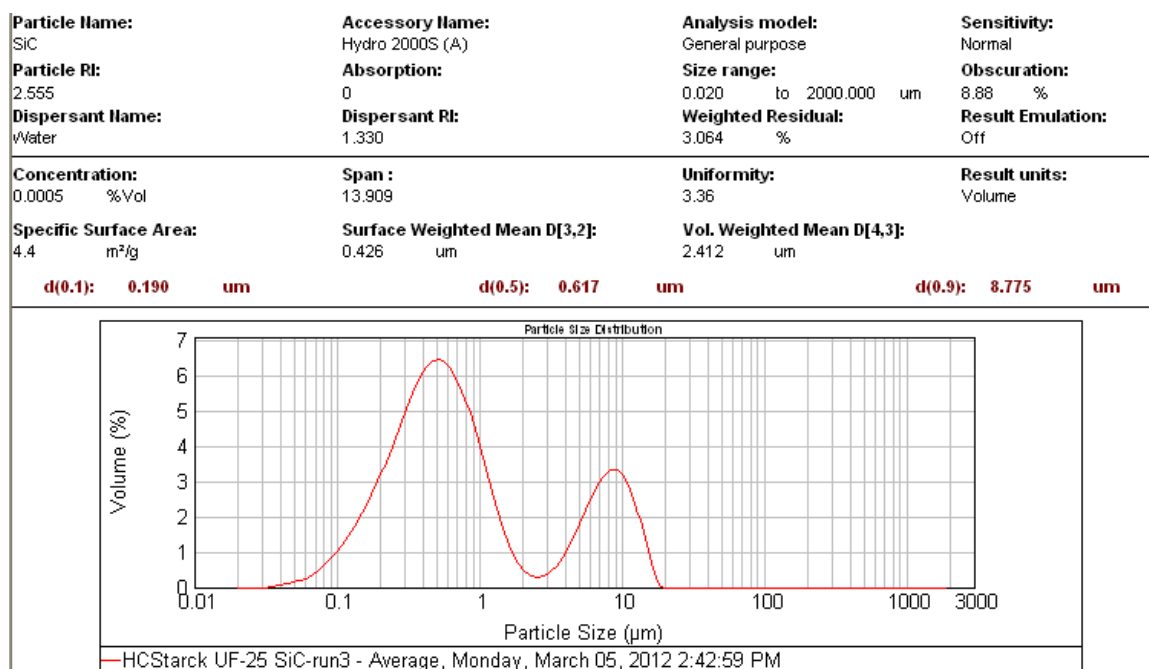


Figure 15. HC-SiC particle size distribution

5.1.3.4. FESEM Imaging

FESEM image analysis was performed on the powders to confirm the measured particle sizes and to examine the morphology of the powder particles. Micrographs of the SG-SiC and HC-SiC powders are shown below in Figure 16 and Figure 17, respectively. As mentioned previously, the primary particles of the SG-SiC powder are between 1.5 – 2 microns in size with many smaller fragments also seen around them. No individual particles larger than 5 microns were seen, supporting the idea that the larger end of the measured size distribution in the previous section consisted of large agglomerates. The same is true of the HC-SiC powder – no individual particles large than about 1 micron were seen, suggesting that the larger measured particles were simply agglomerates.

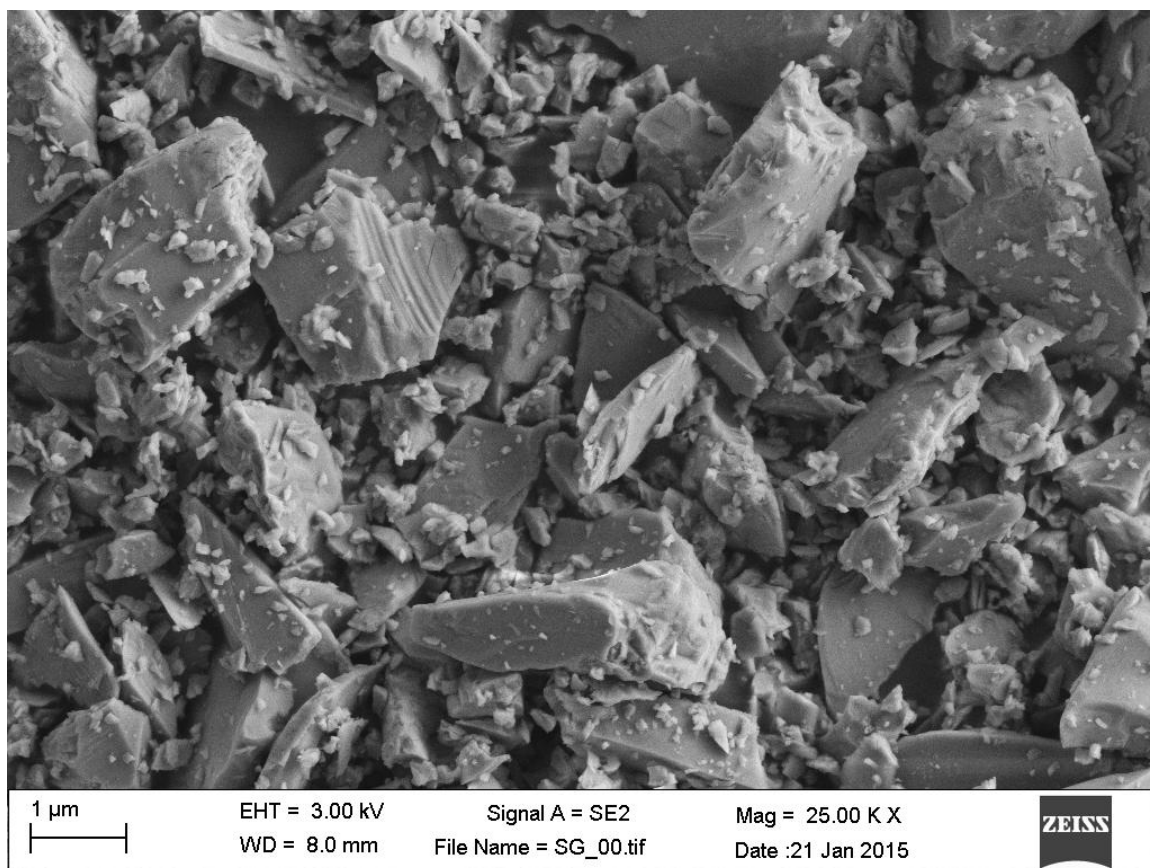


Figure 16. SG-SiC powder micrograph showing primary particles 1 - 3 μm in size with smaller particle fragments

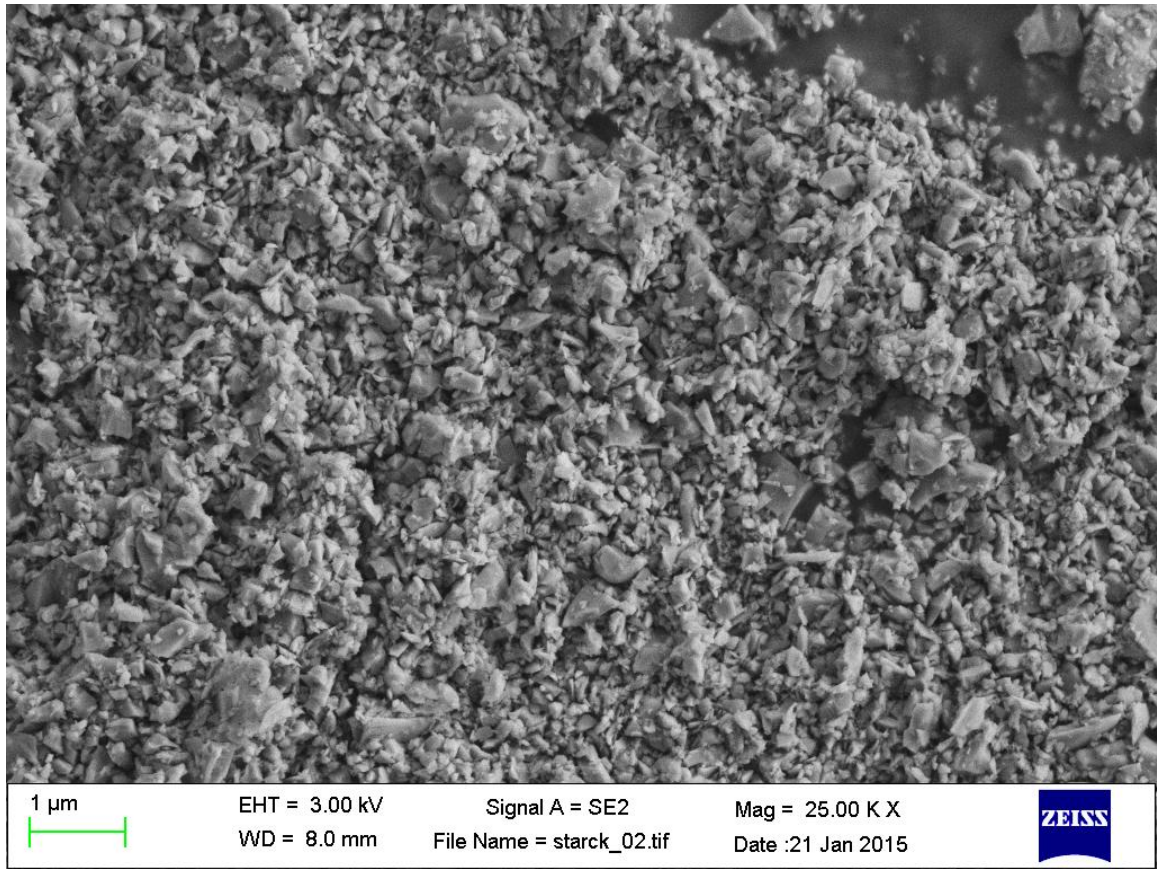


Figure 17. HC-SiC powder micrograph showing uniform submicron particle size

5.2. Production of Dense Silicon Carbide Samples

5.2.1. Selection of Optimum Sintering Conditions

5.2.1.1. HC-SiC Sintering Study

Work done on a project prior to this thesis had focused on producing custom silicon carbide samples using different processing methods and additives. These samples were made using the HC-SiC powder with carbon and boron carbide additives from various sources. Additionally, several different processing methods were also explored including dry mixing, wet mixing, ball milling, and filter pressing before densification using spark plasma sintering with different heating profiles. While these samples all

showed high density and elastic properties, FESEM examination revealed that the microstructures tended to be dominated by very large, elongated grains.

In order to determine the optimum sintering conditions to use with this powder system, a sintering study was performed to try to reduce the grain size and aspect ratio. The Reduced Grain Size Test (RGST) series samples were made using H.C. Starck UF-25 silicon carbide, Fisher lamp black carbon and either H.C. Starck HD20 boron carbide or a boron carbide powder synthesized at Rutgers designated SF8. 23 RGST samples were prepared and densified using SPS. The SPS cycles were systematically changed in order to find the combination of time and temperature to get the most uniform microstructure with smallest average grain size. Different amounts and types of boron carbide additives were also used to find the most effective composition.

To make the RGST series powders, the silicon carbide, boron carbide, and lamp black were ball milled in ethanol for 24 hours in a polyethylene container. For RGST 1 – 20, the commercial H.C. Starck boron carbide powder was used, while RGST 21 – 23 used the Rutgers powder. Most of the RGST samples were made using 1.5% carbon and 0.5% B₄C additives. RGST 12 – 15 and 18 – 20 were made with 1.5% carbon and 0.25% B₄C additives. After milling, the powders were sieved to remove the ball mill media, pan dried, and left to dry in an oven at 115°C overnight.

The samples were then densified in a Thermal Technology SPS 10-4 spark plasma sintering unit in argon atmosphere using five grams of powder in a graphite die lined with graphite foil. The samples were sintered by first heating to 1400°C at 200°C per minute under 50 MPa uniaxial pressure and holding for either 1 or 30 minutes. The samples were then heated to between 1900°C and 2000°C at 200°C per minute under 50 MPa pressure

and held for between 2 and 15 minutes. The sintering temperature and dwell time for each sample are shown below in Table 6 and Figure 18. The temperature was measured using an optical pyrometer aimed at a hole drilled into the side of the graphite die. After the sintering cycle was complete the pressure was released and the system was allowed to cool and the samples removed.

Table 6. RGST Series sintering temperature and dwell time

Sample	Time at 1400°C	Dwell Temperature	Dwell Time	Density (g/cc)
RGST 1	30 min	2000°C	2 min	3.20
RGST 2	30 min	2000°C	5 min	3.20
RGST 3	1 min	2000°C	2 min	3.21
RGST 4	1 min	2000°C	5 min	3.20
RGST 5	30 min	1950°C	2 min	3.21
RGST 6	1 min	1950°C	2 min	3.18
RGST 7	1 min	1950°C	5 min	3.20
RGST 8	30 min	1950°C	5 min	3.21
RGST 9	30 min	1925°C	2 min	3.05
RGST 10	30 min	1900°C	2 min	3.03
RGST 11	30 min	1900°C	5 min	3.13
RGST 12	30 min	1900°C	10 min	3.19
RGST 13	30 min	1950°C	2 min	3.16
RGST 14	30 min	1900°C	10 min	3.19
RGST 15	30 min	1950°C	5 min	3.21
RGST 16	30 min	1900°C	12 min	3.18
RGST 17	30 min	1900°C	15 min	3.18
RGST 18	30 min	1950°C	3.5 min	3.20
RGST 19	30 min	1900°C	15 min	3.20
RGST 20	30 min	1900°C	12 min	3.20
RGST 21	30 min	1900°C	10 min	3.15
RGST 22	30 min	1900°C	12 min	3.19
RGST 23	30 min	1900°C	15 min	3.20

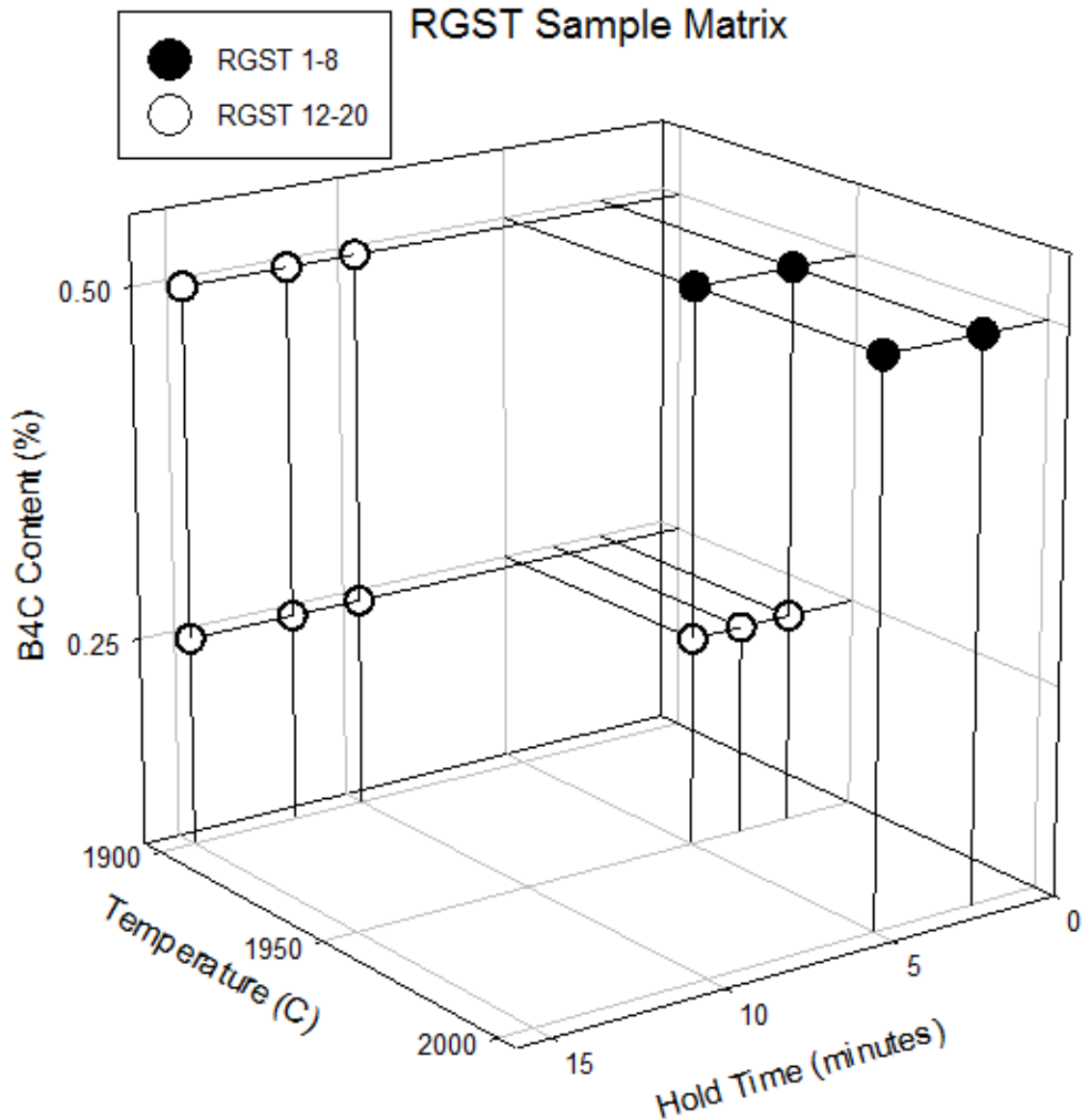


Figure 18. RGST sample matrix

After densification, the samples were sandblasted to remove the graphite foil and the faces were ground flat using a 125 μm diamond grinding wheel. The samples are approximately 20 mm in diameter and 5 mm thick. The densities of the samples were determined using Archimedes' method. The samples were sectioned and polished to a 0.25 μm finish for FESEM imaging. A polished piece from each sample was etched in boiling Murakami's reagent in order to better view the sample microstructure.

Figure 19 and Figure 20 below show FESEM images of RGST samples 1 – 8. Samples 1 – 4 were sintered at 2000°C for 2 or 5 minutes with an intermediate temperature hold for 1 or 30 minutes at 1400°C. The samples that were held for 2 minutes at high temperature show some exaggerated grain growth with some large grains several tens of microns in length but mainly smaller grains. The samples held for 5 minutes show a microstructure dominated by large grains with smaller grains filling in the space between them. Samples 5 – 8 were sintered at 1950°C for 2 or 5 minutes with an intermediate temperature hold for 1 or 30 minutes at 1400°C. At this lower temperature, the average grain size and number of large grains is reduced significantly. As the dwell temperature and time is increased, grain growth is enhanced and the microstructure becomes dominated by larger grains. This is consistent with the findings of other work in silicon carbide [17, 46] and ceramics in general.[31, 33]

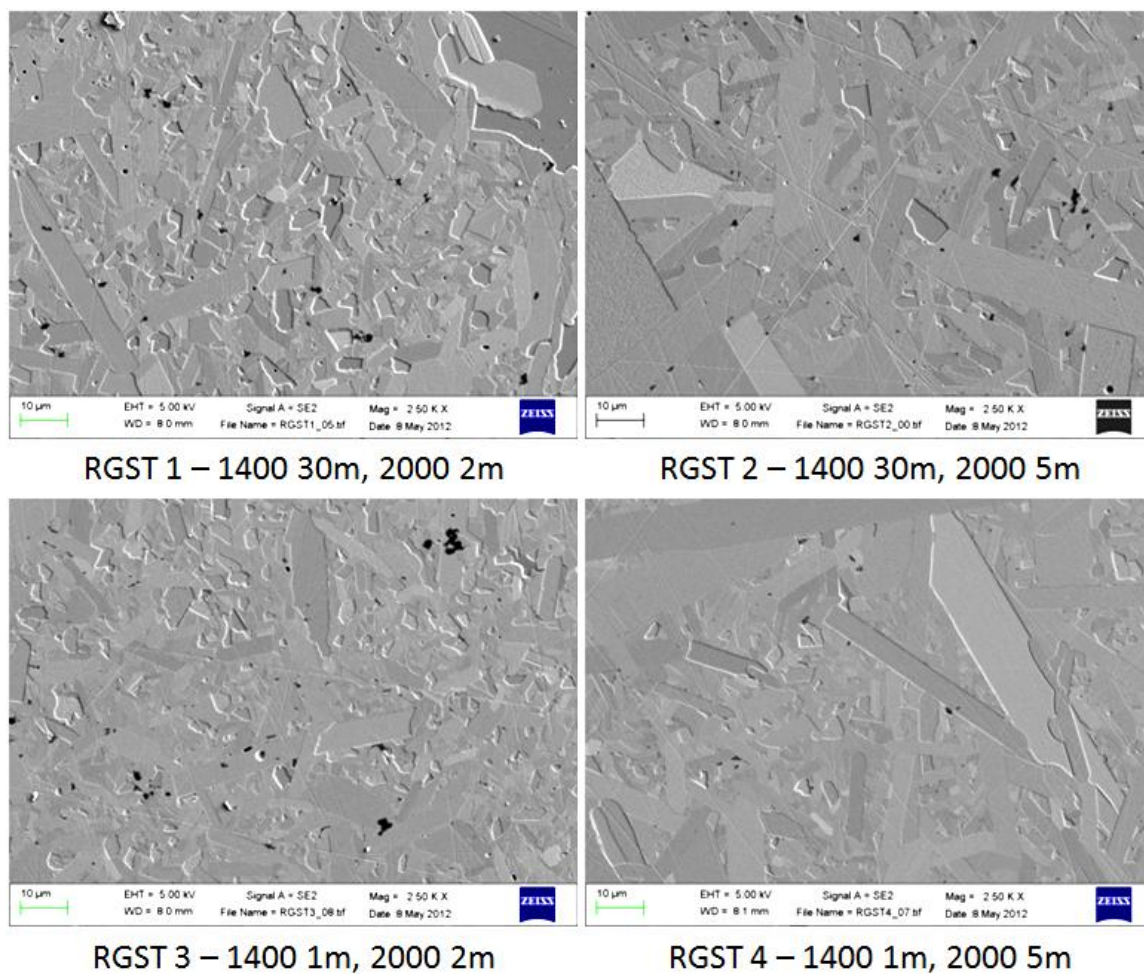


Figure 19. RGST 1 – 4 FESEM images

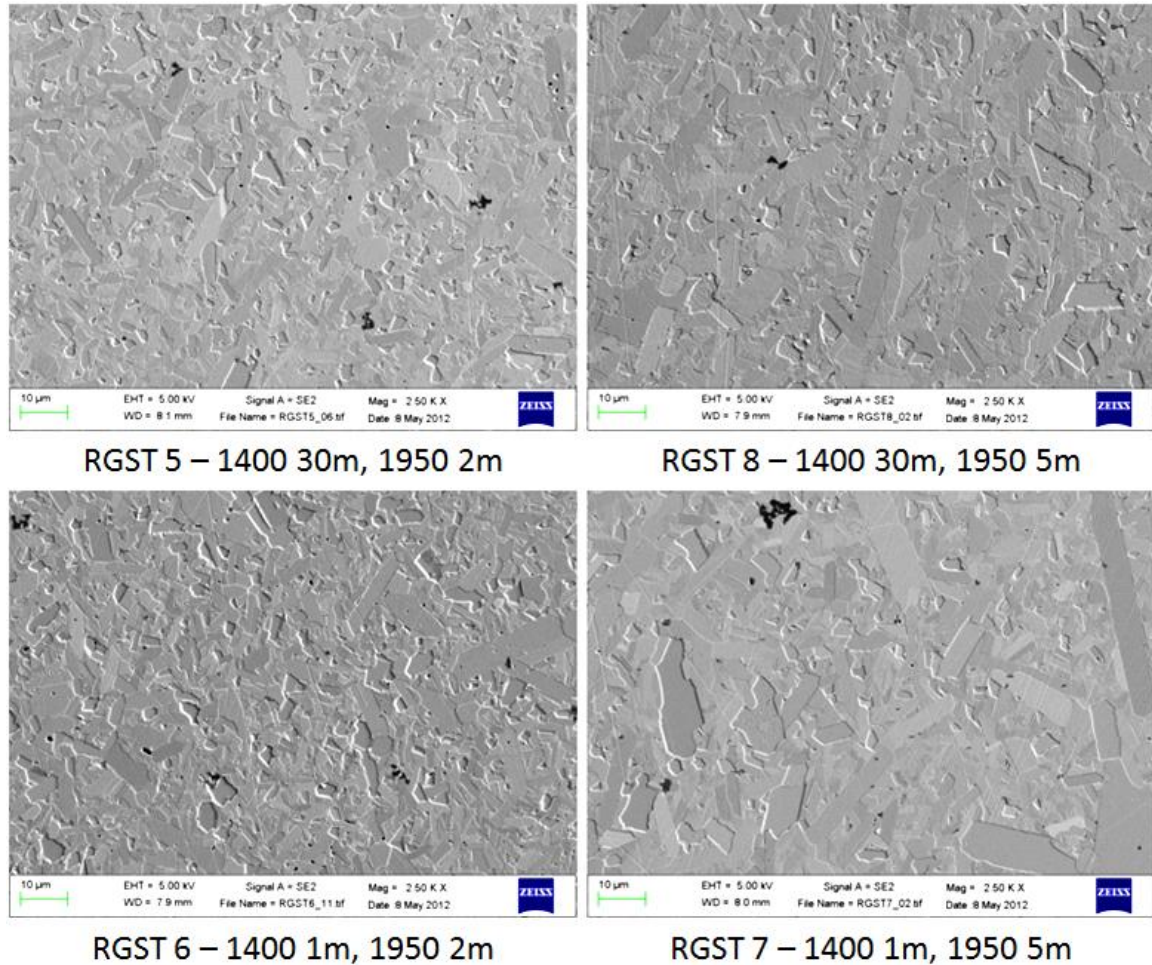


Figure 20. RGST 5 – 8 FESEM images

Figure 21 and Figure 22 below show FESEM images of RGST samples 12 – 20, comparing samples that include 0.5% B_4C additive with samples containing 0.25% B_4C . Samples 12 and 14 were sintered at 1900°C for 10 minutes with an intermediate temperature hold for 30 minutes at 1400°C. Samples 8 and 15 were sintered at 1950°C for 5 minutes with an intermediate temperature hold for 30 minutes at 1400°C. Samples 16 and 20 were sintered at 1900°C for 12 minutes with an intermediate temperature hold for 30 minutes at 1400°C. Samples 17 and 19 were sintered at 1900°C for 15 minutes with an intermediate temperature hold for 30 minutes at 1400°C. The samples that were sintered at 1900°C show much smaller average grain size than those sintered at higher

temperatures and very few grains longer than 10 – 15 μ m. Comparing samples that have different amounts of B₄C additive, it is clear that the samples containing 0.25% B₄C exhibit a much higher frequency of large, high aspect ratio grains and slightly more porosity than those with 0.5% B₄C.

Figure 23 below shows FESEM images of RGST samples 21 – 23 which were made using the same SPS cycles as RGST 12, 16, and 17 (1900°C for 10, 12, or 15 minutes respectively) but using 0.5% Rutgers SF8 B₄C instead of the H.C. Starck HD20 commercial B₄C. They show similar microstructures to the previous RGST samples, but there appear to be fewer agglomerates of the B₄C additive, which appear in the FESEM images as dark gray or black. Due to the limited availability of Rutgers B₄C powders at the time and the relatively small differences in microstructures, it was decided that all future samples would be made using the commercial boron carbide powder as the ease and consistency of using it would outweigh the slight benefits of using the Rutgers powder.

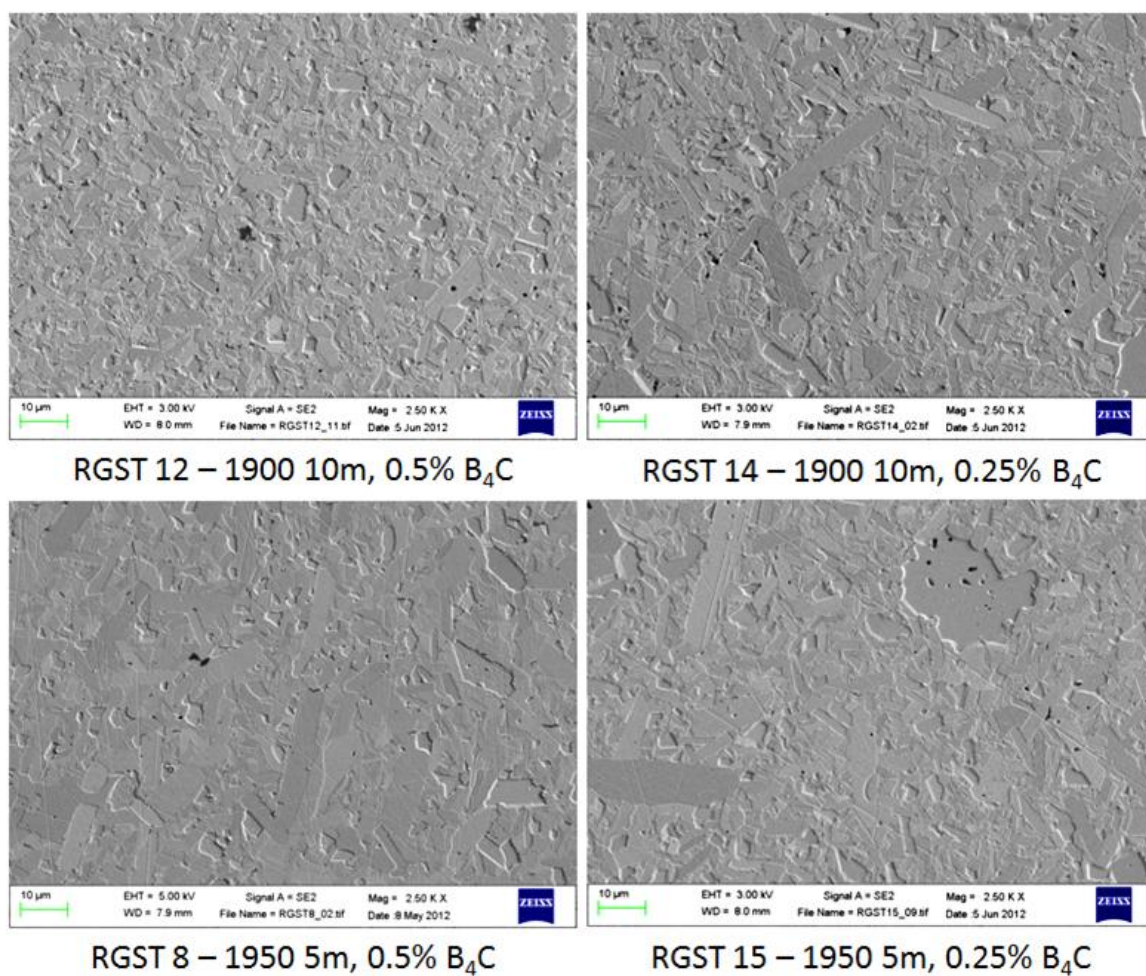


Figure 21. RGST 8 – 15 FESEM images

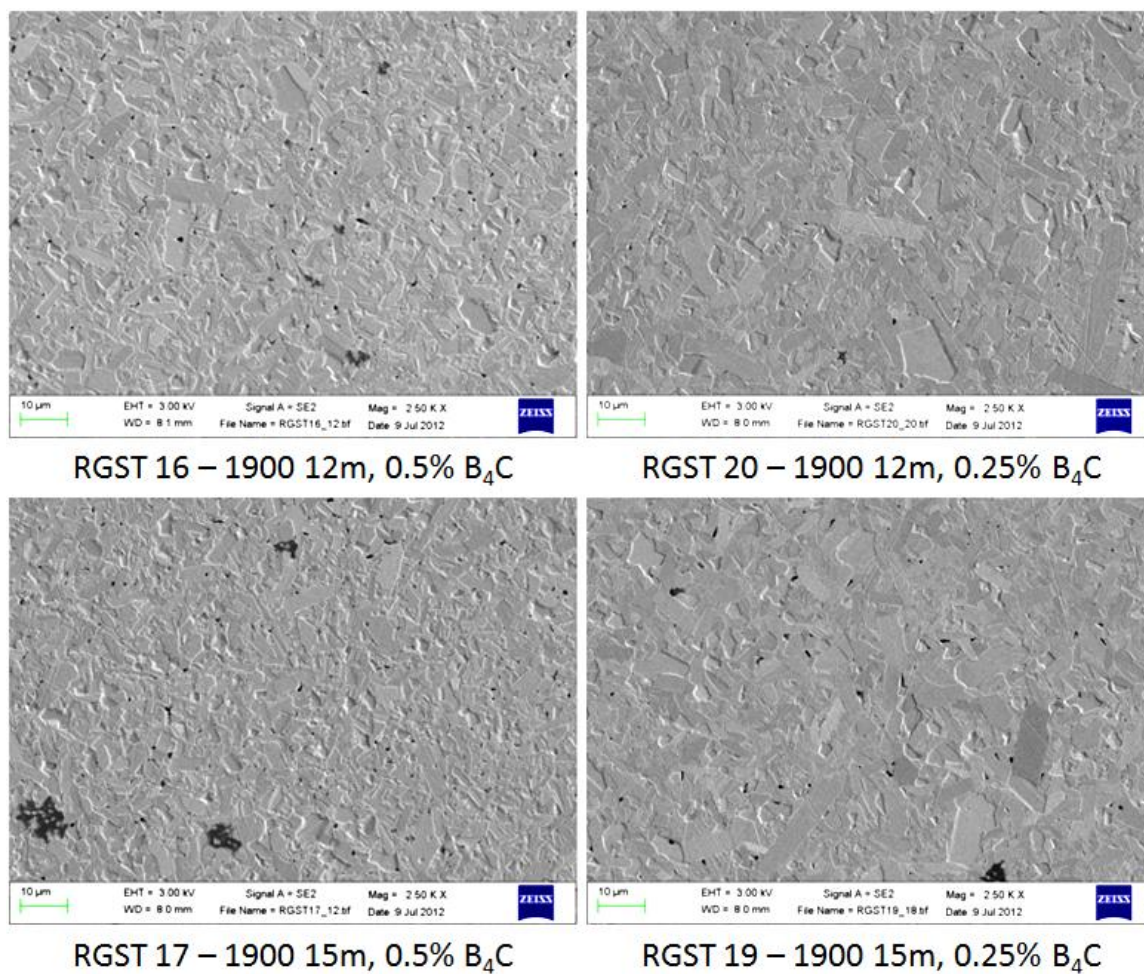


Figure 22. RGST 16 – 20 FESEM images

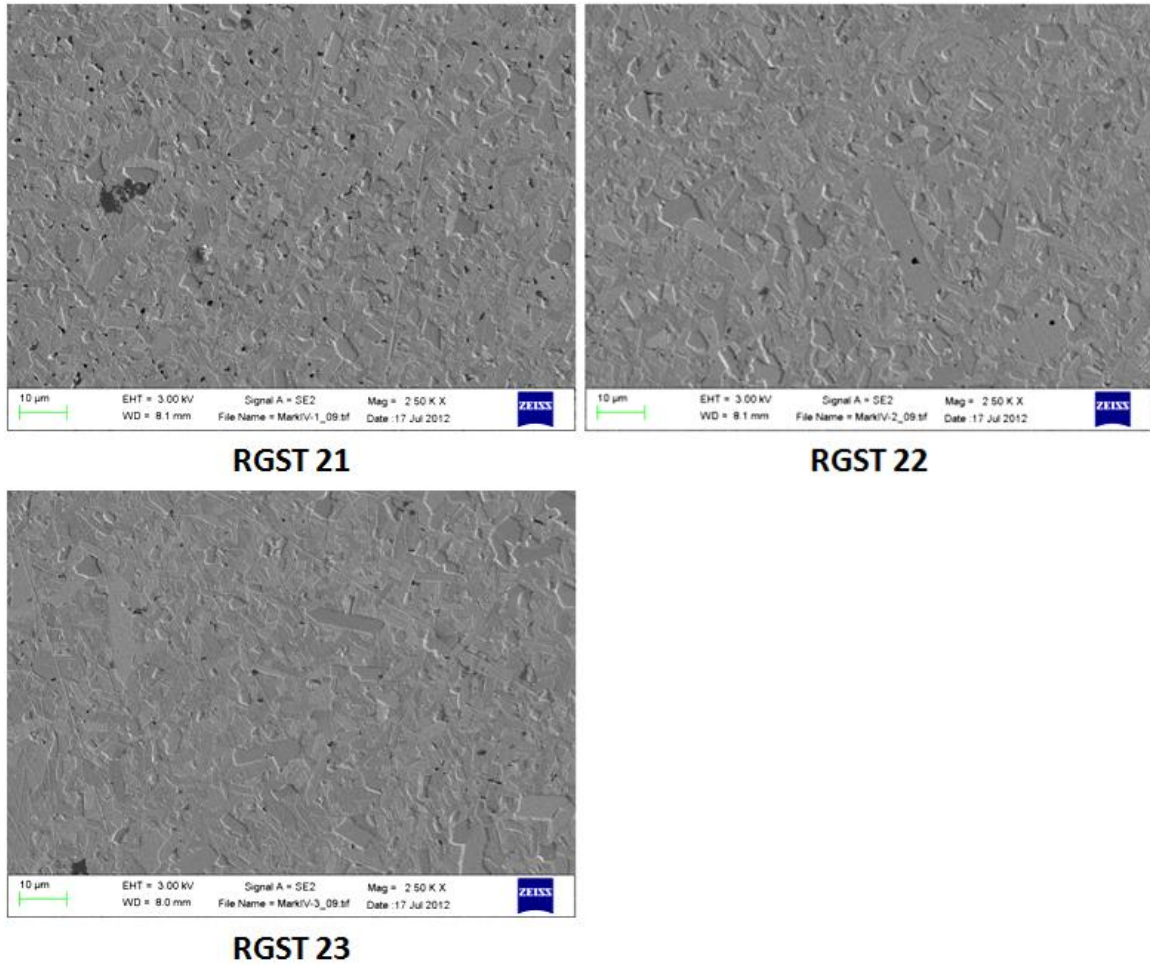


Figure 23. RGST 21 – 23 FESEM images

After comparing the RGST series samples, it was determined that the SPS conditions that produced the best SiC microstructure with the HC-SiC was a 30 minute hold at 1400°C followed by a 15 minute dwell at 1900°C. It was also determined that 0.5% B₄C additive was preferable to 0.25% and resulted in a more favorable microstructure. These conditions were able to fully densify the silicon carbide without much exaggerated grain growth, resulting in a fairly fine grained microstructure.

5.2.1.2. SG-SiC Sintering Study

To determine the optimum sintering conditions to use with the SG-SiC powder system, a sintering study was performed based on the results of the RGST study. Several samples were made using the SG-SiC silicon carbide, Fisher lamp black carbon and H.C. Starck HD20 boron carbide. 30 samples were prepared and densified using SPS. The SPS cycles were systematically changed in order to find the best combination of time, temperature, and pressure to get the most uniform microstructure with smallest average grain size.

Samples were made with variations in applied pressure, sintering temperature, and dwell time at the sintering temperature. To make these samples, SG-SiC powder was mixed with the boron carbide and carbon additives by ball milling in ethanol for 24 hours in a polyethylene container. Each sample used the same Saint Gobain SiC powder, 1.5% carbon, and 0.5% B₄C. After milling, the powders were sieved to remove the ball mill media, pan dried, ground to uniformity with a mortar and pestle, and left to dry in an oven at 115°C overnight.

The samples were then densified in a Thermal Technology SPS 10-4 spark plasma sintering unit using 6.5 grams of powder in a graphite die lined with graphite foil. The samples were sintered by first heating under vacuum to 1400°C at 200°C per minute under 10 – 50 MPa uniaxial pressure and holding for 5 minutes. After 5 minutes at 1400°C, the chamber was backfilled with argon. The samples were then heated to 1900°C – 2000°C at 200°C per minute under 10 – 50 MPa pressure and held for 5 – 65 minutes. Samples were sintered at temperatures between 1900°C and 2000°C in 25°C intervals. At each temperature, samples were held for between 5 and 65 minutes in 5 minute intervals.

Five samples were made at 1900°C for 15 minutes with varying amounts of applied pressure, between 10 and 50 MPa in 10 MPa intervals. All other samples were made with 50 MPa of applied pressure.

The temperature of the sample during sintering was measured using an optical pyrometer aimed at a small hole drilled about halfway into the side of the graphite die. After the sintering cycle was complete the pressure was released and the system was allowed to cool and the samples were removed. The details of the SPS conditions used for each sample are shown in below in Figure 24 and Table 7. The samples were assigned names based on the format X_Y_Z where X is the sintering temperature, Y is the dwell time in minutes, and Z is the applied pressure.

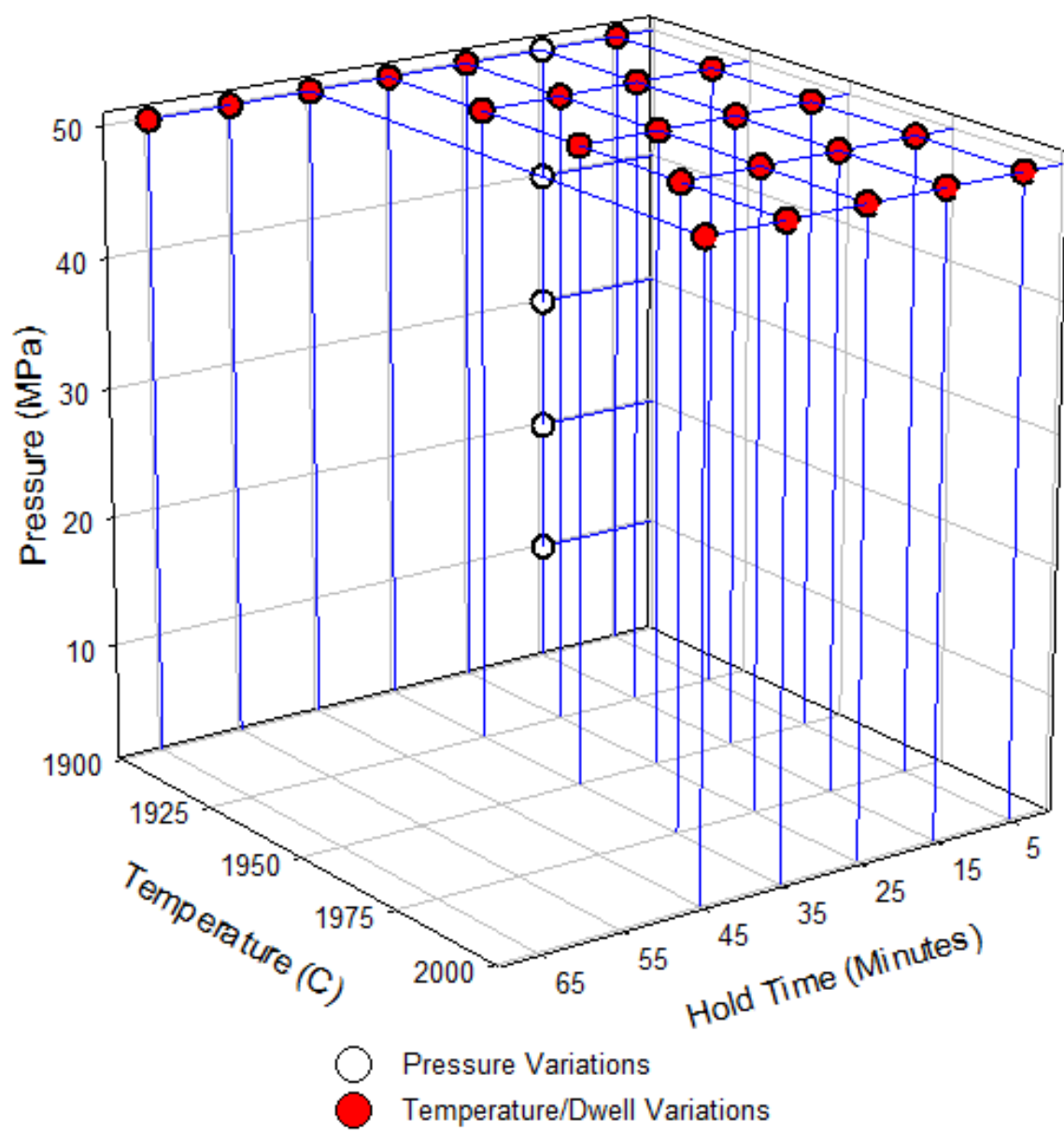


Figure 24. SPS conditions used for each sample

Table 7. SPS conditions used for each sample and resulting sample density

Sample	Applied Pressure (MPa)	Sintering Temp. (°C)	Dwell Time (min)	Density (g/cm ³)
Pressure Variations				
1900_15_50	50	1900	15	3.16
1900_15_40	40	1900	15	3.14
1900_15_30	30	1900	15	3.09
1900_15_20	20	1900	15	3.08
1900_15_10	10	1900	15	2.94
Temperature/Dwell Variations				
1900_5_50	50	1900	5	3.18
1900_15_50	50	1900	15	3.18
1900_25_50	50	1900	25	3.18
1900_35_50	50	1900	35	3.18
1900_45_50	50	1900	45	3.18
1900_55_50	50	1900	55	3.18
1900_65_50	50	1900	65	3.18
1925_5_50	50	1925	5	3.19
1925_15_50	50	1925	15	3.19
1925_25_50	50	1925	25	3.19
1925_35_50	50	1925	35	3.19
1950_5_50	50	1950	5	3.19
1950_15_50	50	1950	15	3.19
1950_25_50	50	1950	25	3.19
1950_35_50	50	1950	35	3.19
1975_5_50	50	1975	5	3.19
1975_15_50	50	1975	15	3.19
1975_25_50	50	1975	25	3.19
1975_35_50	50	1975	35	3.19
2000_5_50	50	2000	5	3.19
2000_15_50	50	2000	15	3.18
2000_25_50	50	2000	25	3.19
2000_35_50	50	2000	35	3.19
2000_45_50	50	2000	45	3.19

After densification, the samples were sandblasted to remove the graphite foil and the faces were ground flat. The final dimensions of the samples were approximately

20 mm in diameter and 6 mm thick. The densities of the samples were determined using Archimedes' method. Each sample was sectioned and polished to a 0.25 μm finish for FESEM imaging. A polished piece from each sample was etched in boiling Murakami's reagent in order to better view the sample microstructure.

Figure 25 below shows FESEM images of the pressure variation samples. The samples all show similar size and shape of the SiC grains with relatively small, equiaxed grains and small, evenly distributed secondary phase particles of unreacted B_4C and carbon. The main differences are in the amount of porosity observed in the samples sintered at lower pressures. Very little if any porosity is seen in the samples sintered at 50 and 40 MPa. Those sintered at 30 and 20 MPa show a moderate amount of porosity and the sample sintered at 10 MPa shows a significant level of porosity. This increase in porosity is also reflected in the differences in density between samples.

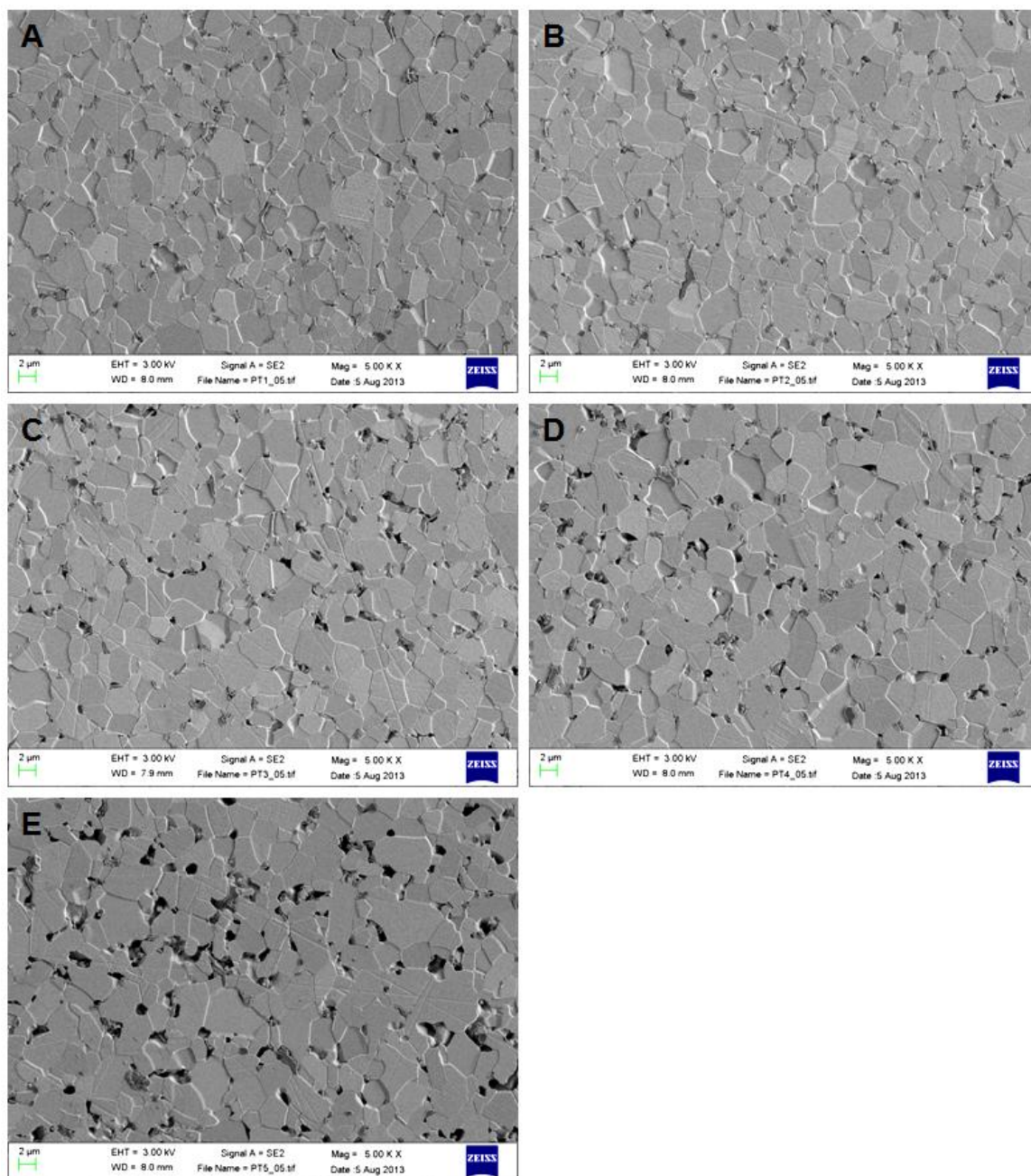


Figure 25. FESEM images of samples sintered with 50 MPa (A), 40 MPa (B), 30 MPa (C), 20 MPa (D), and 10 MPa (E) of applied uniaxial pressure at 5000x magnification

Figure 26 below shows FESEM images of samples sintered at varied temperatures. At lower temperatures, the microstructures of each sample appear quite

similar to each other. They show relatively small, equiaxed grains and small, evenly distributed secondary phase particles. At higher temperatures, the grain size increases and the SiC grains start to become elongated. This is most apparent in the sample sintered at 2000°C, shown in Figure 26e.

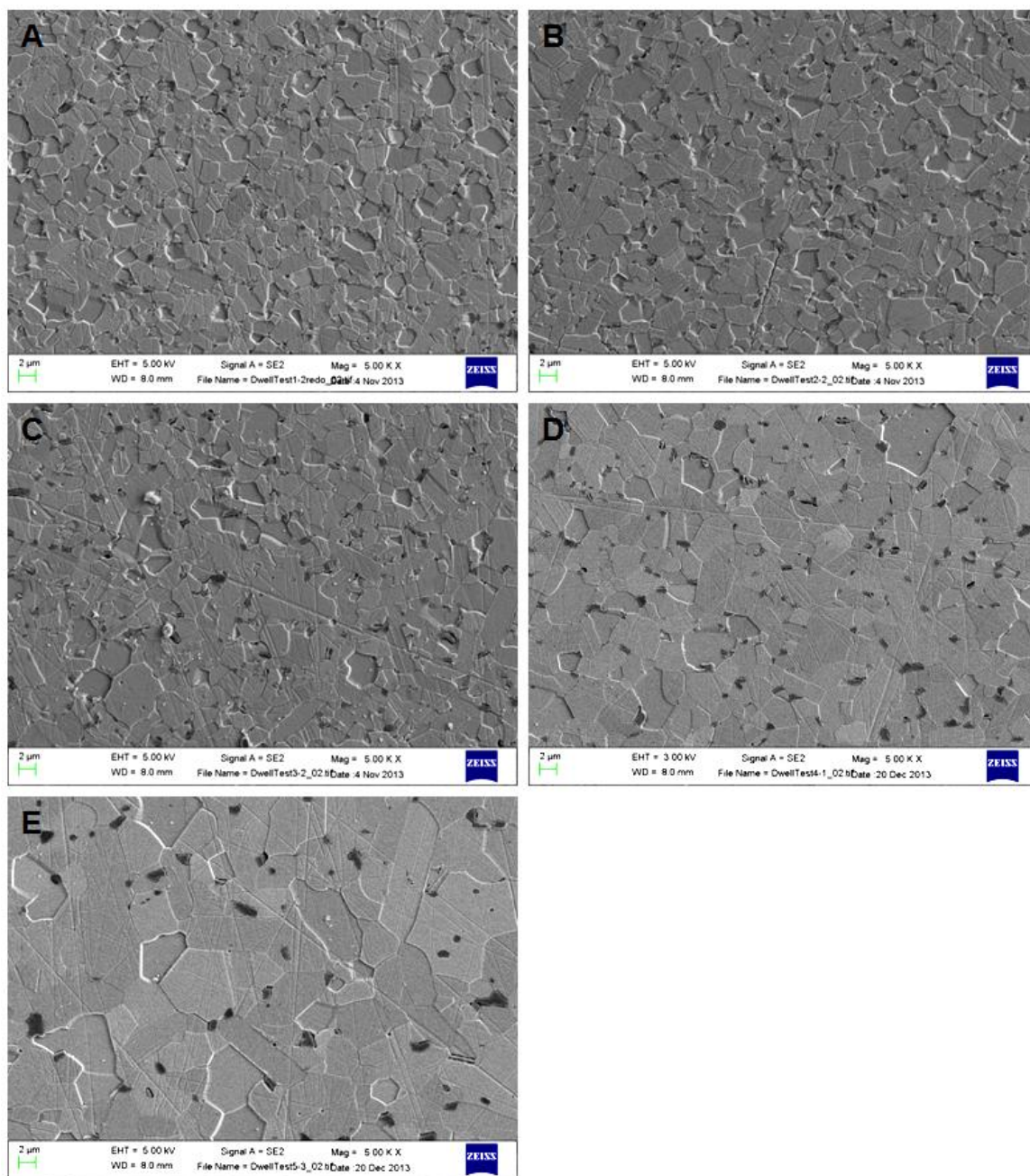


Figure 26. FESEM images at 5000x magnification of samples sintered at 1900°C (A), 1925°C (B), 1950°C (C), 1975°C (D), and 2000°C (E) for 5 minutes

Figure 27 below shows FESEM images of samples sintered at 1900°C for varying lengths of time. The samples sintered at 1900°C all show microstructures with mainly equiaxed grains. There is some increase in grain size as the samples are sintered for

longer periods of time as well as some slight elongation of grains, but neither the grain size increase nor the elongation is extreme. Samples sintered with higher dwell temperatures showed similar behavior with increasing dwell time, but the grain sizes typically grew larger as the dwell temperatures increased.

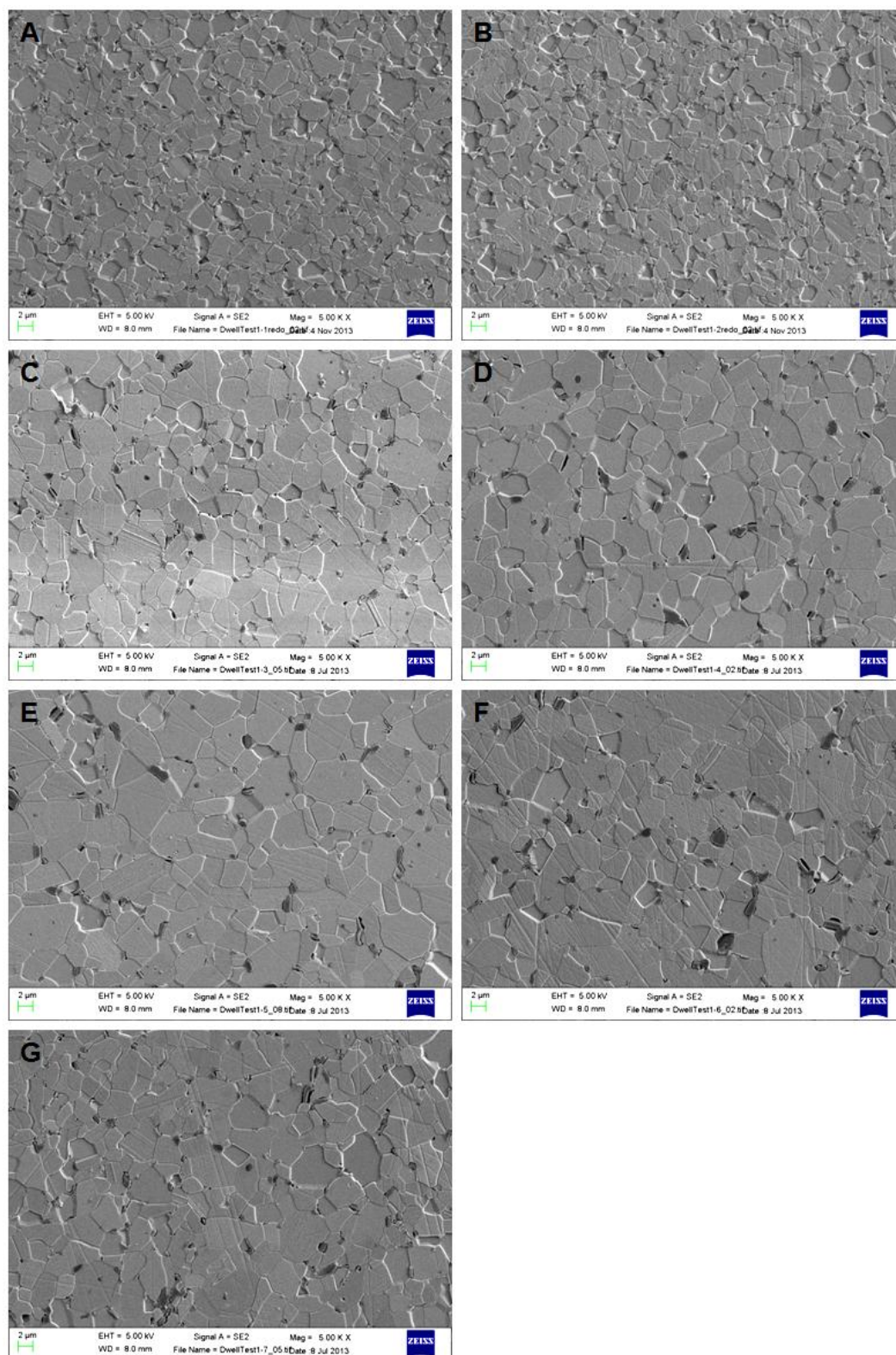


Figure 27. FESEM images at 5000x magnification of samples sintered at 1900°C for 5 (A), 15 (B), 25 (C), 35 (D), 45 (E), 55 (F), and 65 (G) minutes

After comparing the samples made in the SG-SiC sintering study, it was determined that the same SPS conditions that produced the best SiC microstructure in the HC-SiC system could also be used with the SG-SiC. A 15 minute dwell at 1900°C and 50 MPa was able to fully densify both silicon carbide powders without exaggerated grain growth, resulting in fairly fine grained microstructures. As such, the optimum SPS sintering conditions that were chosen to use for the samples in this thesis are shown below in Figure 28. The sintering cycle starts by ramping up to 600°C and 10 MPa of pressure and holding there until the pyrometer starts to read the actual temperature of the die. The sample is then heated under vacuum to an intermediate dwell temperature of 1400°C at 200°C per minute, ramping up to 50 MPa of uniaxial pressure at 10 MPa per minute and holding there for 30 minutes. After this intermediate dwell step, the chamber is backfilled with argon. The furnace is then ramped to 1900°C at 200°C per minute and held at that temperature for 15 minutes, maintaining 50 MPa of pressure. The power supplies are then shut off and the sample is allowed to cool for 30 – 45 minutes so that it can be safely removed from the unit.

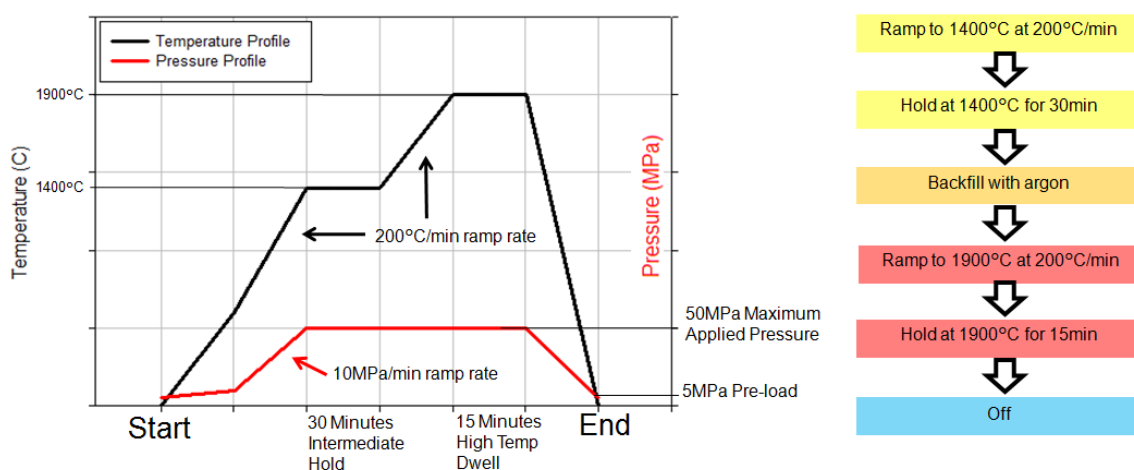


Figure 28. Optimum spark plasma sintering conditions

5.2.2. Powder Preparation

The matrix of silicon carbide samples that were produced for this thesis is shown below in Table 8.

Table 8. Silicon Carbide Sample Matrix

Sample Series	SiC Powder	Oxygen Content	Carbon Added	Notes
HC-AW-series	HC Starck	0.5% - 3.36%	1.5%	HC Starck powder washed and aged to different O ₂ content
SG-AW-series	Saint Gobain	0.2% - 0.98%	1.0%	St. Gobain powder washed and aged to different O ₂ content
HC-LBC-series	HC Starck	1.7%	1.5% - 4.5%	HC Starck powder with different C amounts added (lamp black)
SG-LBC-series	Saint Gobain	0.3%	0% - 2%	St. Gobain powder with different C amounts added (lamp black)
HC-PRC-series	HC Starck	1.7%	1.5% - 4.5%	HC Starck powder with different C amounts added (phenolic resin)
SG-PRC-series	Saint Gobain	0.3%	0% - 2%	St. Gobain powder with different C amounts added (phenolic resin)

The powders used in this thesis were prepared by mixing the SiC powder with the boron carbide and carbon additives. Two different types of carbon additives were used – a particulate lampblack (Fisher Scientific), and a liquid phenolic resin (VARCUM 29353, Durez Corp.). For all of the samples, SiC powder was combined with 0.5% by weight of H.C. Starck HD20 boron carbide, and varying amounts of carbon between 0% and 4.5%. A 50 gram batch of powder was produced for each sample composition.

When using the particulate carbon, as in the SG-AW, HC-AW, SG-LBC, and HC-LBC-Series samples, the combined powders were mixed by ball milling in ethanol for 24 hours in a polyethylene container with silicon carbide media. After milling, the powders were sieved to remove the ball mill media, pan dried, and ground to uniformity with a

mortar and pestle. The compositions of the LBC-Series samples are shown below in Table 9. The compositions of the AW-Series samples are shown below in Table 10.

Table 9. LBC-Series sample compositions

Sample	SiC (g)	B₄C (g)	Carbon (g)
SG-LBC-0C	49.75	0.25	0
SG-LBC-0.5C	49.50	0.25	0.25
SG-LBC-1.0C	49.25	0.25	0.50
SG-LBC-1.5C	49.00	0.25	0.75
SG-LBC-2.0C	48.75	0.25	1.00
HC-LBC-1.5C	49.00	0.25	0.75
HC-LBC-3.0C	48.25	0.25	1.50
HC-LBC-4.5C	47.50	0.25	2.25

Table 10. AW-Series sample compositions

Sample	SiC (g)	B₄C (g)	Carbon (g)
SG-AW-0.22%	49.25	0.25	0.50
SG-AW-0.38%	49.25	0.25	0.50
SG-AW-0.98%	49.25	0.25	0.50
HC-AW-0.60%	49.00	0.25	0.75
HC-AW-1.69%	49.00	0.25	0.75
HC-AW-3.36%	49.00	0.25	0.75

When using the liquid phenolic resin, the weight ratios of the carbon additives had to be adjusted. To be comparable to samples made with lamp black as the carbon source, powders were prepared with the SG-SiC to have 0.5, 1.0, and 1.5 weight percent carbon, and HC-SiC to have 1.5, 3.0, and 4.5 weight percent carbon. Thermogravimetric analysis (TGA) was performed on the resin and it was determined that the char yield was approximately 43% as shown in Figure 29. Previous work performed in the CCOMC using this resin suggested that about 10% of the resin would be lost during filter pressing. As such, the weight of phenolic resin added was 2.58 times the amount of carbon that was desired in the final formulation. The amount of material used in each sample is shown in Table 11.

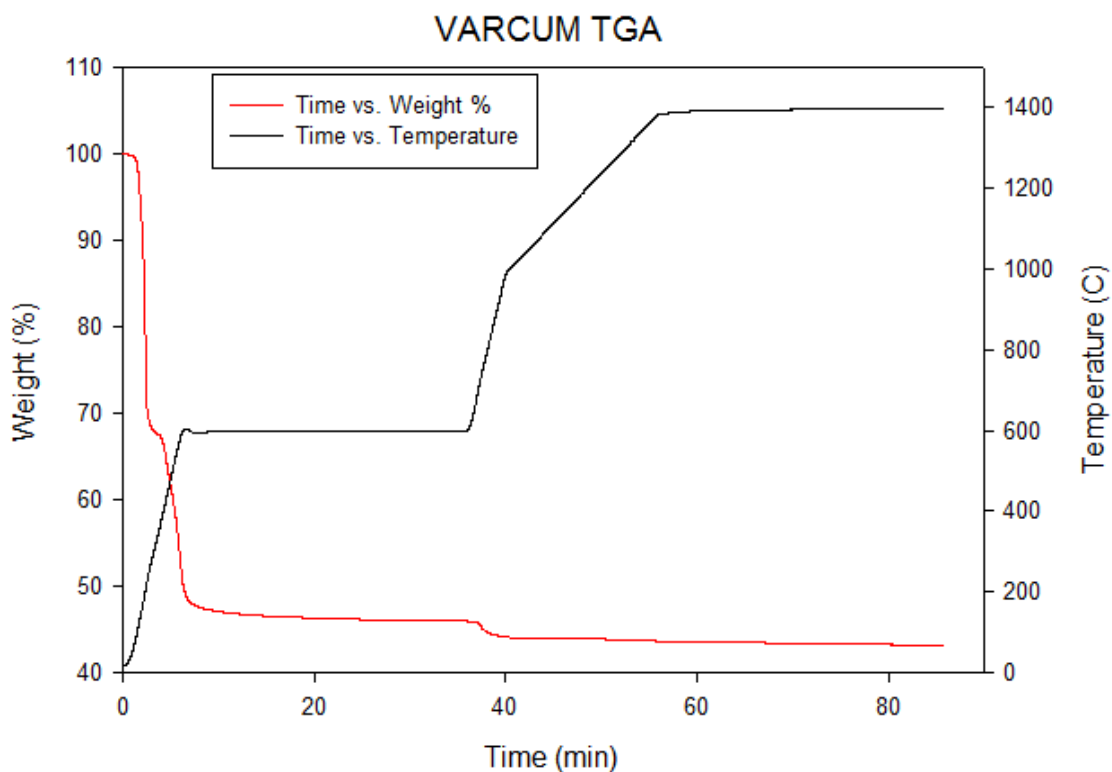


Figure 29. VARCUM phenolic resin TGA data

Table 11. PRC-Series sample compositions

Sample	SiC (g)	B ₄ C (g)	Phenolic Resin (g)	Carbon Equivalent (g)
SG-PRC-0.5C	49.50	0.25	0.65	0.25
SG-PRC-1.0C	49.25	0.25	1.29	0.50
SG-PRC-1.5C	49.00	0.25	1.94	0.75
HC-PRC-1.5C	49.00	0.25	1.94	0.75
HC-PRC-3.0C	48.25	0.25	3.88	1.50
HC-PRC-4.5C	47.50	0.25	5.81	2.25

To prepare the powders, the solid SiC and B₄C powders were first combined in a plastic Nalgene container. The liquid phenolic resin was mixed with water in a separate container and sonicated. The liquid mixture was then added to the dry powder along with approximately 0.22 g of ammonium hydroxide as a dispersant. SiC milling media was added and the container was sealed and left on a ball mill to mix for 24 hours. After

mixing, the media was removed and the slurry was filter pressed at 35 psi to remove the excess water. The resulting cake was broken up and dried in an oven at 100°C for an hour, checking every ten minutes to further break up any large chunks. After drying, the material was lightly crushed with a mortar and pestle to create a uniform powder for sintering.

5.2.3. Fabrication of Dense Samples

5.2.3.1. Samples Made Using LBC Carbon Source

The SG-LBC-Series, HC-LBC-Series, SG-AW-Series, and HC-AW-Series samples were densified via SPS in a Thermal Technology SPS 10-4 spark plasma sintering unit. 6.5 grams of powder were loaded in a graphite die with graphite punches, all lined with graphite foil. The samples were sintered by first heating under vacuum to 1400°C at a rate of 200°C/min and the pressure increased to 50 MPa and held for 30 minutes. After 30 minutes at 1400°C, the chamber was backfilled with argon and the samples were heated to 1900°C at 200°C per minute maintaining 50 MPa pressure and held for 15 minutes. After the sintering cycle was complete the pressure was released and the system was allowed to cool and the sample was removed.

5.2.3.2. Samples Made Using PRC Carbon Source

The SG-PRC-Series and HC-PRC-Series samples were densified via SPS in a Thermal Technology SPS 10-4 spark plasma sintering unit. 6.5 grams of powder were loaded in a graphite die with graphite punches, all lined with graphite foil. The samples were sintered by first heating under vacuum to 800°C at 200°C per minute under 20 MPa of uniaxial pressure and holding for one hour to burn off the resin. The temperature was then increased to 1400°C at a rate of 200°C/min and the pressure increased to 50 MPa

and held for 30 minutes. After 30 minutes at 1400°C, the chamber was backfilled with argon and the samples were heated to 1900°C at 200°C per minute maintaining 50 MPa pressure and held for 15 minutes. After the sintering cycle was complete the pressure was released and the system was allowed to cool and the sample was removed.

5.3. Characterization of Dense Silicon Carbide Samples

5.3.1. SG-LBC-Series

5.3.1.1. Microstructure Characterization

Figure 30 shows the microstructures of the SG-LBC series of samples. The samples with lower carbon content show significant amounts of porosity. The samples with 1.0 and 1.5% carbon are nearly fully dense, while the sample with 2.0% carbon shows some slight porosity. While the grain morphology appears to be quite similar between the five samples, the grain size varies as the carbon content changes.

When additional carbon is available to react with the surface oxide present on the silicon carbide the porosity decreases until the ceramic reaches full density at around 1% carbon addition. The grain size also increases up to this point as there are fewer pores to inhibit the grain growth. As the amount of carbon is increased further, the samples retain their high density, but begin to display reduced grain sizes as the residual carbon inclusions prevent the silicon carbide grains from growing as much. These trends are also reflected in Table 12 which lists the average grain size and standard deviation for each sample as measured by the linear intercepts method using at least 100 intercepts on each image.

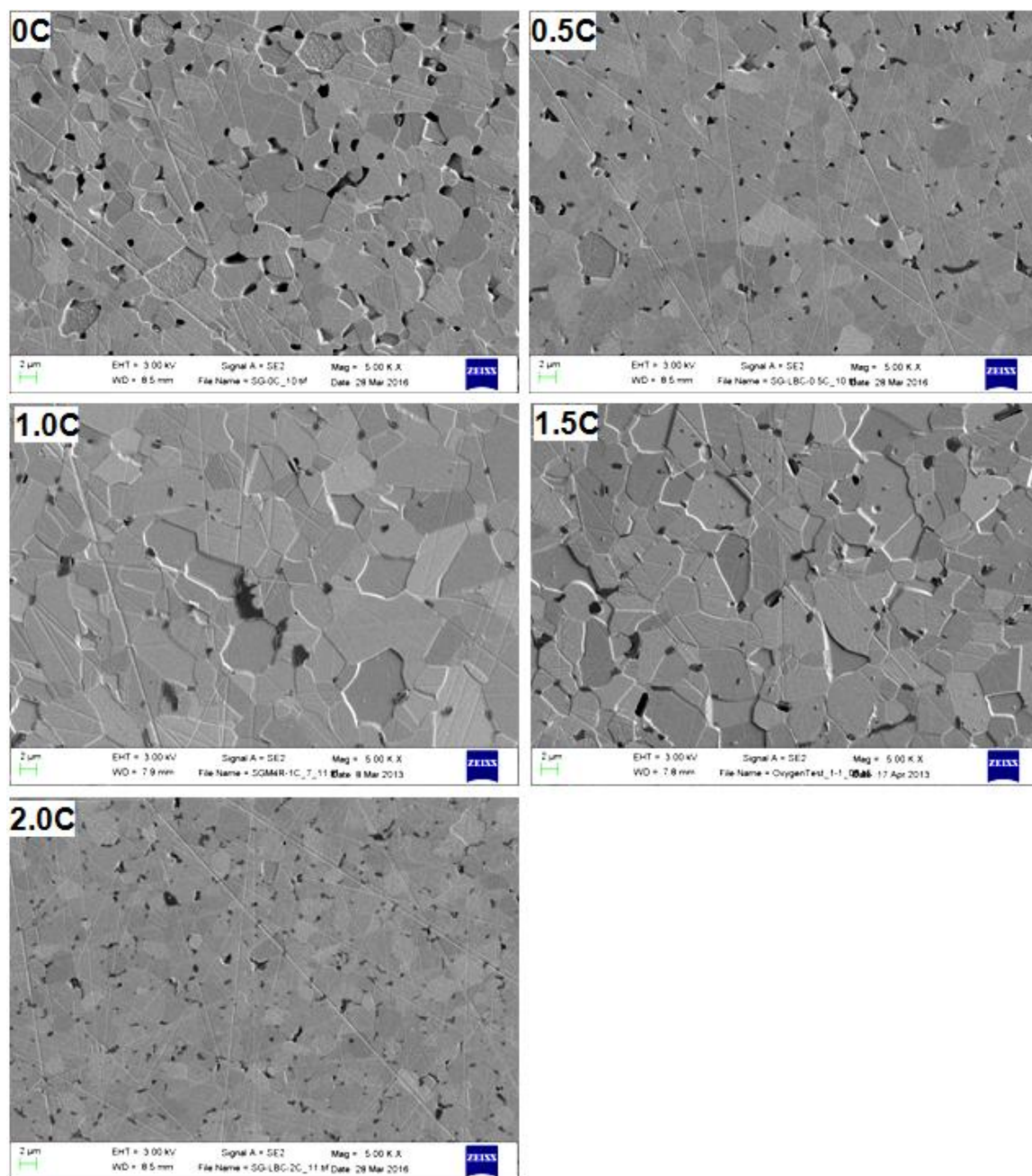


Figure 30. SG-LBC-Series microstructures at 5000x magnification

Table 12. SG-LBC-Series average grain sizes measured by the linear intercepts method

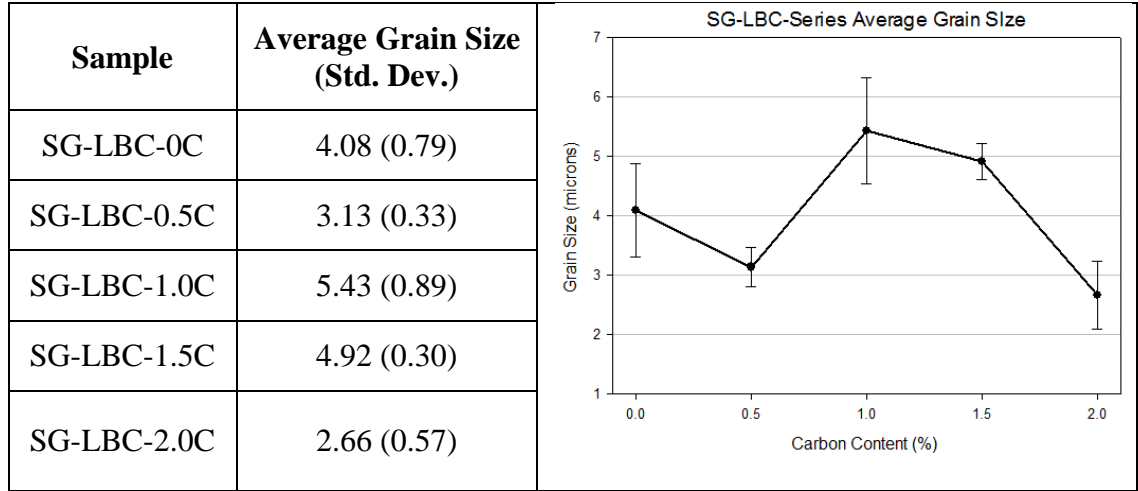


Figure 31 shows EBSD maps of the SG-LBC series of samples. In each of the maps shown, the red color indicates the presence of the 6H SiC polytype and the green color shows the 4H SiC polytype. The black color indicates areas where neither phase found due to the presence of secondary phases, pores, roughness, grain boundaries, or other factors. The investigated areas of each sample are dominated by grains of the 6H polytype while a smaller fraction of the grains are 4H. This is also reflected in Table 13 which shows the phase fractions of each polytype present in the mapped areas. Due to the presence of the black areas mentioned before, the total areas of 6H and 4H do not add up to a full 100%. For all of the samples the ratio of 4H/6H SiC is quite low, between 0.139 – 0.241, which is only slightly higher than the starting powder ratio of 0.109. In this case, it does not appear that the oxygen content, which would decrease as the amount of carbon added increases, has much of an effect on the conversion of SiC from 6H to 4H.

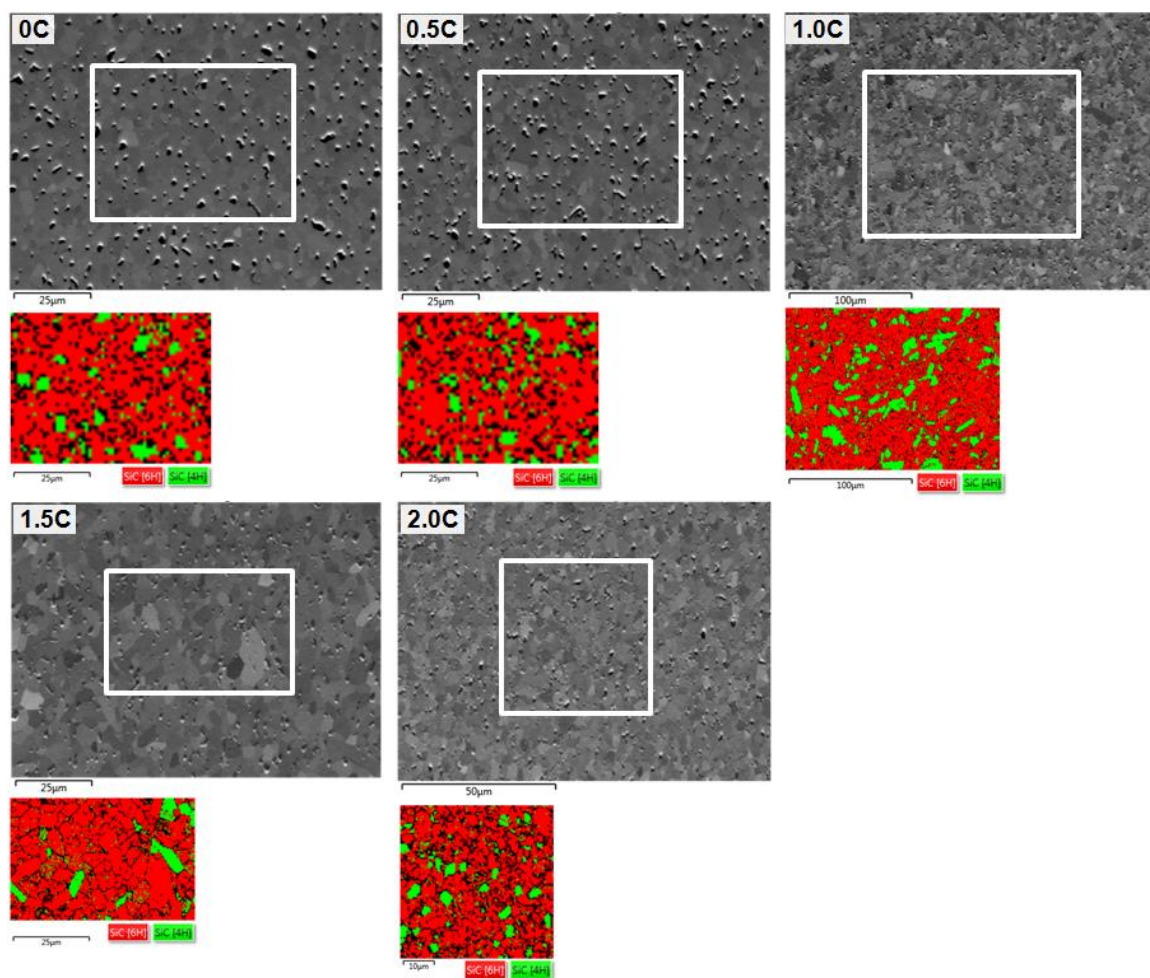


Figure 31. SG-LBC-Series EBSD Maps

Table 13. SG-LBC-Series phase fractions

Sample	Phase Fraction 4H (%)	Phase Fraction 6H (%)	4H/6H ratio
SG-LBC-0C	10	69	0.14
SG-LBC-0.5C	11	69	0.16
SG-LBC-1.0C	17	71	0.24
SG-LBC-1.5C	10	73	0.14
SG-LBC-2.0C	11	62	0.18

5.3.1.2. Mechanical Properties

The densities of the SG-LBC-Series samples were determined using Archimedes' method and the elastic properties were measured using the nondestructive ultrasonic techniques and are shown below in Table 14. The longitudinal and shear sound speeds were measured directly and the Poisson's Ratio and moduli were calculated from these values using the equations described in Section 4.5.2. The elastic properties were plotted against the carbon content as shown below in Figure 32.

Looking at the sample densities, it is apparent that at low added carbon amounts, there is insufficient carbon to fully remove the surface oxygen and full densification is inhibited. At 1.0% added carbon, the density peaks as there is enough carbon to effectively remove the oxygen but not leave much in the microstructure as carbonaceous inclusions. At higher carbon levels, there is more than enough carbon to react with and remove the oxygen so the excess carbon remains in the microstructure as small inclusions. Because the carbon is less dense than SiC, these inclusions reduce the overall sample density. The same general effect is seen in the other elastic properties, where the

modulus is reduced at low carbon contents because of porosity and at high carbon amounts by carbonaceous inclusions.

Table 14. SG-LBC-Series elastic properties

Sample	c_L (m/s)	c_S (m/s)	Poisson Ratio	Density (g/cm^3)	E (GPa)	G (GPa)	K (GPa)
SG-0C	12130	7660	0.17	3.08	424	182	211
SG-LBC-0.5C	11980	7620	0.16	3.09	416	180	204
SG-LBC-1.0C	12100	7720	0.16	3.19	440	190	214
SG-LBC-1.5C	11980	7660	0.16	3.18	431	186	208
SG-LBC-2.0C	11790	7530	0.16	3.13	411	178	199

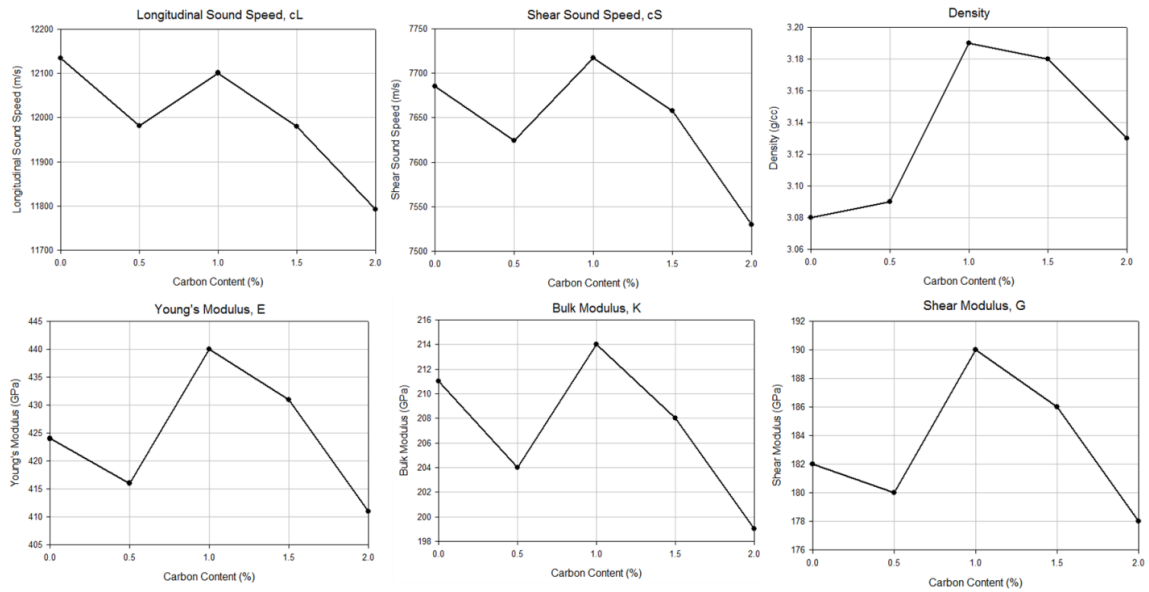


Figure 32. SG-LBC-Series elastic properties vs. carbon content

Knoop microhardness testing was performed on each sample in the SG-LBC series with 10 indents at each of five different loads (100 g, 300 g, 500 g, 1000 g, 2000 g). Load-hardness curves for each sample are shown below in Figure 33. These curves show clearly the indentation size effect that is typically seen in ceramic materials

where the hardness decreases as the load, and therefore indentation size, increases.[68] The hardness values follow the same trend as the elastic properties, where the 1.0% and 1.5% carbon samples have higher values compared with the others. This is again most likely due to the effect of porosity in the lower carbon samples and carbonaceous inclusions in the higher carbon sample. In such cases, both the pores and carbon inclusions are too small and evenly distributed to avoid when indenting the samples, even at the lowest loads.

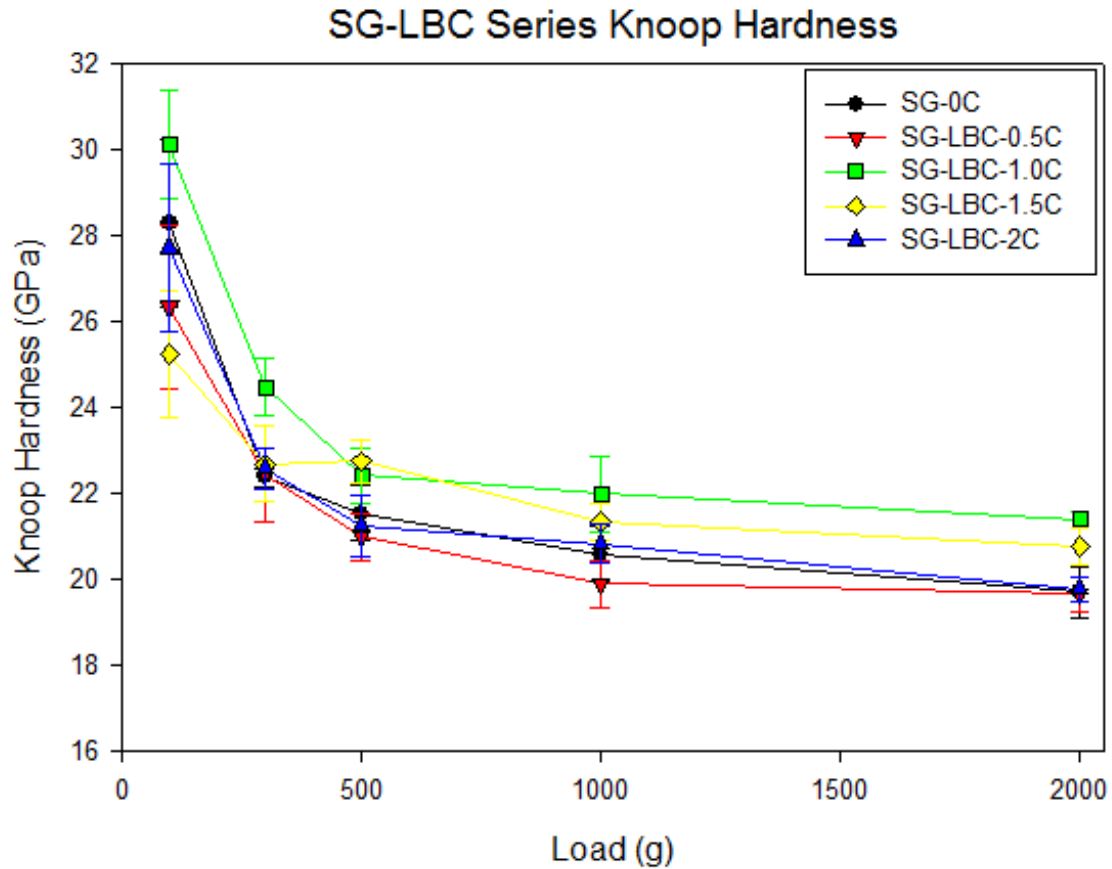


Figure 33. SG-LBC-Series Knoop Hardness curves

The 1000 g load Knoop hardness values for each sample in the series as a function of carbon content are shown below in Figure 34. Assuming that the oxygen content scales inversely with the carbon content, it appears that the hardness increases as

the oxygen content is reduced, reaching a maximum at around 1% added carbon. Above 1% carbon, there is more than enough carbon to fully remove the oxygen and the carbon remaining in the microstructure as small inclusions reduces the hardness from the maximum.

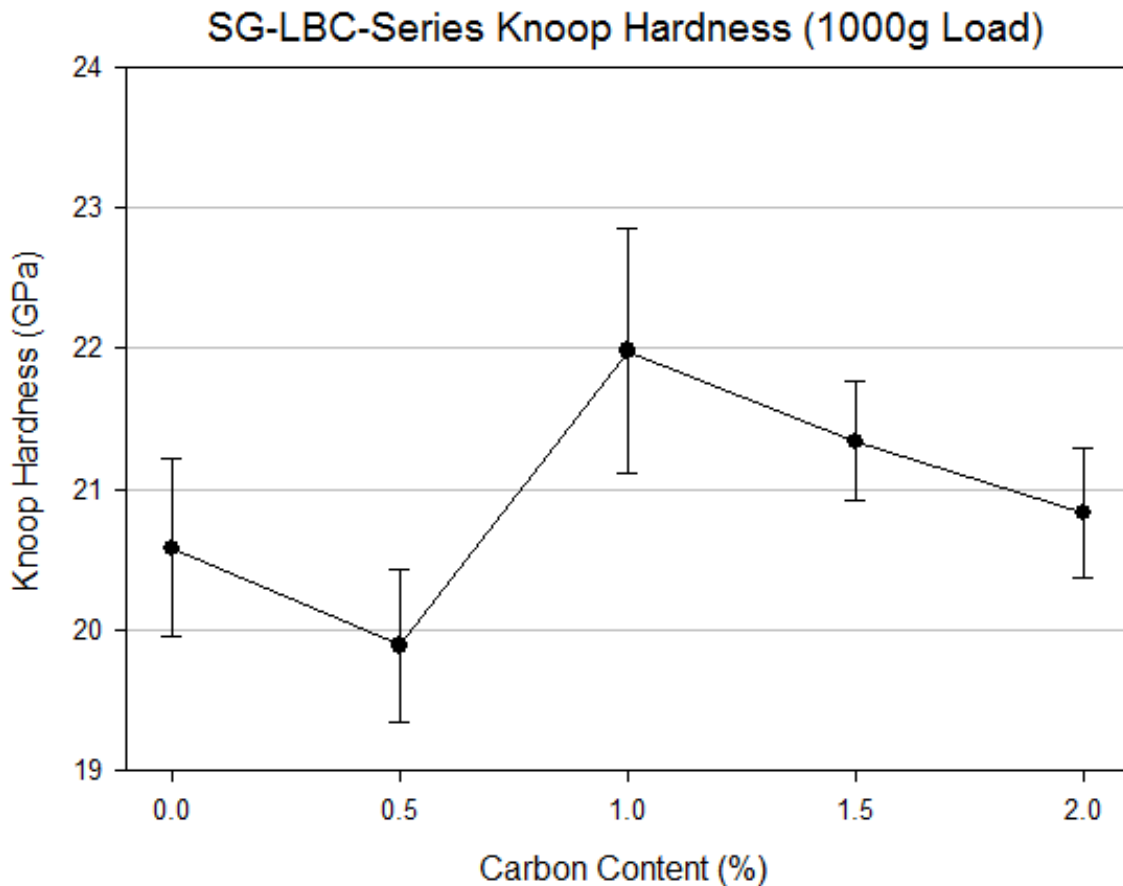


Figure 34. SG-LBC-Series Knoop Hardness at 1000 g load

5.3.1.3. Ultrasound Analysis

Figure 35 below shows the attenuation coefficient spectra for the SG-LBC series samples. The samples all show fairly similar behavior at lower frequencies but differ at frequencies above 40 MHz. The 1.0% and 1.5% samples show low attenuation in this range while the other three samples show increased attenuation. Looking at the microstructures of the different samples, the explanation seems to be in the degree of

porosity. The samples with 0%, 0.5% and 2.0% show increased amounts of porosity which has been shown to cause increased attenuation at these higher frequencies.

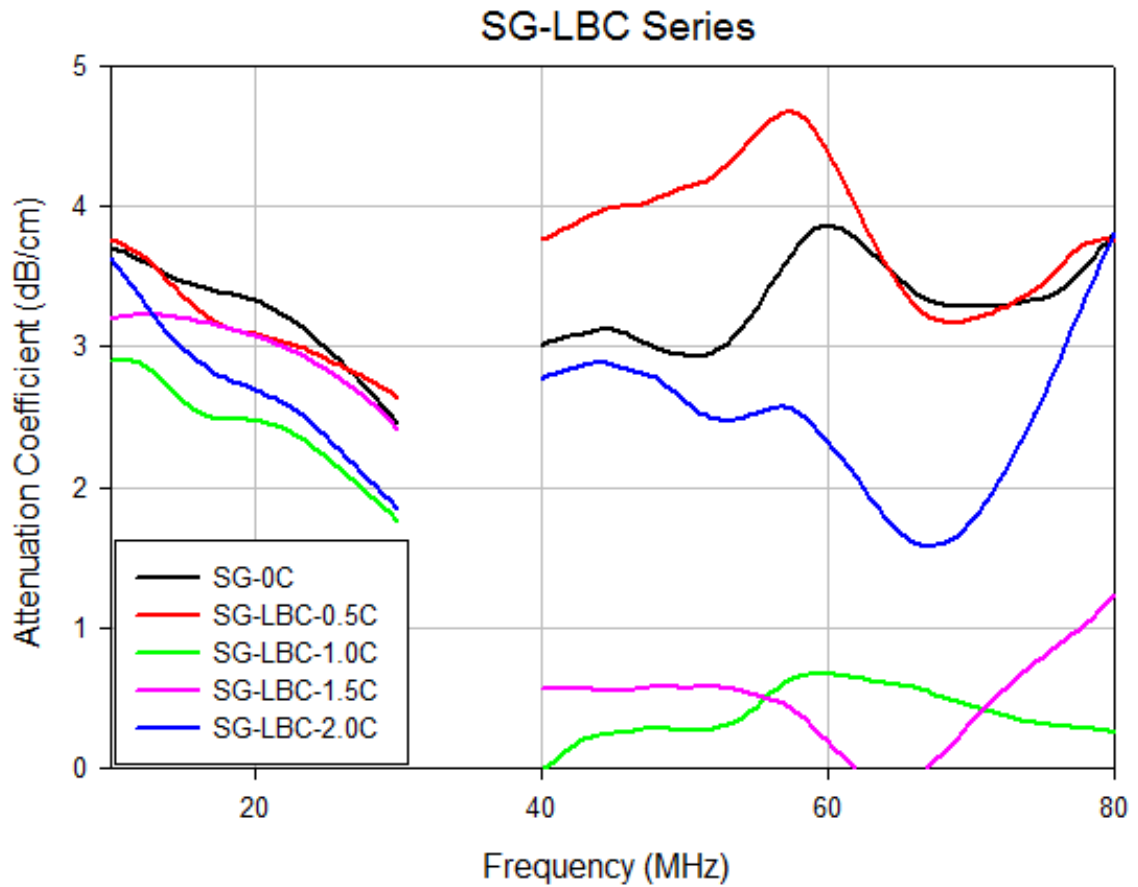


Figure 35. SG-LBC-Series ultrasound attenuation spectra

5.3.2. SG-PRC-Series

5.3.2.1. Microstructure Characterization

Figure 36 shows the microstructures of the SG-PRC series of samples. The samples with lower carbon content show significant amounts of porosity as reflected by the low measured density. The sample with 1.5% carbon is nearly fully dense, with only occasional small pores. The grain size and grain morphology appears to be very similar between the three samples. This is also shown in Table 15 which lists the average grain size and standard deviation for each sample as measured by the linear intercepts method,

measuring at least 100 intercepts per image. All three samples also seem to show similar numbers of second phase inclusions with porosity being the primary difference between them. It might be expected that the samples with greater carbon additions would show more inclusions than the 0.5% carbon sample, but this is not the case. This suggests that most of the carbon is reacting and being removed with the oxygen on the particle surfaces, and that the lower carbon content is not enough to fully remove the oxygen, resulting in inhibited densification. In this case, it would be expected that there would not be any carbon left in the microstructure, as it would all have reacted with the oxygen. The fact that each sample displays these inclusions suggests that perhaps the phenolic resin pooled together in some regions resulting in locally high carbon concentrations which were in excess of the amount needed for oxygen removal and that this resulted in the small carbon inclusions left behind after densification. Compared to the SG-LBC series samples with the same amounts of carbon added, the SG-PRC series all show greater amounts of porosity. This lends further evidence that the resin may not have mixed as well with the SiC powder or it could suggest that some of the phenolic resin carbon may have been lost during processing.

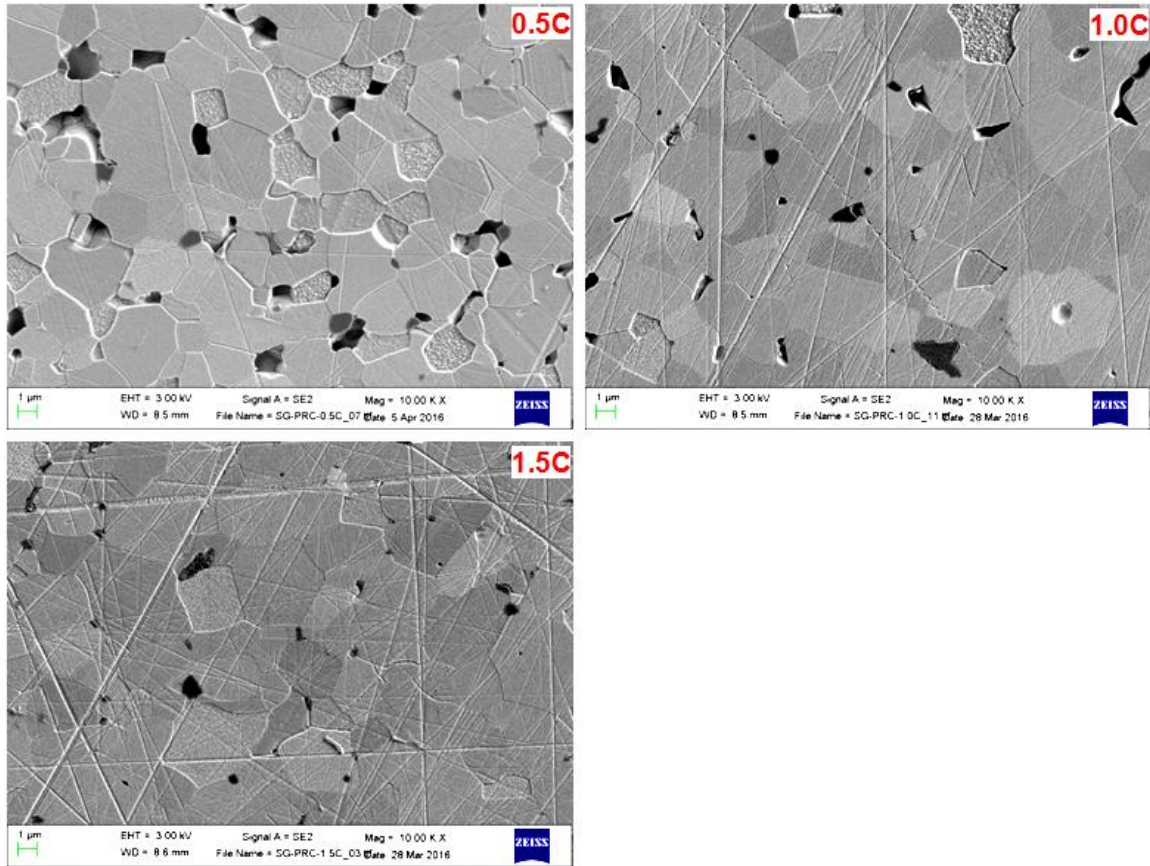


Figure 36. SG-PRC-Series microstructures at 10000x magnification

Table 15. SG-PRC-Series average grain sizes measured by the linear intercepts method

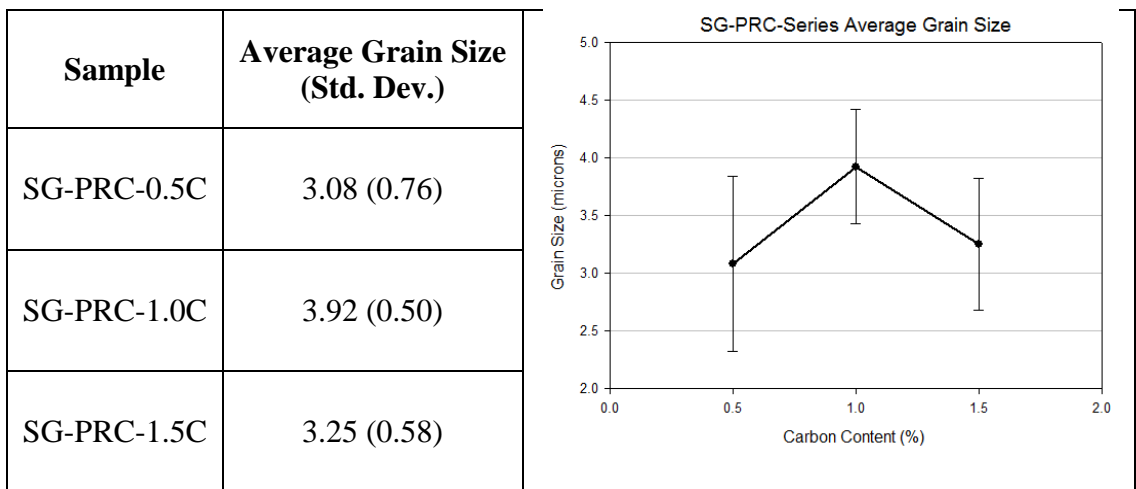


Figure 37 shows EBSD maps of the SG-PRC series of samples. In each of the maps shown, the red color indicates the presence of the 6H SiC polytype and the green color shows the 4H SiC polytype. The black color indicates areas where neither phase found due to the presence of secondary phases, pores, roughness, grain boundaries, or other factors. The investigated areas of each sample are dominated by grains of the 6H polytype with a much smaller fraction of 4H grains. This is also shown in Table 16 which presents the phase fractions of each polytype present in the mapped areas. Due to the presence of the black areas mentioned before, the total areas of 6H and 4H do not add up to a full 100%. For each of the samples, the ratio of 4H/6H SiC is quite low, between 0.141 – 0.221, which is only slightly higher than the starting powder ratio of 0.109. In these samples, it does not appear that differences in the oxygen content, which should decrease as the amount of carbon added increases, has much of an effect on the SiC polytype ratio in this case.

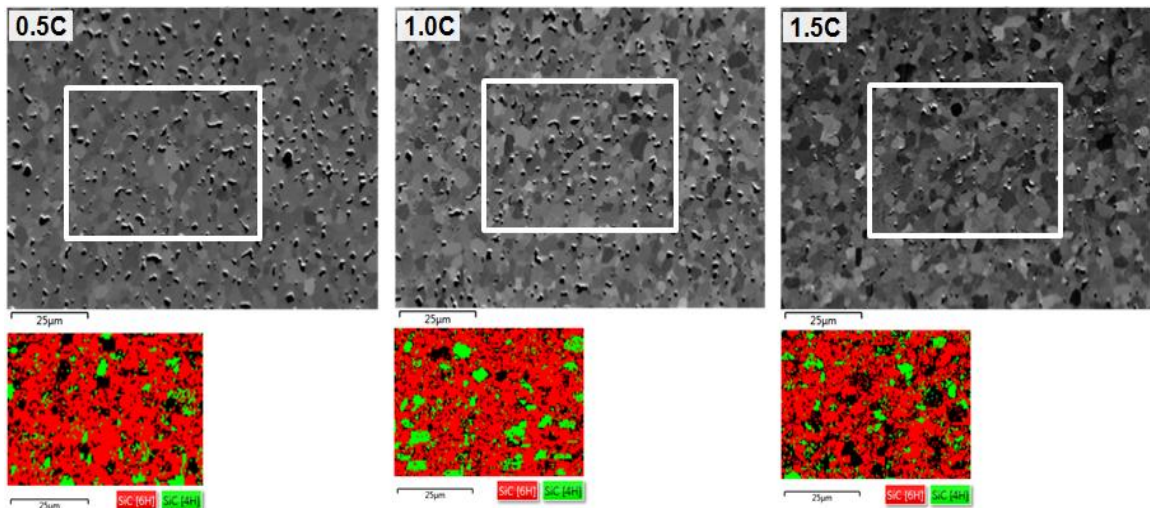


Figure 37. SG-PRC-Series EBSD Maps

Table 16. SG-PRC-Series phase fractions

Sample	Phase Fraction 4H (%)	Phase Fraction 6H (%)	4H/6H ratio
SG-PRC-0.5C	10	68	0.15
SG-PRC-1.0C	15	66	0.23
SG-PRC-1.5C	10	57	0.18

5.3.2.2. Mechanical Properties

The densities of the SG-PRC-Series samples were determined using Archimedes' method and the elastic properties were measured using the nondestructive ultrasonic techniques and are shown below in Table 17. The longitudinal and shear sound speeds were measured directly and the Poisson's Ratio and moduli were calculated from these values using the equations described in Section 4.5.2. The elastic properties were plotted against the carbon content as shown below in Figure 38. Assuming that the oxygen content scales inversely with the carbon content, it is clear that all of the measured elastic properties increase as the oxygen content is reduced. This is primarily due to the reduced porosity of the higher carbon samples, which in turn results in higher elastic property values as given by the equation

$$\frac{E}{E_0} = 1 - bP \quad \text{Equation 10}$$

where E is the Young's modulus, E_0 is the Young's modulus without any porosity, P is the volume fraction of porosity, and b is an empirically derived constant that is typically around 4 for ceramics.[68]

Table 17. SG-PRC-Series elastic properties

Sample	c_L (m/s)	c_S (m/s)	Poisson	Density (g/cm ³)	E (GPa)	G (GPa)	K (GPa)
SG-PRC-0.5C	11910	7560	0.16	3.05	407	175	199
SG-PRC-1.0C	12000	7610	0.16	3.08	415	178	206
SG-PRC-1.5C	12160	7740	0.16	3.18	441	190	216

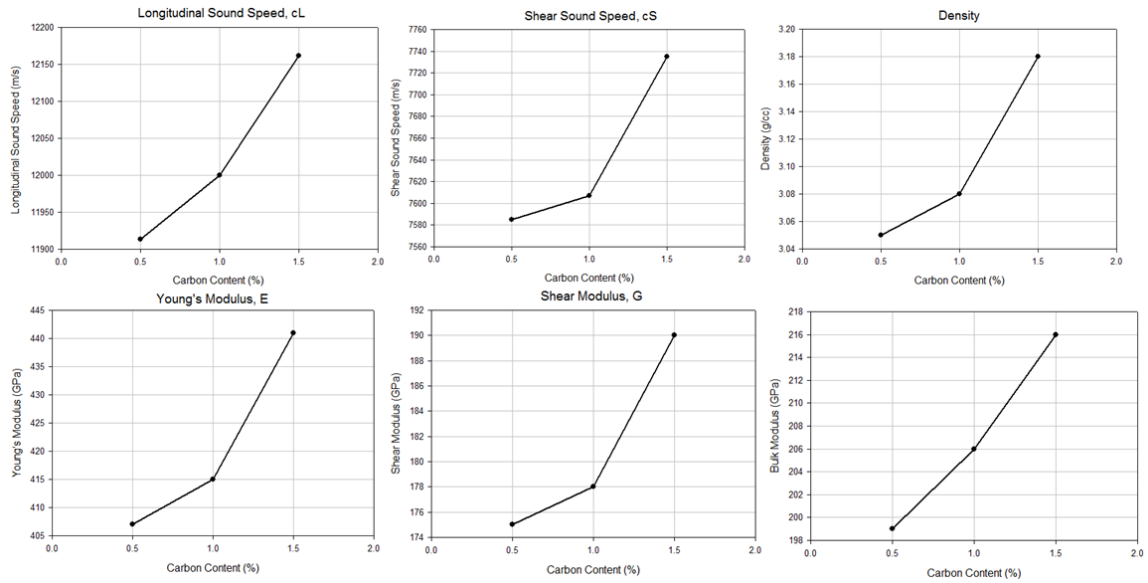


Figure 38. SG-PRC-Series elastic properties vs. carbon content

Knoop microhardness testing was performed on each sample in the SG-PRC series with 10 indents at each of five different loads (100 g, 300 g, 500 g, 1000 g, 2000 g). Load-hardness curves for each sample are shown below in Figure 39, and again show the typical indentation size effect. As with the elastic properties, the hardness increases with increasing amounts of added carbon and therefore lower oxygen content. Again, this is due to the increased density of the higher carbon sample which is a result of the more complete removal of the oxygen on the powder surfaces by the added carbon.

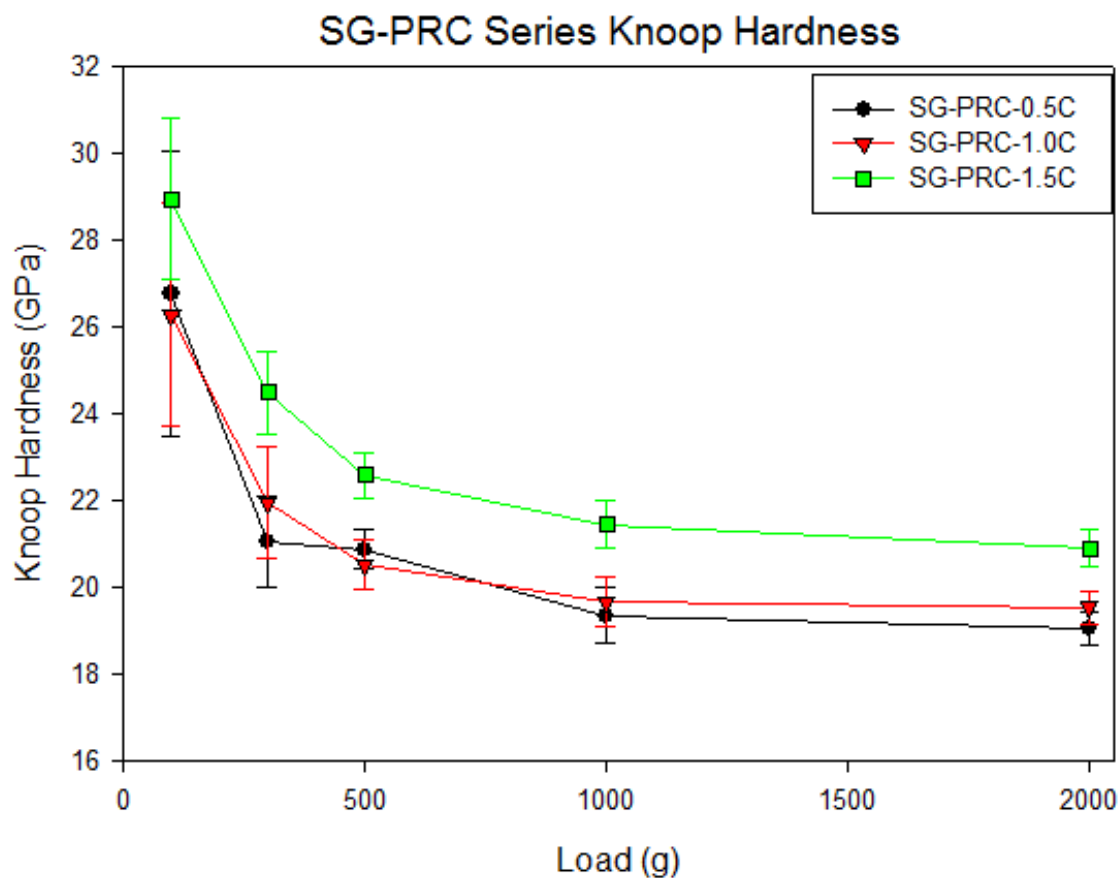


Figure 39. SG-PRC-Series Knoop Hardness curves

The 1000 g load Knoop hardness values for each sample in the series as a function of carbon content are shown below in Figure 40. Assuming that the oxygen content scales inversely with the carbon content, it appears that the hardness increases as the oxygen content is reduced, reaching a maximum at 1.5% added carbon, which would result in the lowest oxygen content. This behavior differs from that of the SG-LBC series where the hardness peaked at 1% added carbon before dropping as more carbon was added. This would suggest that some of the phenolic resin may have been lost during processing and that the actual amount of carbon in the samples during sintering was lower than the amount initially added, or that the phenolic resin did not mix well with the

SiC powder and was not distributed evenly in such a way that it could effectively remove all the oxygen.

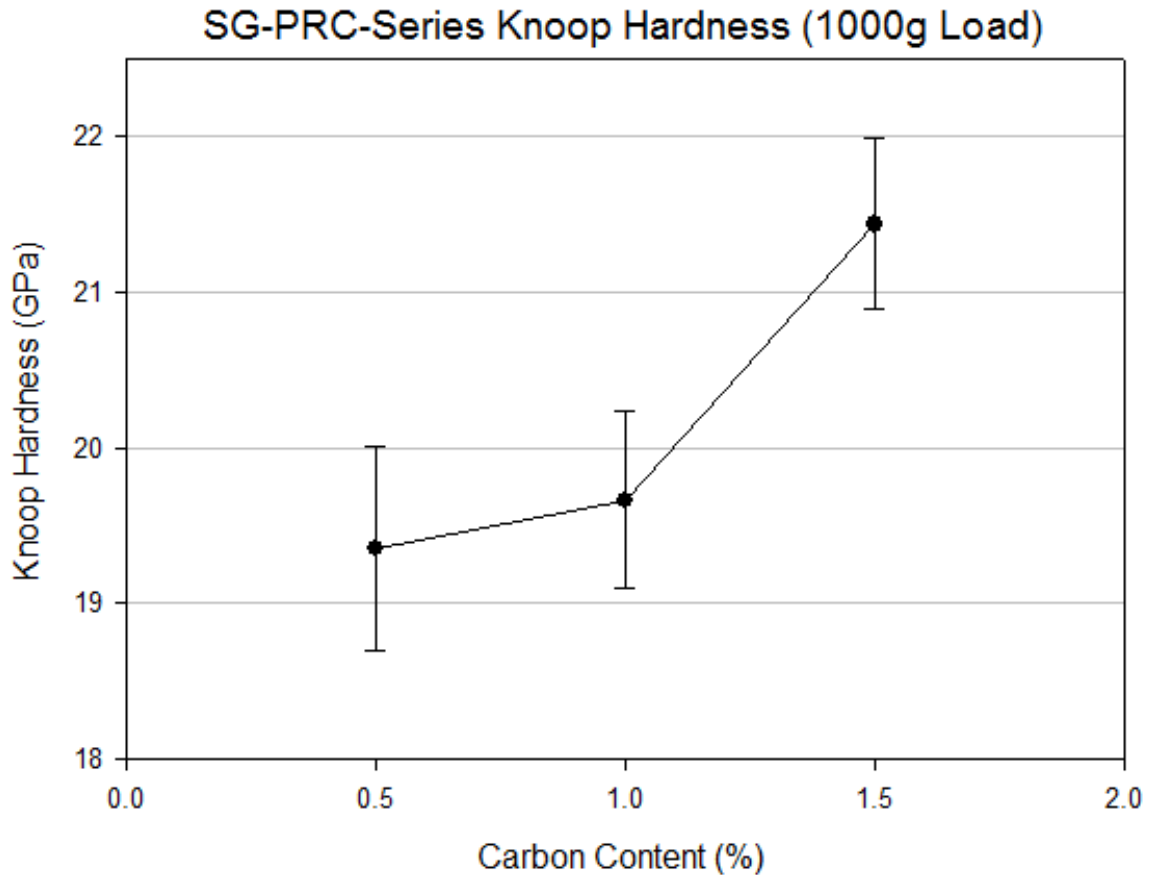


Figure 40. SG-PRC-Series Knoop Hardness at 1000 g load

5.3.2.3. Ultrasound Analysis

Figure 41 below shows the attenuation coefficient spectra for the SG-PRC series samples. The samples all show fairly similar behavior at lower frequencies below 30 MHz but differ significantly at frequencies above 40 MHz. Looking at the microstructures of the different samples, there seems to be some explanation for the differences in the attenuation spectra between samples. The SG-PRC samples all have similar grain size and shape, but the samples with 0.5% and 1.0% show significant amounts of porosity. This suggests that porosity is the dominant attenuation mechanism

at the measured frequencies rather than scattering from the silicon carbide grains. If scattering was the dominant mechanism, the attenuation spectra would look much more similar as the grain size distributions between these samples are very similar.

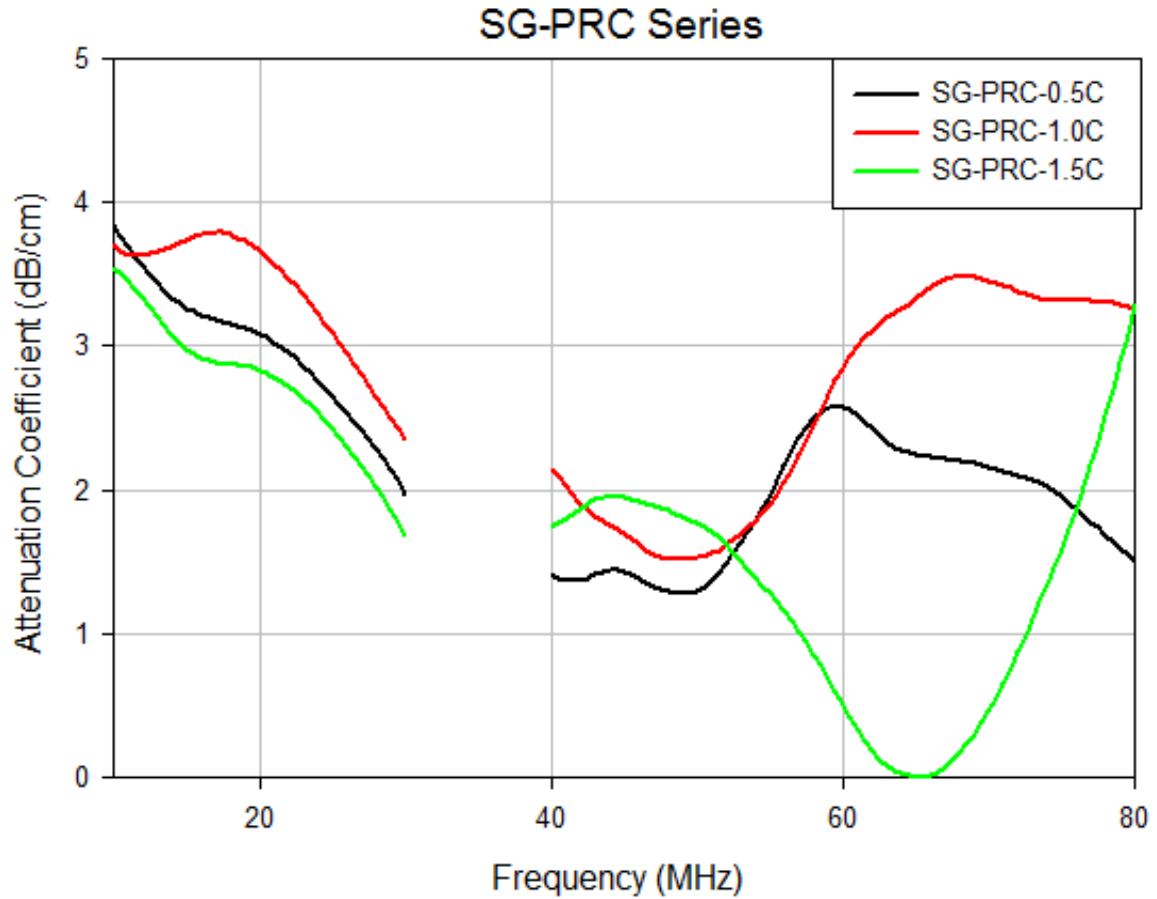


Figure 41. SG-PRC-Series ultrasound attenuation spectra

5.3.3. SG-AW-Series

5.3.3.1. Microstructure Characterization

Figure 42 shows the microstructures of the SG-AW series of samples. At the lowest oxygen level, the sample is fully dense and displays small, fairly equiaxed grains. There are a number of small carbonaceous inclusions located at the grain boundaries and triple points between grains. As the oxygen content increases to an intermediate level, the microstructure changes dramatically. The grains are now almost entirely large with high

aspect ratios. There are still many small inclusions present, but many of them have been completely engulfed by the large grains, with fewer of them appearing between grains. At the highest oxygen content, there is again a drastic change in the microstructure. The grains are again relatively small and equiaxed, but there is a great deal of porosity and very few remaining carbon inclusions, suggesting that almost all of the carbon reacted with the oxygen on the surface of the powder during sintering. This behavior is reflected in Table 18 below which lists the average grain size and standard deviation for each sample as measured by the linear intercepts method. At least 100 intercepts were measured for each image. It is clear that the oxygen content has a major effect on the grain size and shape in these samples.

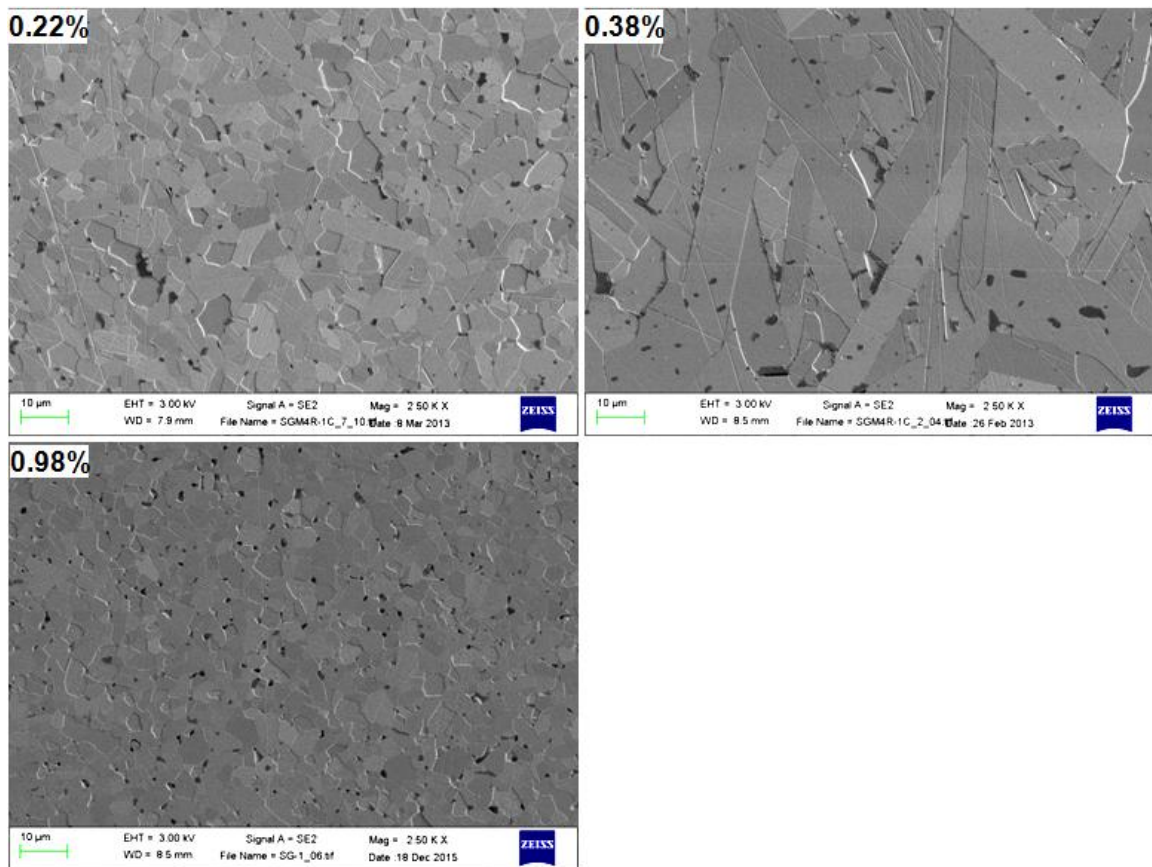


Figure 42. SG-AW-Series microstructures at 2500x magnification

Table 18. SG-AW-Series average grain sizes measured by the linear intercepts method

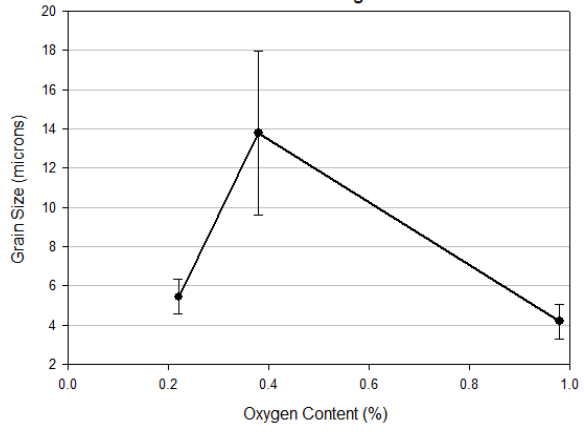
Sample	Average Grain Size (Std. Dev.)	
SG-AW-0.22%	5.43 (0.89)	
SG-AW-0.38%	13.80 (4.19)	
SG-AW-0.98%	4.18 (0.88)	

Figure 43 shows EBSD maps of the SG-AW series of samples. In each of the maps shown, the red color indicates the presence of the 6H SiC polytype and the green color shows the 4H SiC polytype. The black color indicates areas where neither phase found due to the presence of secondary phases, pores, roughness, grain boundaries, or other factors. Table 19 shows the phase fractions of each polytype present in the mapped areas as well as the polytype ratio. Due to the presence of the black areas mentioned before, the total areas of 6H and 4H do not add up to a full 100%. For the lowest oxygen content sample the ratio of 4H/6H SiC is quite low at 0.241, which is in line with the other samples that use this powder. For the intermediate oxygen content sample, there is a shift from 6H to 4H grains dominating the microstructure. This is shown by the high 4H/6H ratio of 1.926. At higher oxygen contents, the sample returns to a lower 4H/6H ratio of 0.262.

In this case, it appears that the oxygen content has a large effect on the SiC polytype ratio. At low concentrations, the oxygen appears to be fully removed by the added carbon and the sample retains a lower 4H/6H ratio. At intermediate levels, there

may not be enough carbon to fully remove the oxygen resulting in increased conversion of 6H to 4H and major grain growth and elongation. At higher oxygen concentrations all of the carbon is exhausted and densification and grain growth are inhibited but the 6H grains are not transformed to 4H.

In the previous sections, the SG-LBC and SG-PRC samples were shown to have similar 4H/6H ratios regardless of the oxygen content as dictated by the amount of carbon available to remove it during sintering. In the case of the SG-AW samples, the 4H/6H ratio was very different, even with the same amount of carbon additive. This suggests that the transformation from 6H to 4H is dictated by the initial oxygen content of the powder prior to any reaction with carbon additives. In work on hot pressing SiC without additives, Sajgalik found that annealing SiC powders at relatively low temperatures (150°C) led to the formation of an oxycarbide glass phase on the particle surfaces and that this phase could form a transient melt during sintering, leading to enhanced densification and SiC polytype transformation.[69] This annealing process is similar to the aging done on the 0.38% sample and the formation of an oxycarbide liquid phase during sintering may explain the increased polytype transformation and grain growth in this sample compared to the others. The highest oxygen content sample does not show this behavior though, which may indicate that the higher temperature oxidation results in a different oxide phase on the powder surface which does not melt and enhance densification during sintering.

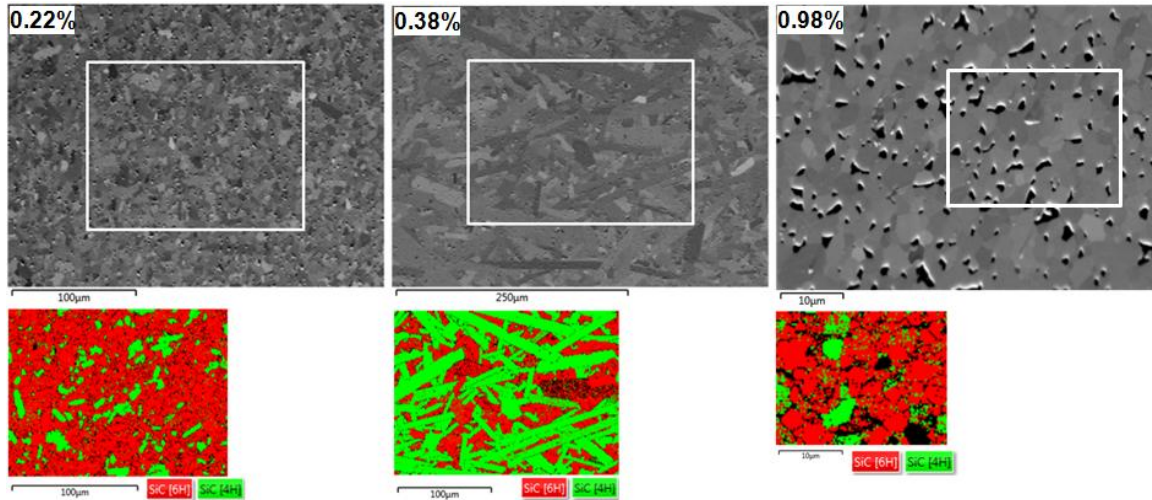


Figure 43. SG-AW-Series EBSD Maps

Table 19. SG-AW-Series phase fractions

Sample	Phase Fraction 4H (%)	Phase Fraction 6H (%)	4H/6H ratio
SG-AW-0.22%	17	71	0.24
SG-AW-0.38%	61	31	1.97
SG-AW-0.98%	16	63	0.25

5.3.3.2. Mechanical Properties

The densities of the SG-AW-Series samples were determined using Archimedes' method and the elastic properties were measured using the nondestructive ultrasonic techniques and are shown below in Table 20. The longitudinal and shear sound speeds were measured directly and the Poisson's Ratio and moduli were calculated from these values using the equations described in Section 4.5.2. The elastic properties were plotted against the carbon content as shown below in Figure 44. Looking at the densities and modulus, it is clear that the higher oxygen content is detrimental to the elastic properties of these samples. While the low and intermediate oxygen samples are fairly close in

density, as the oxygen content is increased to a higher level, the density drops slightly as do the other elastic properties.

Table 20. SG-AW-Series elastic properties

Sample	c_L (m/s)	c_S (m/s)	Poisson	Density (g/cm^3)	E (GPa)	G (GPa)	K (GPa)
SG-AW-0.22%	12100	7720	0.16	3.19	440	190	214
SG-AW-0.38%	12140	7680	0.17	3.18	437	188	218
SG-AW-0.98%	12180	7750	0.16	3.12	434	187	213

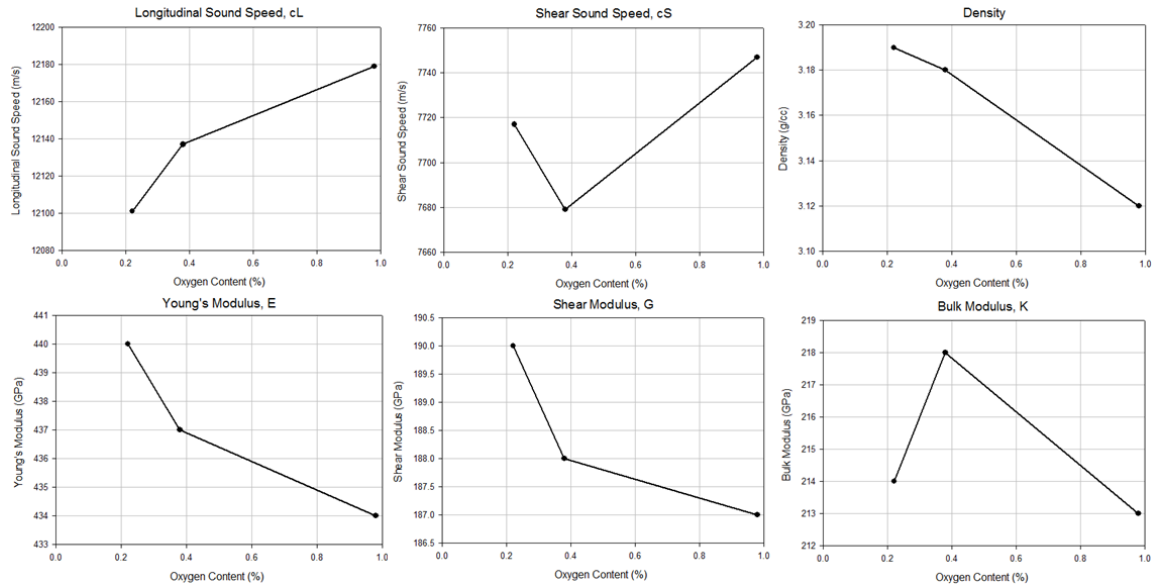


Figure 44. SG-AW-Series elastic properties vs. oxygen content

Knoop microhardness testing was performed on each sample in the SG-AW series with 10 indents at each of five different loads (100 g, 300 g, 500 g, 1000 g, 2000 g). Load-hardness curves for each sample are shown below in Figure 45. The hardness of all three samples is fairly similar over the entire load range and shows the typical indentation size effect. At higher loads, the hardness follows the same trend as the density and modulus, with the hardness increasing as the oxygen content decreases. However, at

lower loads, the intermediate oxygen sample shows a lower hardness. This could be due to grain size effects [70] as the average grain size of the intermediate oxygen sample is much larger than the others.

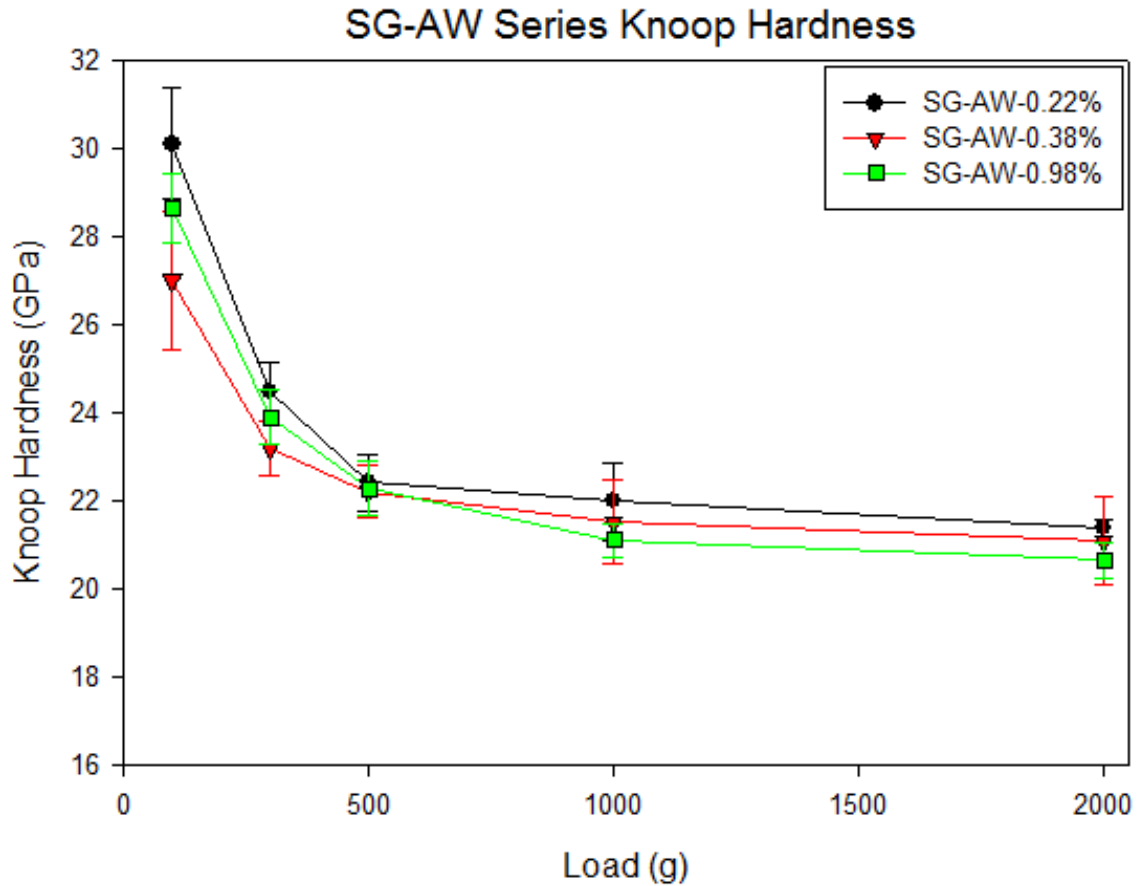


Figure 45. SG-AW-Series Knoop Hardness curves

The 1000 g load Knoop hardness values for each sample in the series as a function of oxygen content are shown below in Figure 46. At this load, the hardness is very similar for each sample although it does appear to decrease slightly with increasing oxygen content.

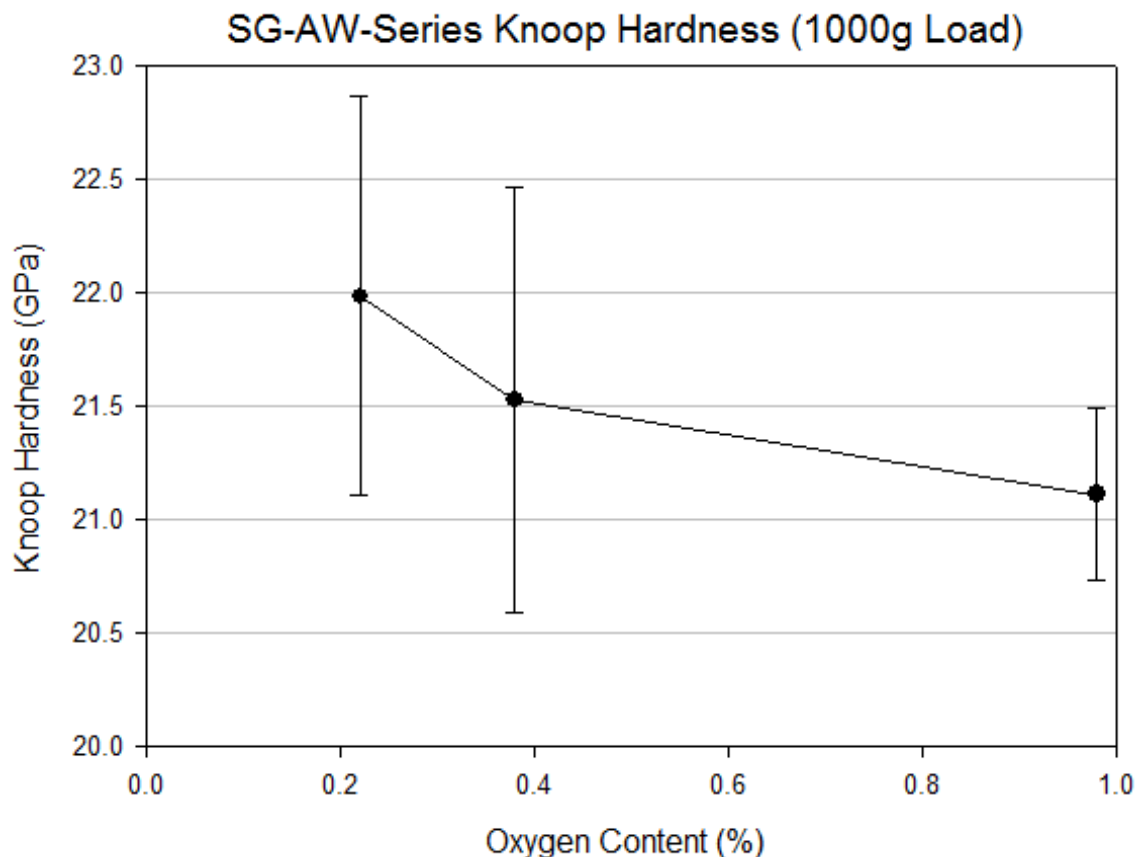


Figure 46. SG-AW-Series Knoop Hardness at 1000 g load

Pieces of each SG-AW-Series sample were broken and the fracture surfaces were examined in the FESEM. Micrographs of the fracture surfaces are shown below in Figure 47. Each of the three samples appears to show mixed mode fracture, with some intergranular fracture taking place around the smaller grains, but also a significant amount of transgranular fracture through the grains. This is most obvious in the 0.38% sample where the fracture surface goes straight through some of the larger grains leaving large flat areas on the surface.

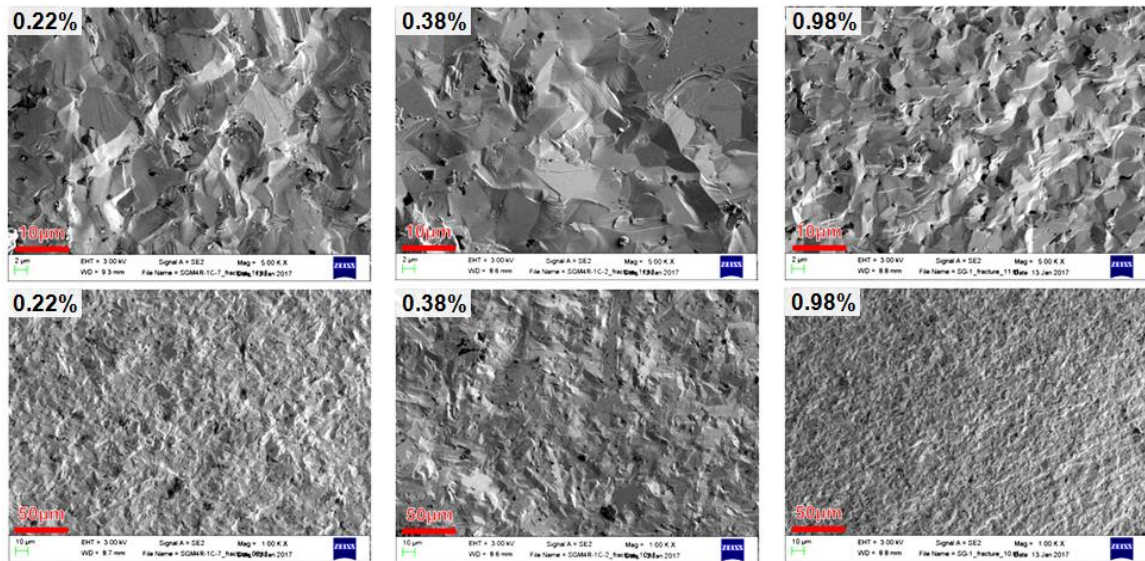


Figure 47. SG-AW-Series fracture surface images at 5000x magnification (top row) and 1000x magnification (bottom row)

5.3.3.3. Ultrasound Analysis

Figure 48 below shows the attenuation coefficient spectra for the SG-AW series samples. Like the previous series samples, the low frequency attenuation spectra are very similar in shape between samples. At high frequencies, there is a notable increase in attenuation as the oxygen content on the powder used to make the samples increases. Between the 0.22% oxygen and 0.38% oxygen samples, this difference should be caused by the increase in grain size and change in grain morphology as these are the only features that are different between the two samples. At 0.98% oxygen, the large increase in the attenuation coefficient is caused by the increase in porosity as other microstructural features such as grain size and shape are similar to that of the lowest oxygen content sample.

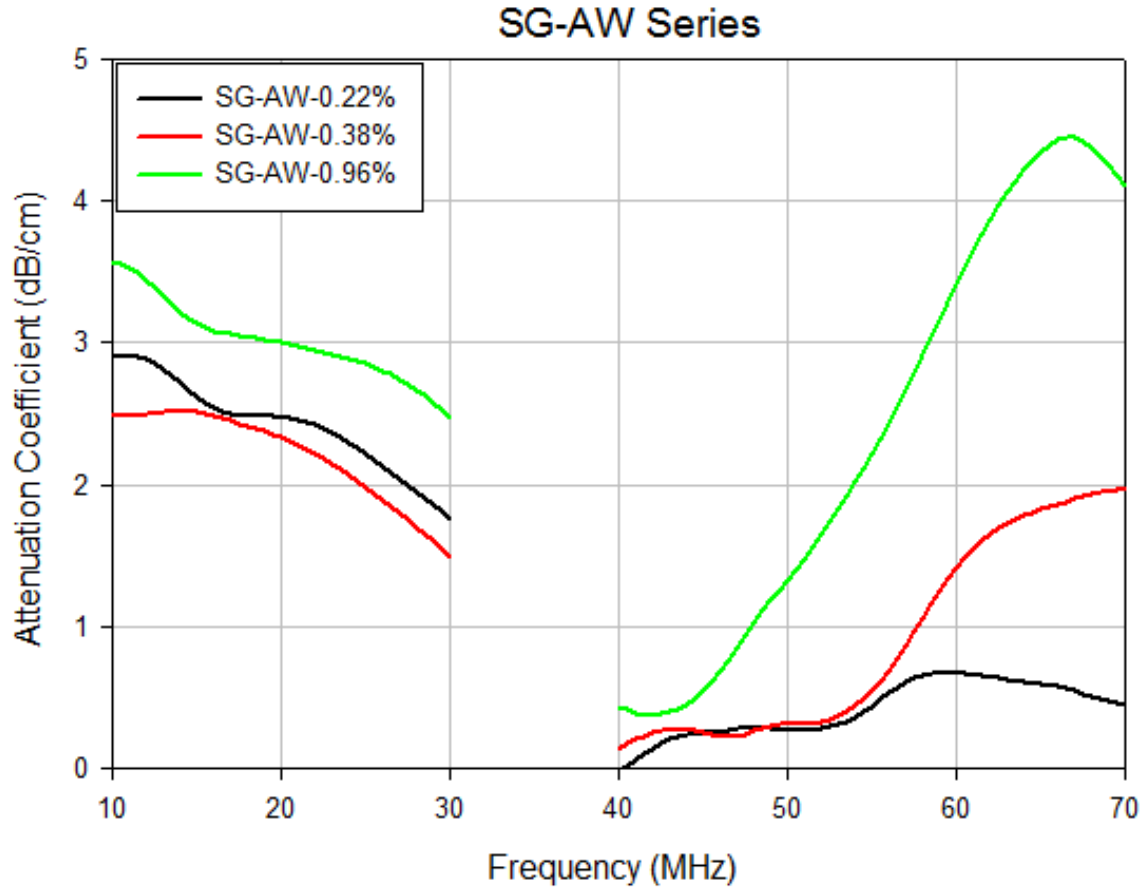


Figure 48. SG-AW-Series ultrasound attenuation spectra

5.3.4. HC-LBC-Series

5.3.4.1. Microstructure Characterization

Figure 49 shows the microstructures of the HC-LBC series of samples. The sample with the lowest carbon content was almost fully dense, while the samples with additional carbon added showed some residual porosity. The 1.5% carbon sample showed almost no residual carbon remaining in the microstructure after sintering while the 3.0% displayed a number of small carbonaceous inclusions. The 4.5% sample shows a significant concentration of carbon inclusions but a lower degree of porosity compared to the 3.0% sample.

The average grain size is similar between the samples in this series, but the grain morphology varies significantly with the change in carbon content. The 1.5% sample shows some elongation of grains which results in a wider range of grain sizes while the higher carbon samples tend to be more equiaxed with a much narrower distribution of grain sizes. This behavior is reflected in Table 21 which lists the average grain size and standard deviation for each sample as measured by the linear intercepts method. Since the 1.5% sample shows almost no residual carbon, it could be that all of the carbon was consumed during the pre-sintering process to remove oxygen, suggesting that it may not have been enough to fully remove the oxygen from the powder. The remaining oxygen may be causing the changes in the microstructure compared to the samples that did have enough carbon to fully remove the oxygen from the surfaces of the powder. Additionally, the excess carbon present in the higher carbon samples may play a role in preventing the elongated grain growth in those samples.

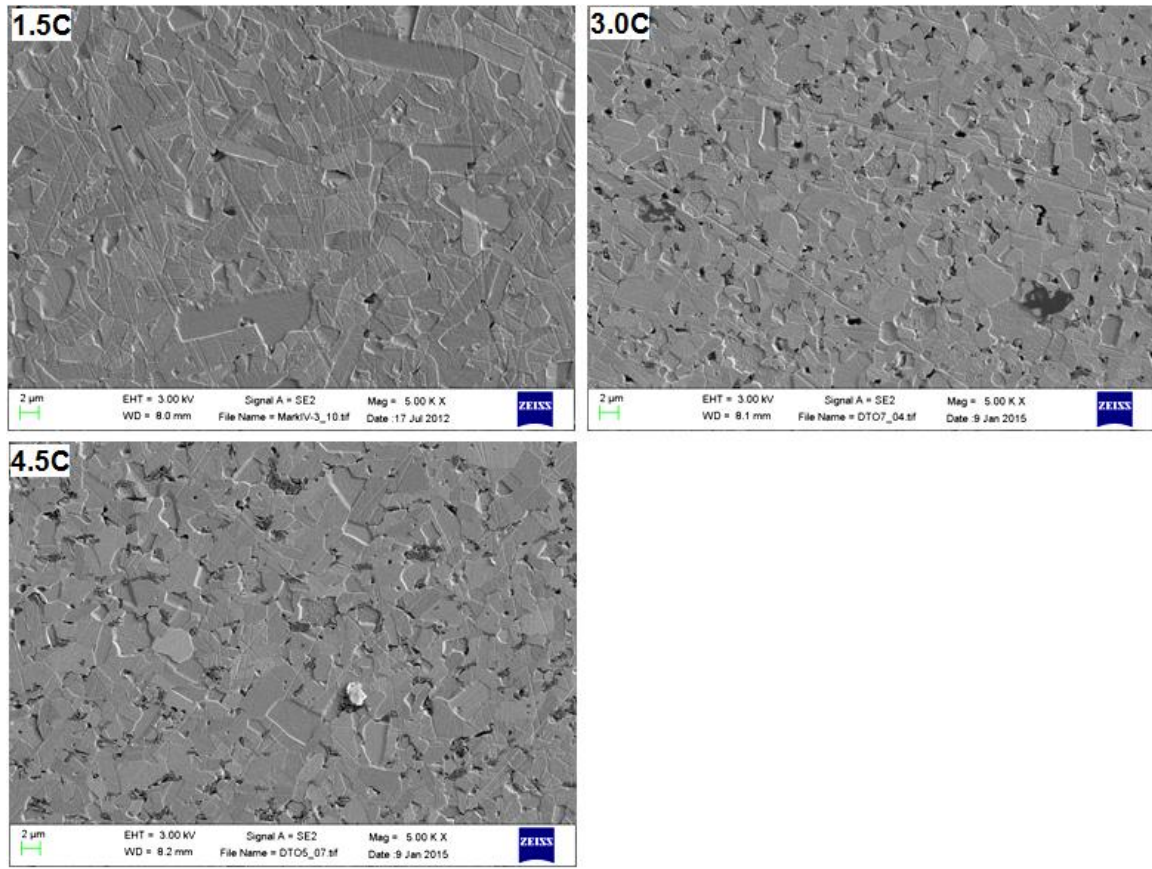


Figure 49. HC-LBC-Series microstructures at 5000x magnification

Table 21. HC-LBC-Series average grain sizes measured by the linear intercepts method

Sample	Average Grain Size (Std. Dev.)	<p>HC-LBC-Series Average Grain Size</p>
HC-LBC-1.5C	2.28 (1.91)	
HC-LBC-3.0C	2.41 (0.33)	
HC-LBC-4.5C	2.55 (0.72)	

Figure 50 shows EBSD maps of the HC-LBC series of samples. In each of the maps shown, the red color indicates the presence of the 6H SiC polytype and the green color shows the 4H SiC polytype. The black color indicates areas where neither phase is found due to the presence of secondary phases, pores, roughness, grain boundaries, or other factors. The investigated areas of each sample are dominated by grains of the 6H polytype while a smaller fraction of the grains are 4H. In the 1.5% C sample, the 4H polytype is seen more often in the elongated grains. While there are more 6H grains in this sample, the large size of the 4H grains results in a higher 4H/6H ratio than the other samples. This is also reflected in Table 22 which shows the phase fractions of each polytype present in the mapped areas. Due to the presence of the black areas mentioned before, the total areas of 6H and 4H do not add up to a full 100%. For the higher carbon samples, the ratio of 4H/6H SiC is quite low, between 0.23 – 0.24, which is only slightly higher than the starting powder ratio of 0.152. On the other hand, the low carbon sample shows an elevated 4H/6H ratio of 0.426. In this case, it does appear that the oxygen content, which would decrease as the amount of carbon added increases, has an effect on the 6H to 4H ratio. As the amount of oxygen remaining increases, the amount of 4H increases relative to 6H.

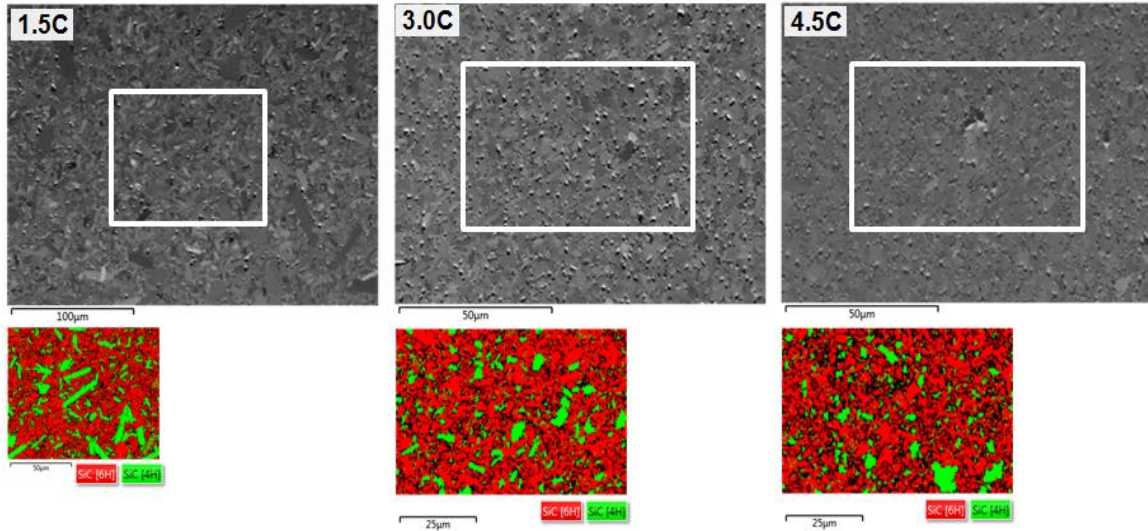


Figure 50. HC-LBC-Series EBSD Maps

Table 22. HC-LBC-Series phase fractions

Sample	Phase Fraction 4H (%)	Phase Fraction 6H (%)	4H/6H ratio
HC-LBC-1.5C	23	53	0.43
HC-LBC-3.0C	14	60	0.23
HC-LBC-4.5C	13	54	0.24

5.3.4.2. Mechanical Properties

The densities of the HC-LBC-Series samples were determined using Archimedes' method and the elastic properties were measured using the nondestructive ultrasonic techniques and are shown below in Table 23. The longitudinal and shear sound speeds were measured directly and the Poisson's Ratio and moduli were calculated from these values using the equations described in Section 4.5.2. The elastic properties were plotted against the carbon content as shown below in Figure 51. There is a clear negative trend

where the density and elastic properties decrease dramatically with increasing amounts of carbon. This suggests that the effect of the residual carbon in the microstructure of these samples dominates any effect of the oxygen content in this case.

Table 23. HC-LBC-Series elastic properties

Sample	c_L (m/s)	c_S (m/s)	Poisson	Density (g/cm^3)	E (GPa)	G (GPa)	K (GPa)
HC-LBC-1.5C	12270	7820	0.16	3.20	453	195	221
HC-LBC-3.0C	11560	7450	0.15	3.16	401	175	188
HC-LBC-4.5C	11030	7130	0.14	3.13	363	159	169

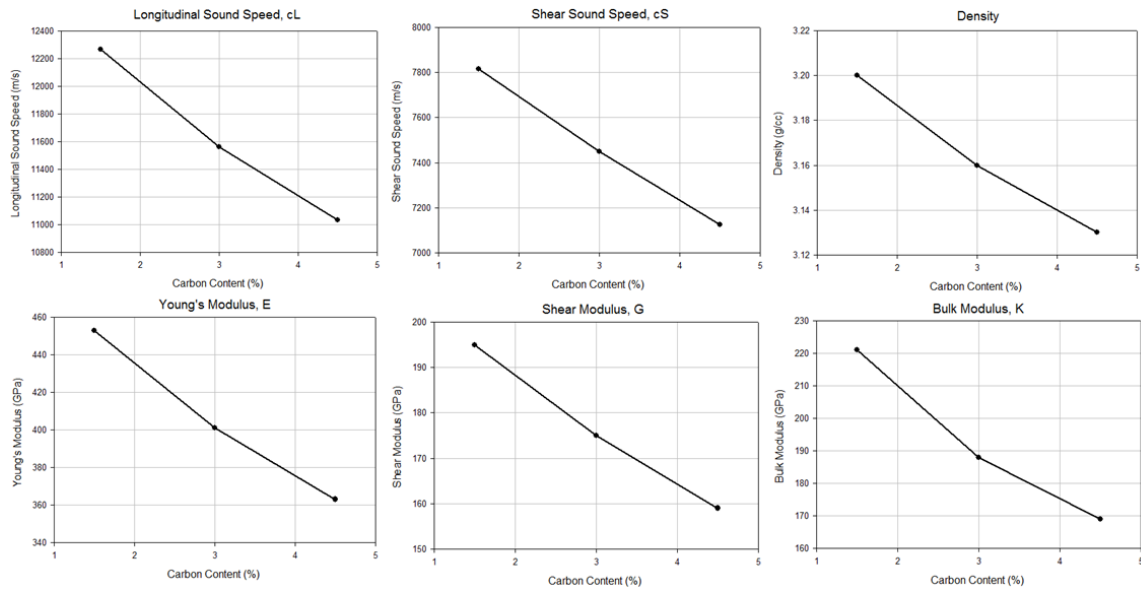


Figure 51. HC-LBC-Series elastic properties vs. carbon content

Knoop microhardness testing was performed on each sample in the HC-LBC series with 10 indents at each of five different loads (100 g, 300 g, 500 g, 1000 g, 2000 g). Load-hardness curves for each sample are shown below in Figure 52, again showing a clear indentation size effect. As with the elastic properties, the hardness decreases with increasing carbon content across the entire load range. Again, this is likely

due to the increased presence of carbonaceous inclusions in the higher carbon content samples, as these inclusions are much softer than the SiC primary phase. The 1000 g load Knoop hardness values for each sample in the series as a function of carbon content are shown below in Figure 53. At this load the same trend is clearly visible

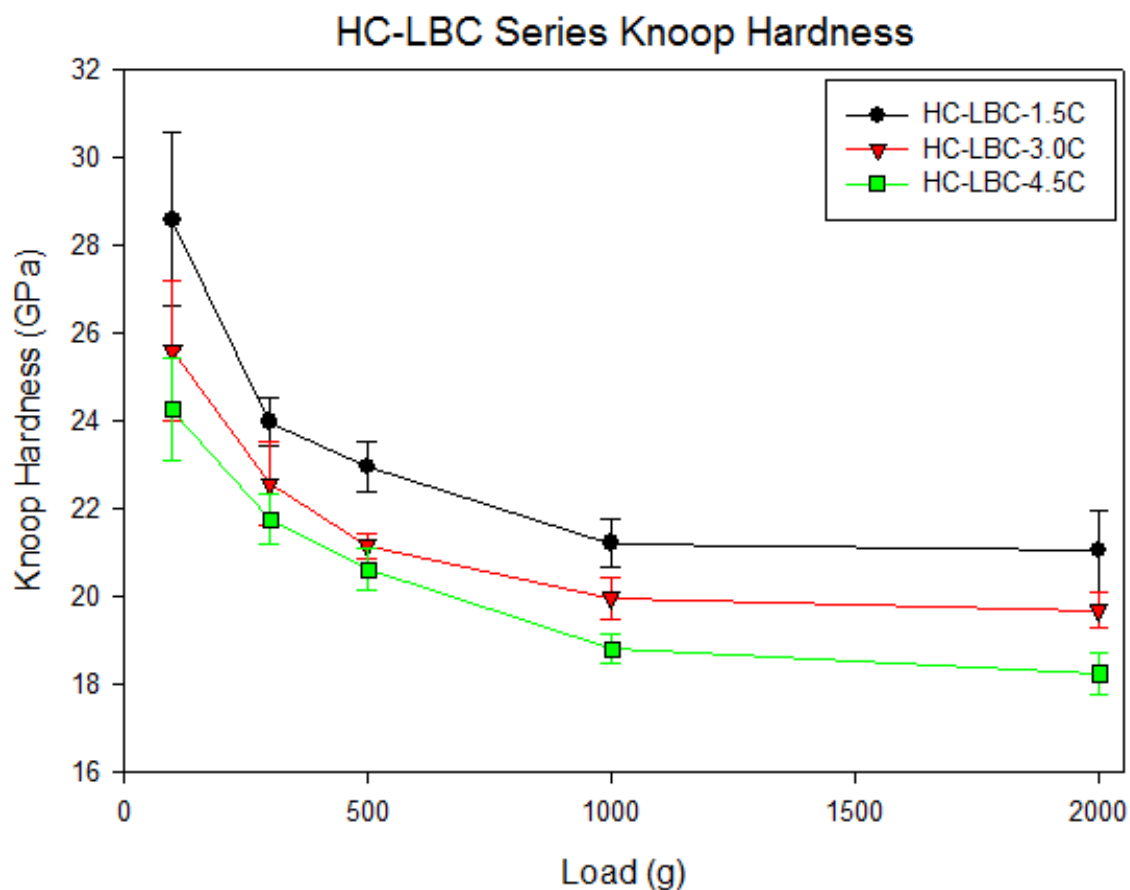


Figure 52. HC-LBC-Series Knoop Hardness curves

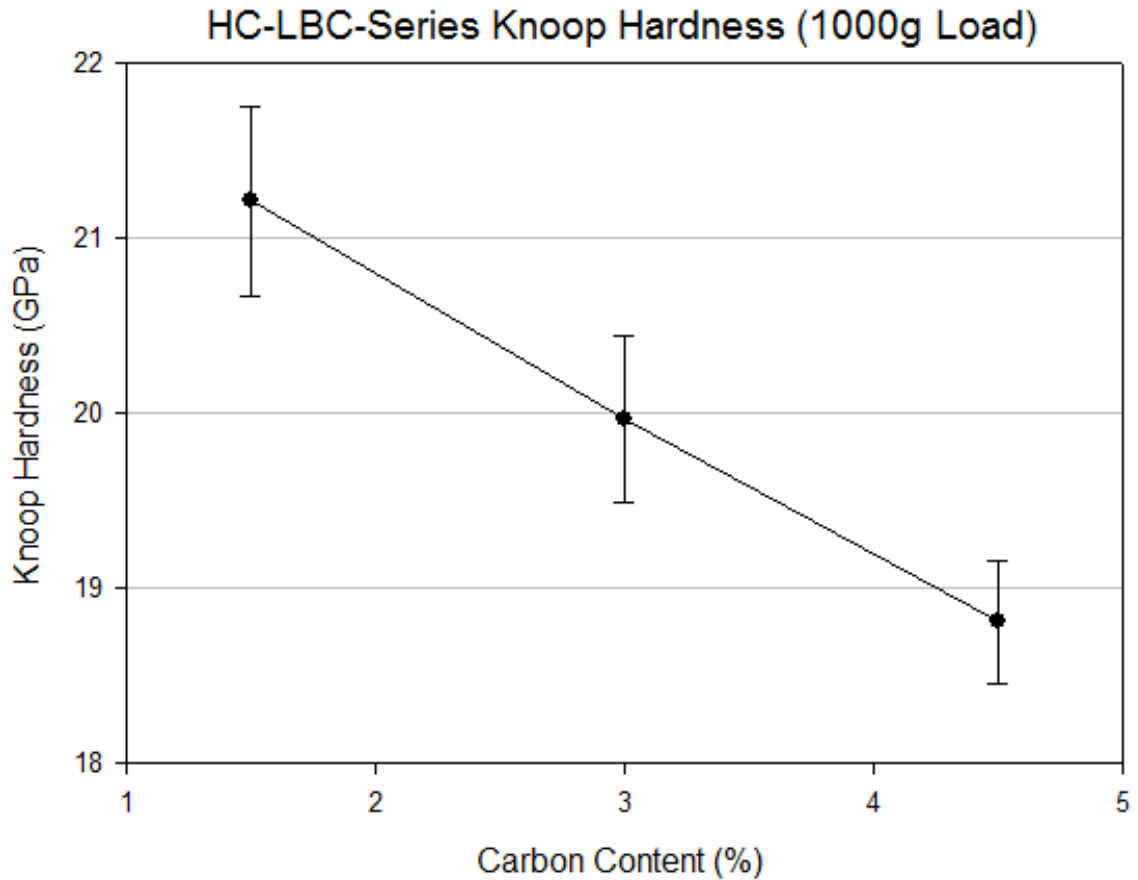


Figure 53. HC-LBC-Series Knoop Hardness at 1000 g load

5.3.4.3. Ultrasound Analysis

Figure 54 below shows the attenuation coefficient spectra for the HC-LBC series samples. The samples show fairly similar behavior at lower frequencies but differ at intermediate frequencies between 40 – 60 MHz. At frequencies above 60 MHz, the attenuation spectra begin to converge again. The 3.0% and 4.5% samples show similar attenuation spectra across the entire frequency range which coincides with the generally similar appearance of the sample microstructures. The 1.5% sample shows different behavior, which is caused by the difference in grain size and shape.

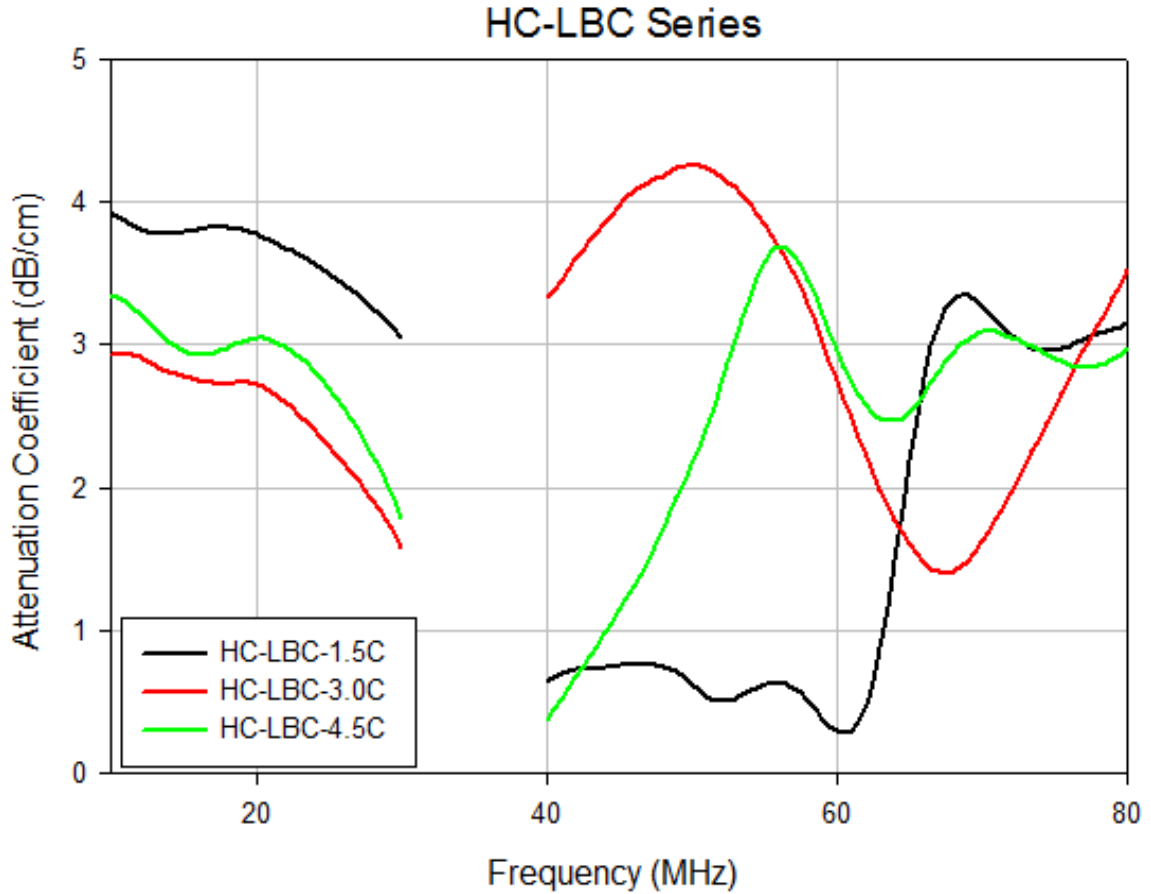


Figure 54. HC-LBC-Series ultrasound attenuation spectra

5.3.5. HC-PRC-Series

5.3.5.1. Microstructure Characterization

Figure 55 shows the microstructures of the HC-PRC series of samples. The sample with the lowest carbon content shows very small grain size and appears to be overetched, much like the sample shown in section 5.3.6.1. with artificially increased oxygen content in which the grain growth was suppressed by the formation of a second phase. This was a surprising result as no treatment was done on the powder used for this sample. As the carbon content is increased to 3.0%, the grain size increases and some grains begin to show significant elongation, resulting in a wider grain size distribution. There is also no evidence of the formation of a second phase. As the carbon content is

further increased to 4.5%, the grain size stays about the same, and while there is still some elongation of the grains, it is not as severe as in the 3.0% sample. This behavior is reflected in Table 24 which lists the average grain size and standard deviation for each sample as measured by the linear intercepts method.

This trend follows that shown in Section 5.3.6.1. where a higher oxygen content (corresponding to low carbon content) results in densification with secondary phase formation and retention of fine, equiaxed grains, intermediate oxygen content (corresponding to intermediate carbon content) results in anisotropic grain growth, while low oxygen content (corresponding to high carbon content) results in a mitigation of these effects. The samples with 3.0% and 4.5% also show some degree of porosity. When compared to the HC-LBC series samples, the scarcity of carbon inclusions visible in the microstructures of the higher carbon samples suggest that much of the phenolic resin was lost during processing or poorly mixed so as to reduce the amount of effective carbon in the bulk of the sample. Evidence of this is also seen in Figure 56.

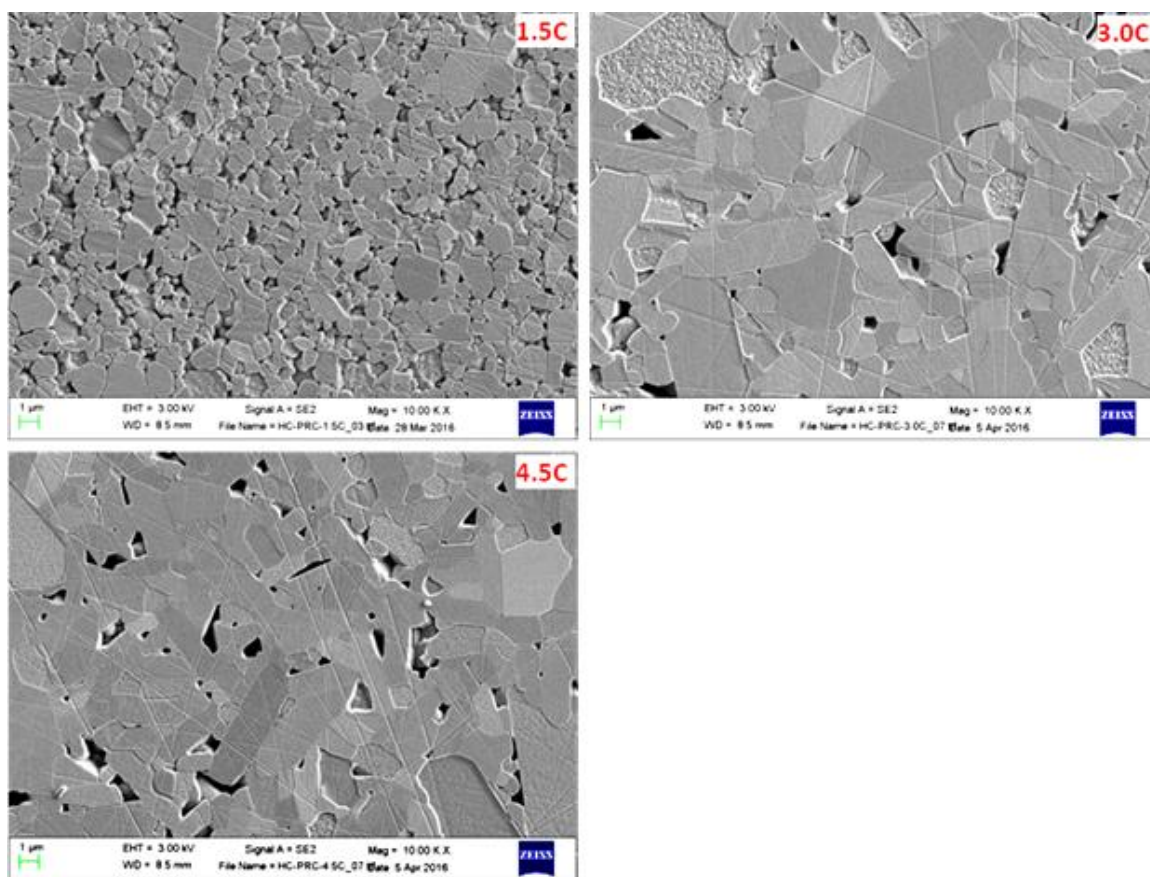
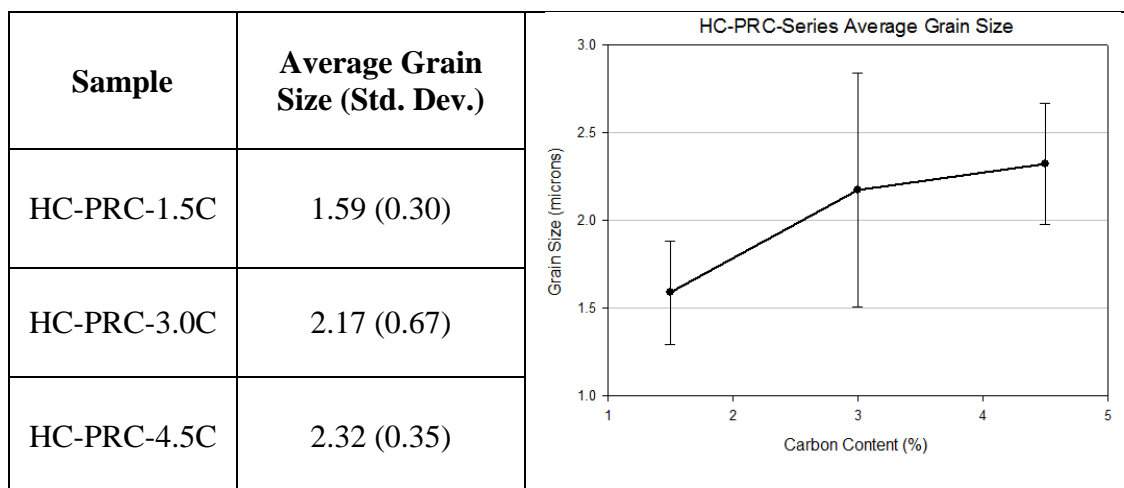


Figure 55. HC-PRC-Series microstructures at 10000x magnification

Table 24. HC-PRC-Series average grain sizes measured by the linear intercepts method



While the 3.0% and 4.5% samples show generally similar microstructures, the 4.5% sample showed some large clusters of carbon inclusions that were not seen in the 3.0% sample. One such cluster is shown below in Figure 56.

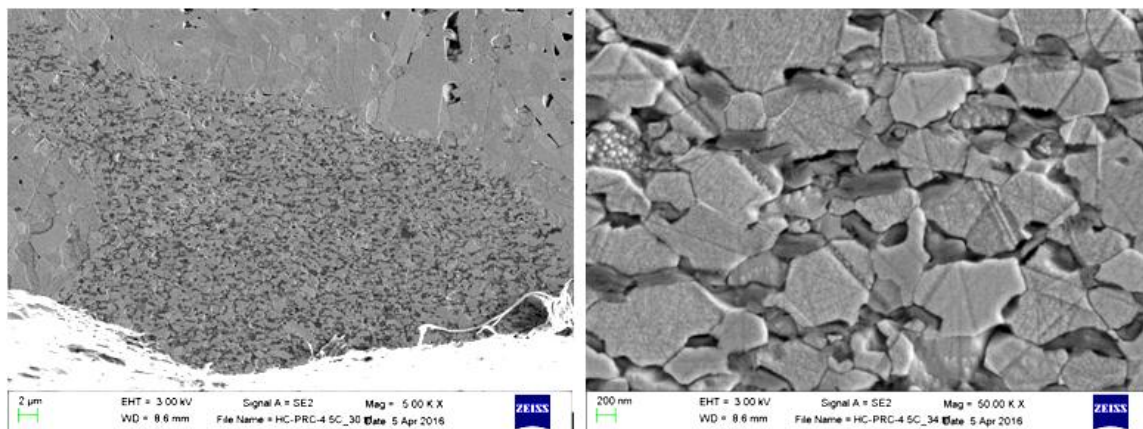


Figure 56. Sample HC-PRC-4.5C showing a large cluster of carbon inclusions (5000x and 50000x magnification)

Figure 57 shows EBSD maps of the HC-PRC series of samples. In the maps shown below, the red color indicates grains of the 6H SiC polytype and the green color shows the 4H SiC grains. The black color indicates areas where neither phase found due to the presence of secondary phases, pores, roughness, grain boundaries, or other factors. The investigated areas of each sample appear to be dominated by the 6H polytype with a smaller area appearing as 4H polytype. This is also shown in Table 25 which shows the phase fractions of each polytype present in the mapped areas. Due to the presence of the black areas mentioned before, the total areas of 6H and 4H do not add up to a full 100%. For the higher carbon samples, the ratio of 4H/6H SiC is fairly low, between 0.225 – 0.252, which is only slightly higher than the starting powder ratio of 0.152. For the lower carbon amount, the 4H/6H ratio is slightly higher at 0.368. However, there is a large portion of the EBSD map where neither polytype could be identified. This is due to the

presence of a second phase at the grain boundaries which is not identified as SiC and also causes significant charging. As such, the accuracy of the 4H/6H ratio measurement may not be as accurate as in the cleaner maps. In these samples, it does appear that differences in the oxygen content, which would decrease as the amount of carbon added increases, have an effect on the SiC polytype ratio. With lower carbon content, and consequently higher oxygen content, the 4H/6H ratio increases.

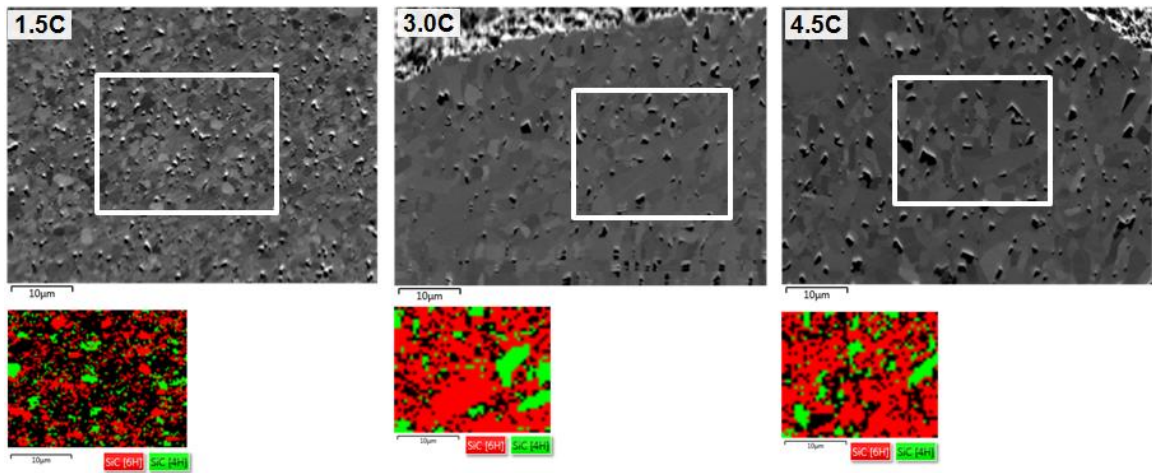


Figure 57. HC-PRC-Series EBSD Maps

Table 25. HC-PRC-Series phase fractions

Sample	Phase Fraction 4H (%)	Phase Fraction 6H (%)	4H/6H ratio
HC-PRC-1.5C	10	26	0.38
HC-PRC-3.0C	16	62	0.26
HC-PRC-4.5C	13	57	0.23

5.3.5.2. Mechanical Properties

The densities of the HC-PRC-Series samples were determined using Archimedes' method and the elastic properties were measured using the nondestructive ultrasonic

techniques and are shown below in Table 26. The longitudinal and shear sound speeds were measured directly and the Poisson's Ratio and moduli were calculated from these values using the equations described in Section 4.5.2. The elastic properties were plotted against the carbon content as shown below in Figure 58. In these samples, the density decreases with the amount of added carbon, as would be expected. However, the elastic properties are very similar between the three samples, suggesting that the bulk of the samples were very similar and that the residual carbon clusters may not have been interrogated by the ultrasound beam at the locations where measurements were taken.

Table 26. HC-PRC-Series elastic properties

Sample	c_L (m/s)	c_s (m/s)	Poisson	Density (g/cm ³)	E (GPa)	G (GPa)	K (GPa)
HC-PRC-1.5C	12000	7550	0.17	3.17	424	181	216
HC-PRC-3.0C	12050	7610	0.17	3.15	426	182	214
HC-PRC-4.5C	11980	7610	0.16	3.14	422	182	207

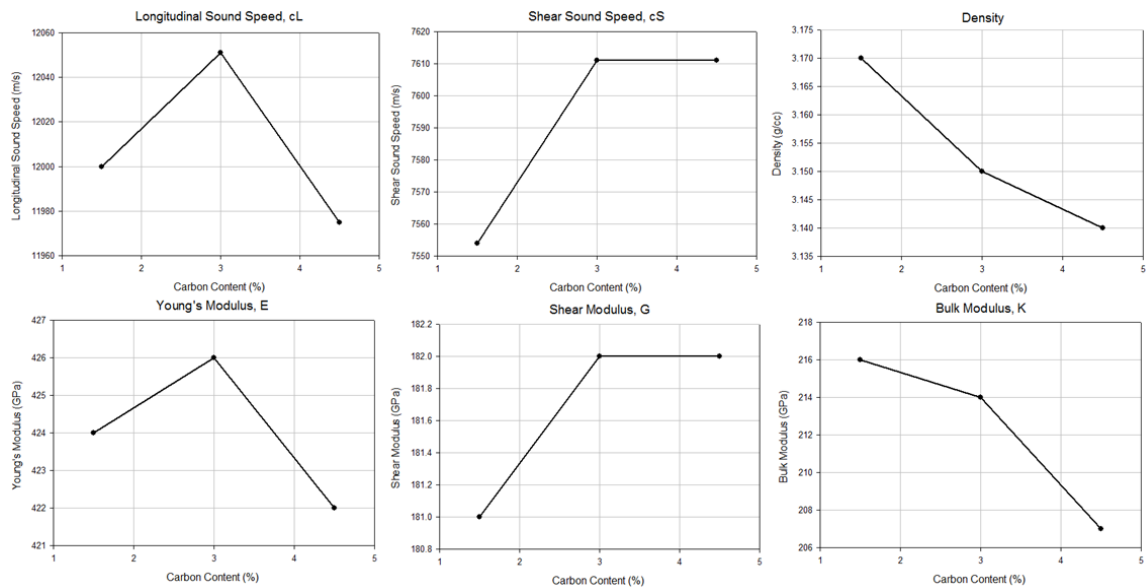


Figure 58. HC-PRC-Series elastic properties vs. carbon content

Knoop microhardness testing was performed on each sample in the HC-PRC series with 10 indents at each of five different loads (100 g, 300 g, 500 g, 1000 g, 2000 g). Load-hardness curves for each sample are shown below in Figure 59. As with the elastic properties, the hardness values for these samples are quite similar, again suggesting that the indented areas were very similar and the indents most likely missed the large carbon clusters. The similarity between the samples in this series are again shown in the 1000 g load Knoop hardness values as a function of carbon content which are shown below in Figure 60.

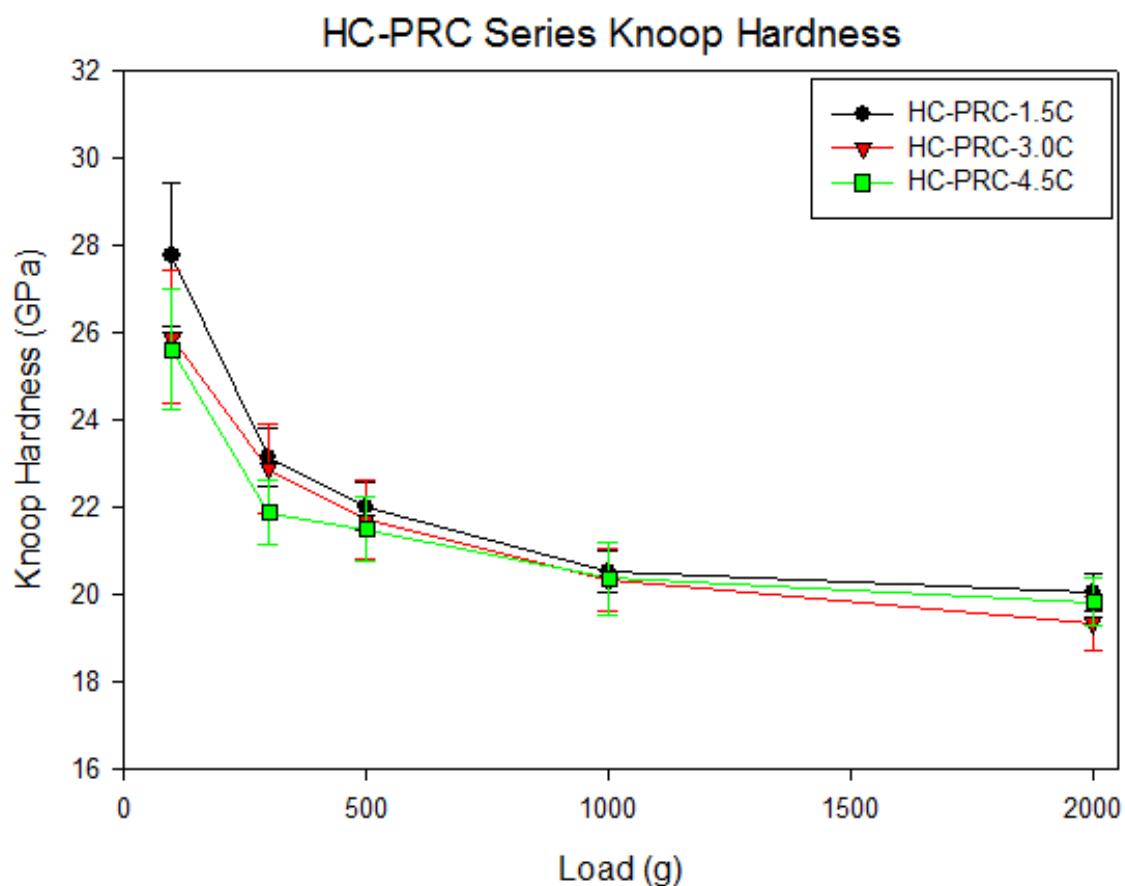


Figure 59. HC-PRC-Series Knoop Hardness curves

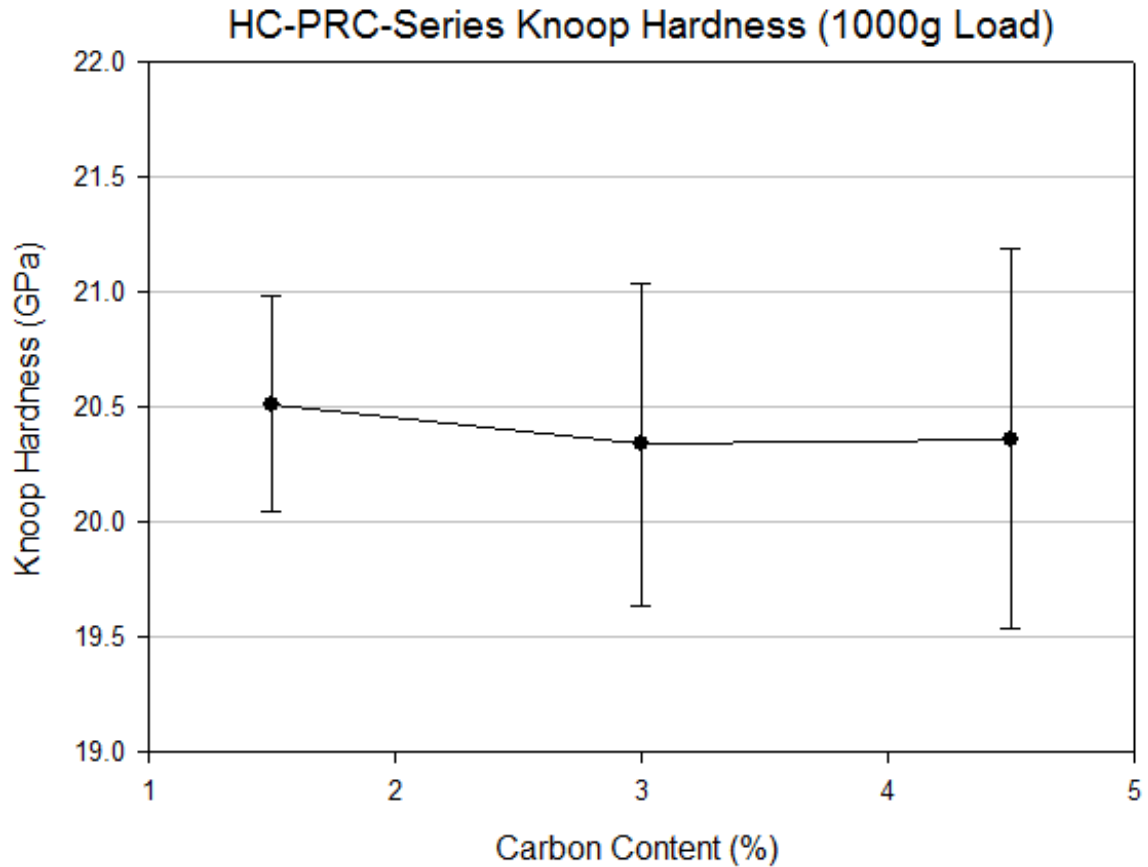


Figure 60. HC-PRC-Series Knoop Hardness at 1000 g load

5.3.5.3. Ultrasound Analysis

Figure 61 below shows the attenuation coefficient spectra for the HC-PRC series samples. The samples all show fairly similar behavior at lower frequencies below 30 MHz but differ significantly at frequencies above 40 MHz. Looking at the microstructures of the different samples, there seems to be some explanation for the differences in the attenuation spectra between samples. In the HC-PRC samples, there are a number of differences between the samples that could be causing the differences in the attenuation spectra. The grain size and shape, as well as secondary phase content, inclusions, and porosity are all different between the samples and all affect the attenuation. While the 3.0% and 4.5% samples show generally similar microstructures,

the 4.5% sample showed some large clusters of carbon inclusions that were not seen in the 3.0% sample and which may be one contribution to their dramatically different attenuation spectra.

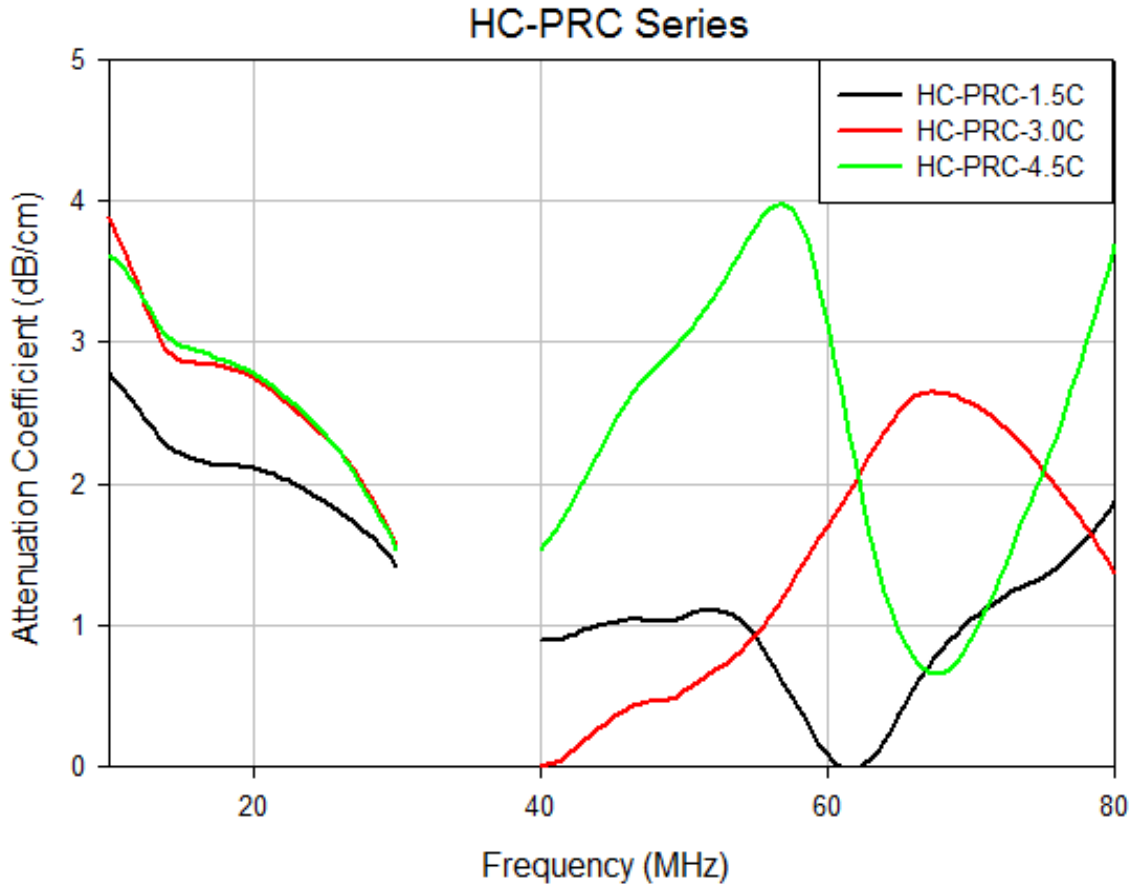


Figure 61. HC-PRC-Series ultrasound attenuation spectra

5.3.6. HC-AW-Series

5.3.6.1. Microstructure Characterization

Figure 62 shows the microstructures of the HC-AW series of samples. At the two lower oxygen levels, the samples appear to be fairly similar in microstructure. Both samples are nearly fully dense and display some large, elongated grains. However, most of the grains tend to be smaller. In both samples, the smaller grains are still somewhat elongated, but not as much as the very large grains. This elongation of the smaller grains

is more pronounced in the intermediate oxygen sample, resulting in a wider grain size distribution as measured by the linear intercepts method. This behavior is reflected in Table 27.

In the lowest oxygen sample, some small carbonaceous inclusions are seen, but as the oxygen content increases to an intermediate level, there are very few inclusions left behind. This suggests that the amount of carbon added was enough to remove the lower amount of oxygen but not quite enough for the intermediate amount. The high oxygen sample shows a much smaller grain size with almost completely equiaxed morphology. It also appears to be severely over-etched even though the same etching procedure was used as the other samples. Further investigation showed the presence of an oxygen rich secondary phase at the grain boundaries, and no carbonaceous inclusions. This suggests that the amount of carbon added was insufficient to remove the oxygen and that there was enough left over to produce a separate second phase, likely an oxygen rich, oxycarbide glass similar to that seen by Sajgalik in the triple points of samples made using annealed, granulated SiC powders.[69] EDS maps showing this secondary phase are shown in Figure 63.

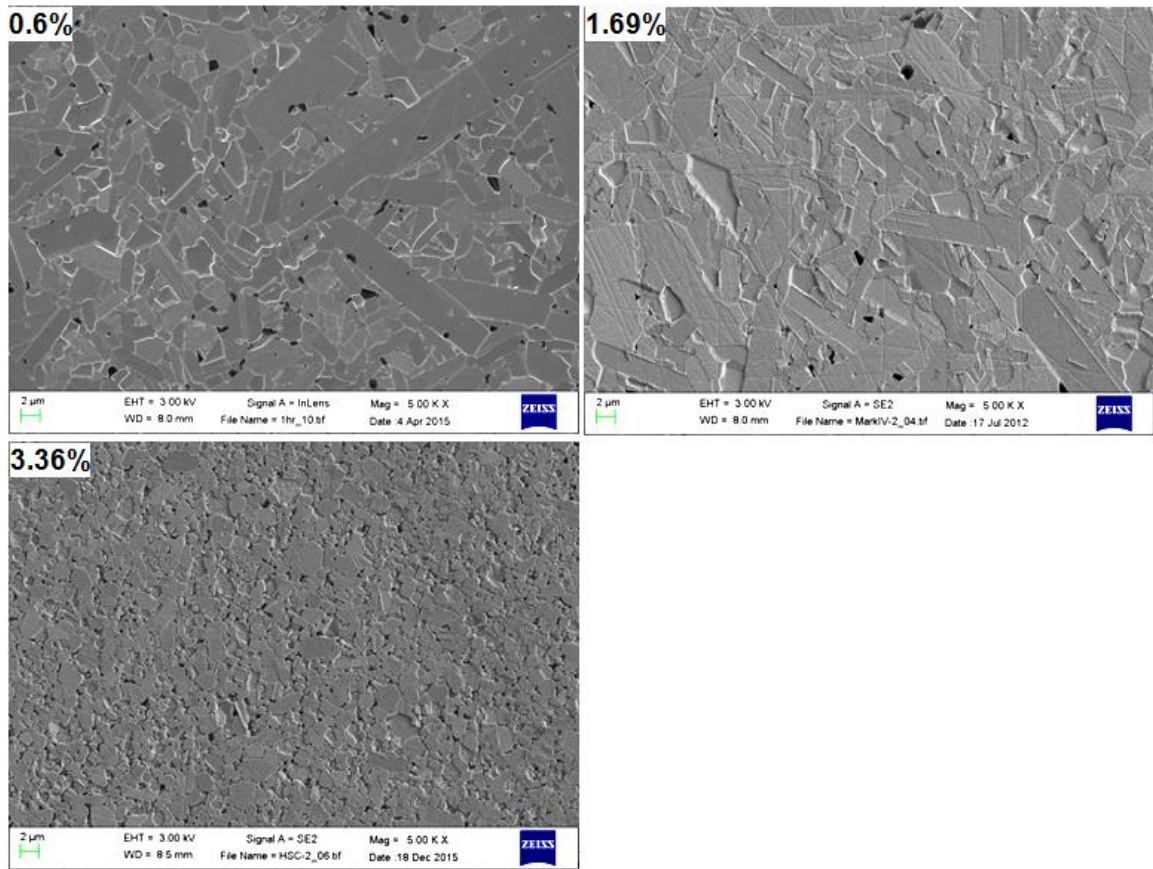


Figure 62. HC-AW-Series microstructures at 5000x magnification

Table 27. HC-AW-Series average grain sizes measured by the linear intercepts method

Sample	Average Grain Size (Std. Dev.)	
HC-AW-0.6%	2.89 (0.99)	
HC-AW-1.69%	2.28 (1.91)	
HC-AW-3.36%	1.21 (0.24)	

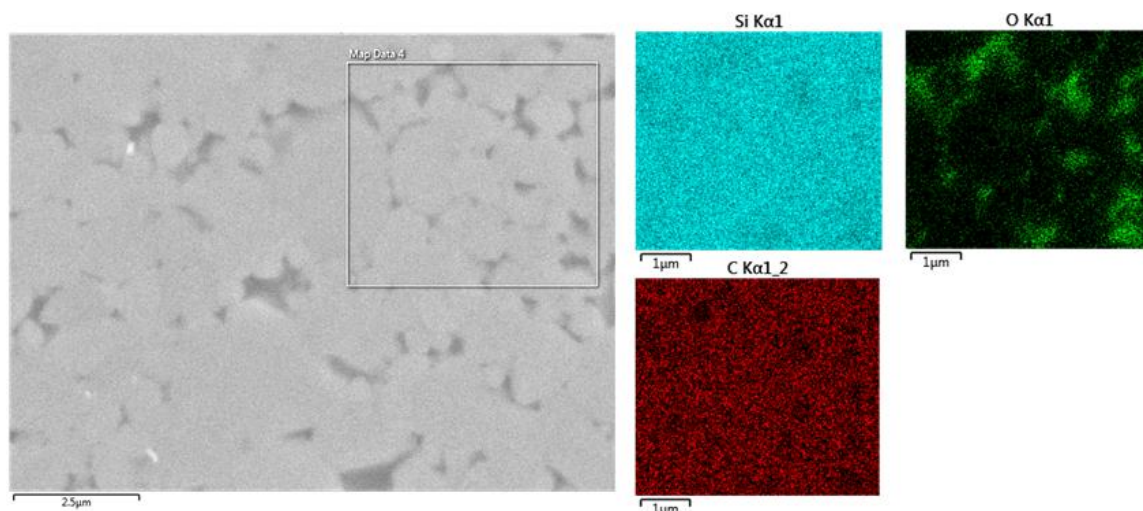


Figure 63. EDS maps of HC-AW-3.36% showing oxygen rich second phase

Figure 64 shows EBSD maps of the HC-AW series of samples. In each of the maps shown, the red color indicates the presence of the 6H SiC polytype and the green color shows the 4H SiC polytype. The black color indicates areas where neither phase found due to the presence of secondary phases, pores, roughness, grain boundaries, or other factors. The investigated areas of each sample are dominated by grains of the 6H polytype while a smaller fraction of the grains are 4H. In the 0.6% oxygen content sample, the 4H polytype is seen more often in the elongated grains while 6H is seen mainly in the smaller more equiaxed grains. This same type of behavior is also seen in the 1.69% oxygen sample. In the 3.36% oxygen sample, the large amount of secondary phase material makes it difficult to obtain clear EBSD maps of the SiC polytypes. This is also reflected in Table 28 which shows the phase fractions of each polytype present in the mapped areas. Due to the presence of the black areas mentioned before, the total areas of 6H and 4H do not add up to a full 100%. For all of these samples, the ratio of 4H/6H SiC is in a similar range between 0.426 – 0.564, which is higher than the starting powder ratio of 0.152. In this case, it does not appear that the oxygen content has much of an effect on

the 4H to 6H ratio, as all of the samples have an elevated concentration of 4H. This may again be attributed to the formation of an oxycarbide glass phase that forms a transient melt during sintering as claimed by Sajgalik et al.[69] This phase is also present even in the lowest oxygen sample as acid washing with HF has been shown to leave silicon oxycarbide phases on the particle surfaces.[30] In the high oxygen case, the overabundance of the second phase appears to suppress the growth of elongated grains but still facilitates the transformation from 6H to 4H.

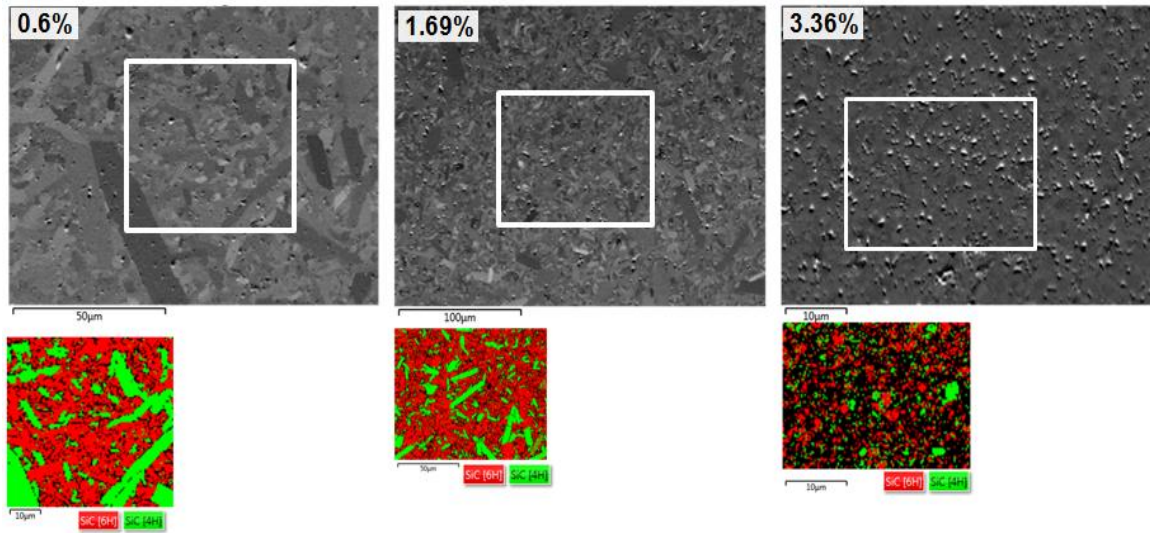


Figure 64. HC-AW-Series EBSD Maps

Table 28. HC-AW-Series phase fractions

Sample	Phase Fraction 4H (%)	Phase Fraction 6H (%)	4H/6H ratio
HC-AW-0.6%	30	53	0.57
HC-AW-1.69%	23	53	0.43
HC-AW-3.36%	11	24	0.46

5.3.6.2. Mechanical Properties

The densities of the HC-AW-Series samples were determined using Archimedes' method and the elastic properties were measured using the nondestructive ultrasonic techniques and are shown below in Table 29. The longitudinal and shear sound speeds were measured directly and the Poisson's Ratio and moduli were calculated from these values using the equations described in Section 4.5.2. The elastic properties were plotted against the carbon content as shown below in Figure 65. The two lower oxygen content samples both reach full density while the density is reduced in the highest oxygen content sample due to the presence of the secondary phase. The sample with the greatest elastic properties is actually the intermediate oxygen sample as the lowest oxygen sample still has some residual carbon inclusions in the microstructure while the highest oxygen sample has the secondary phase reducing the elastic properties. It is clear however that the greatly increased oxygen content is detrimental to the elastic properties.

Table 29. HC-AW-Series elastic properties

Sample	c_L (m/s)	c_S (m/s)	Poisson	Density (g/cm³)	E (GPa)	G (GPa)	K (GPa)
HC-AW-0.6%	12030	7640	0.16	3.21	435	187	215
HC-AW-1.69%	12270	7820	0.16	3.20	453	195	221
HC-AW-3.36%	11760	7400	0.17	3.15	405	173	206

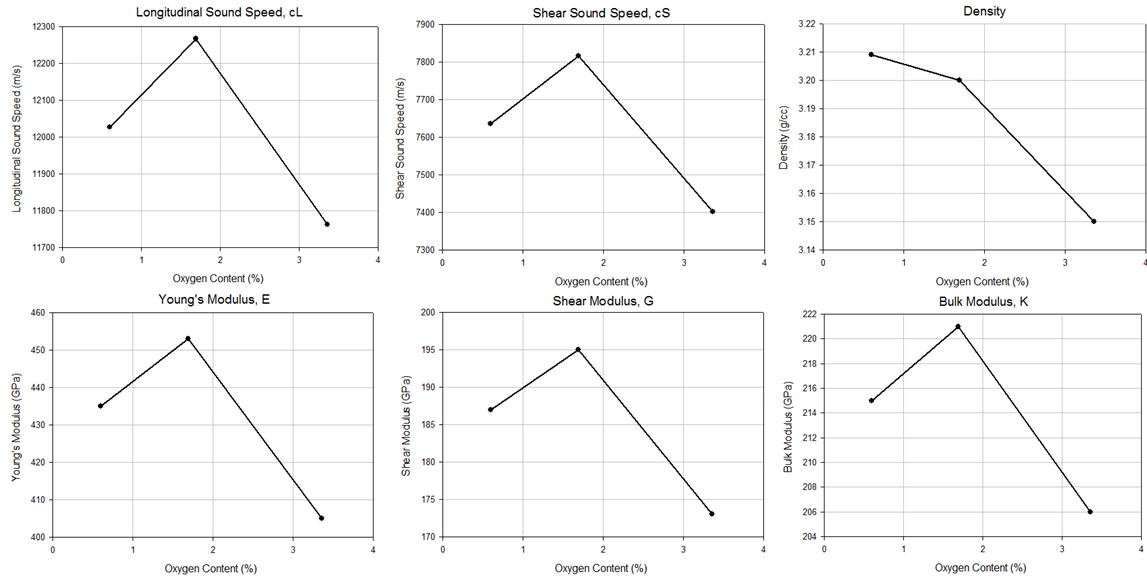


Figure 65. HC-AW-Series elastic properties vs. oxygen content

Knoop microhardness testing was performed on each sample in the HC-AW series with 10 indents at each of five different loads (100 g, 300 g, 500 g, 1000 g, 2000 g). Load-hardness curves for each sample are shown below in Figure 66. The hardness of the two lower oxygen content samples is quite similar over the entire load range while the highest oxygen content sample is significantly lower. Like with the elastic properties, this is due to the presence of the softer, oxygen-rich secondary phase.

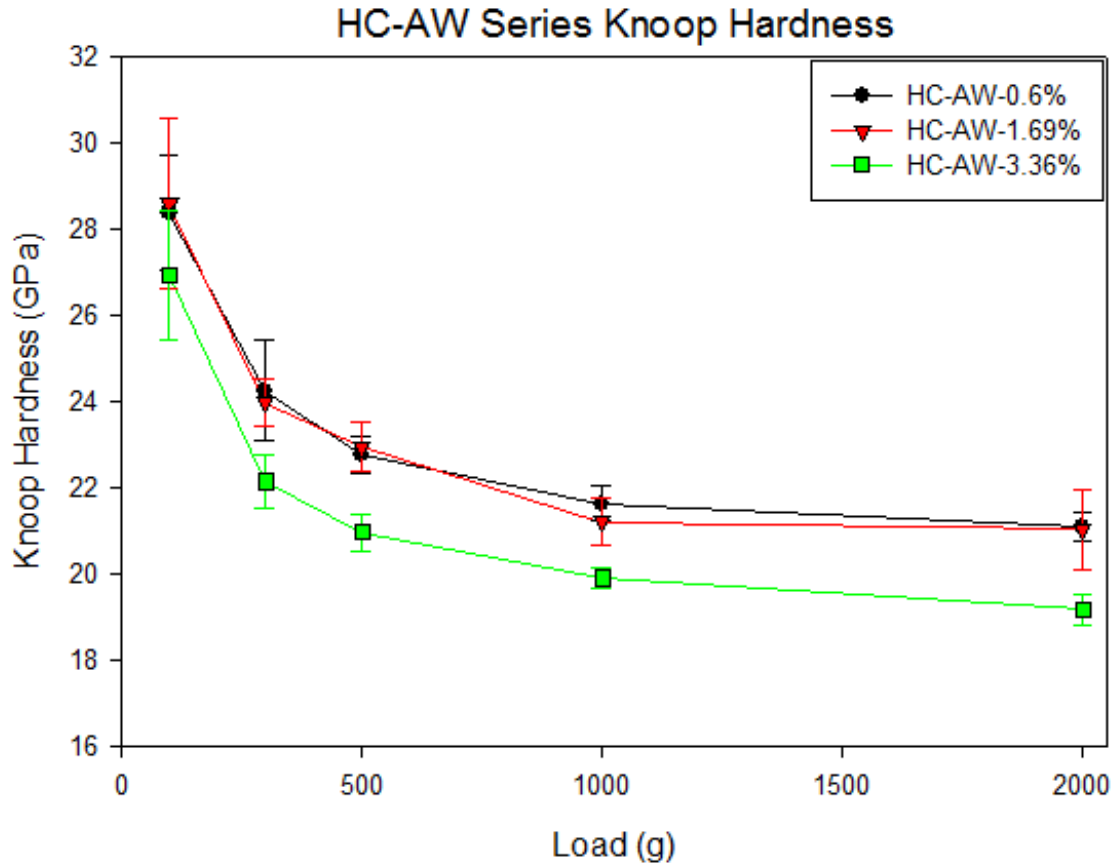


Figure 66. HC-AW-Series Knoop Hardness curves

The 1000 g load Knoop hardness values for each sample in the series as a function of oxygen content are shown below in Figure 67. It is clear that the increase in oxygen content has a negative effect on the Knoop microhardness measured for these samples. At the higher oxygen content, the large amount of a softer second phase material is the cause of this decrease in hardness.

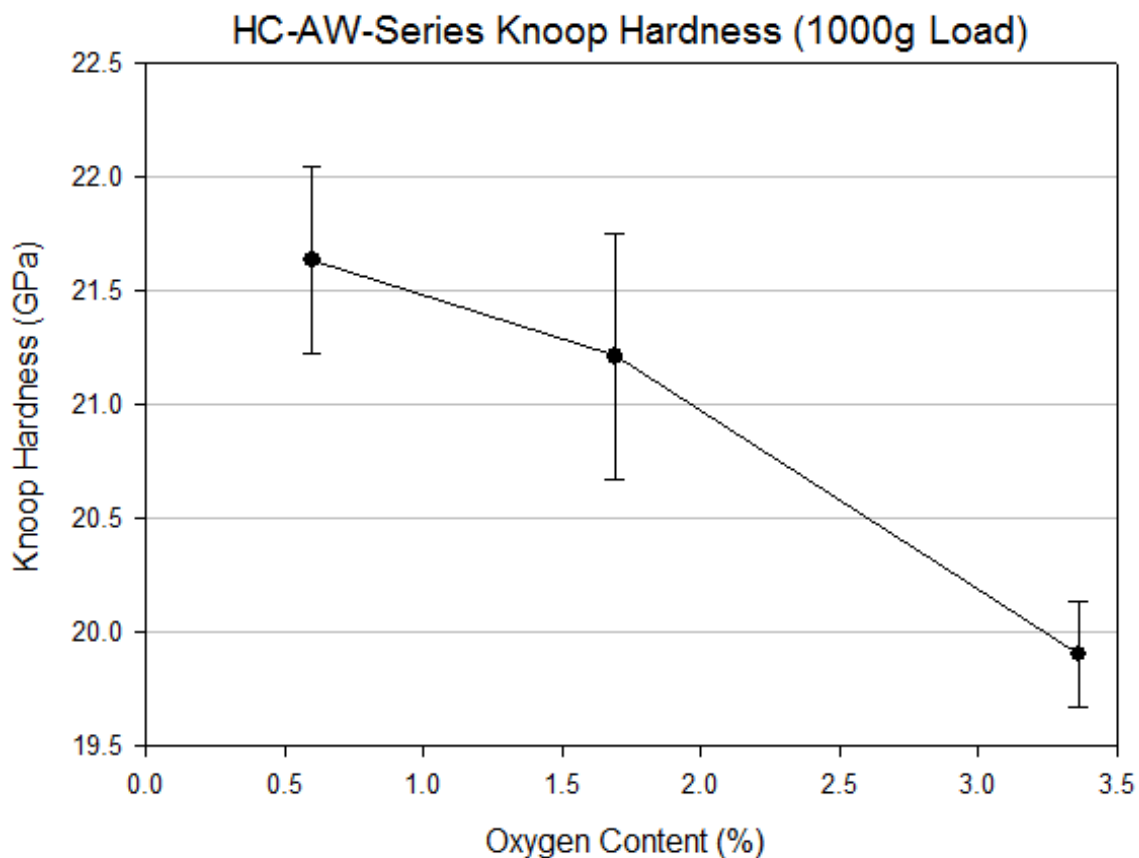


Figure 67. HC-AW-Series Knoop Hardness at 1000 g load

Pieces of each HC-AW-Series sample were broken and the fracture surfaces were examined in the FESEM. Micrographs of the fracture surfaces are shown below in Figure 68. As with the SG-AW-Series, each of the three samples appears to show mixed mode fracture, with some intergranular fracture taking place around some of the smaller grains, but with a significant amount of transgranular fracture through many of the grains. This is most obvious in the lower oxygen content samples where the fracture surface goes straight through some of the larger grains leaving large flat areas on the surface.

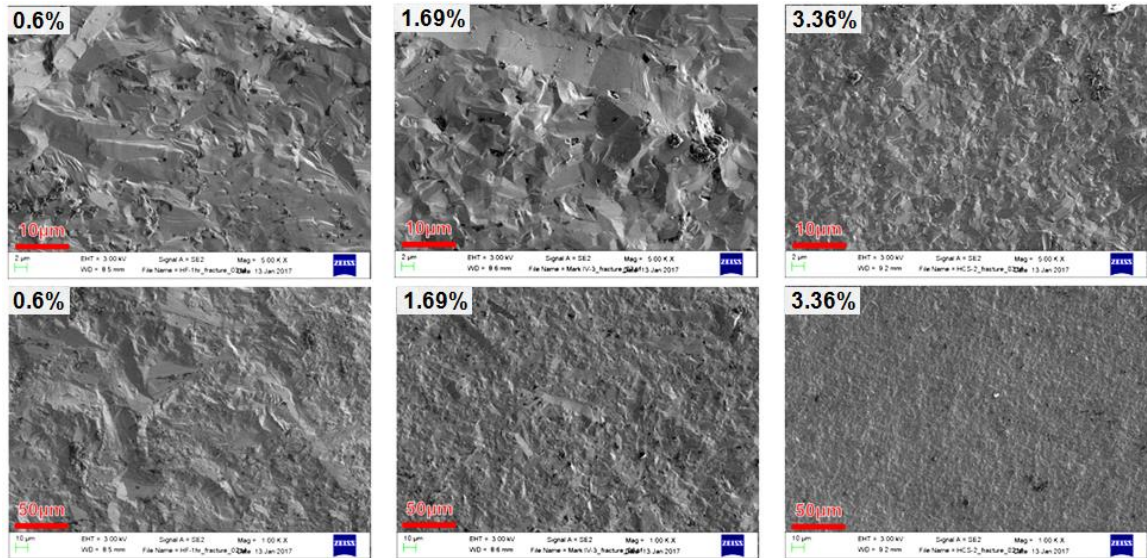


Figure 68. HC-AW-Series fracture surface images at 5000x magnification (top row) and 1000x magnification (bottom row)

5.3.6.3. Ultrasound Analysis

Figure 69 below shows the attenuation coefficient spectra for the HC-AW series samples. In the two higher oxygen samples, the low frequency attenuation spectra are very similar in shape and show a decreasing attenuation coefficient over the 10 – 30 MHz range. However, the lowest oxygen content sample shows an increase in attenuation even at these low frequencies. At higher frequencies, the attenuation coefficient of the low oxygen sample continues to increase sharply and shows power-law type behavior. The two samples with higher oxygen content show only a slight increase in attenuation coefficient at higher frequencies, with the intermediate oxygen sample jumping in attenuation above about 65 MHz. The generally flat attenuation behavior seen in the high oxygen sample is typical of a very fine grained SiC material and this is corroborated by the microstructural images.

The kind of variability in the attenuation of the intermediate oxygen sample at high frequencies is also seen in several of the other samples and is likely caused by the nonuniform microstructure seen in this sample. The power-law type behavior of lowest oxygen content sample would typically suggest an equiaxed grain structure, but looking at the microstructural images, it appears to be very similar to that of the intermediate oxygen content sample, with a number of very large elongated grains surrounded by smaller grains, some of which are elongated and some are more equiaxed. This power-law type attenuation behavior could also be caused by the presence of large second phase inclusions on the order of 100+ microns. However, there was no evidence of this in the microstructural images, so the cause of this behavior in this sample is not known.

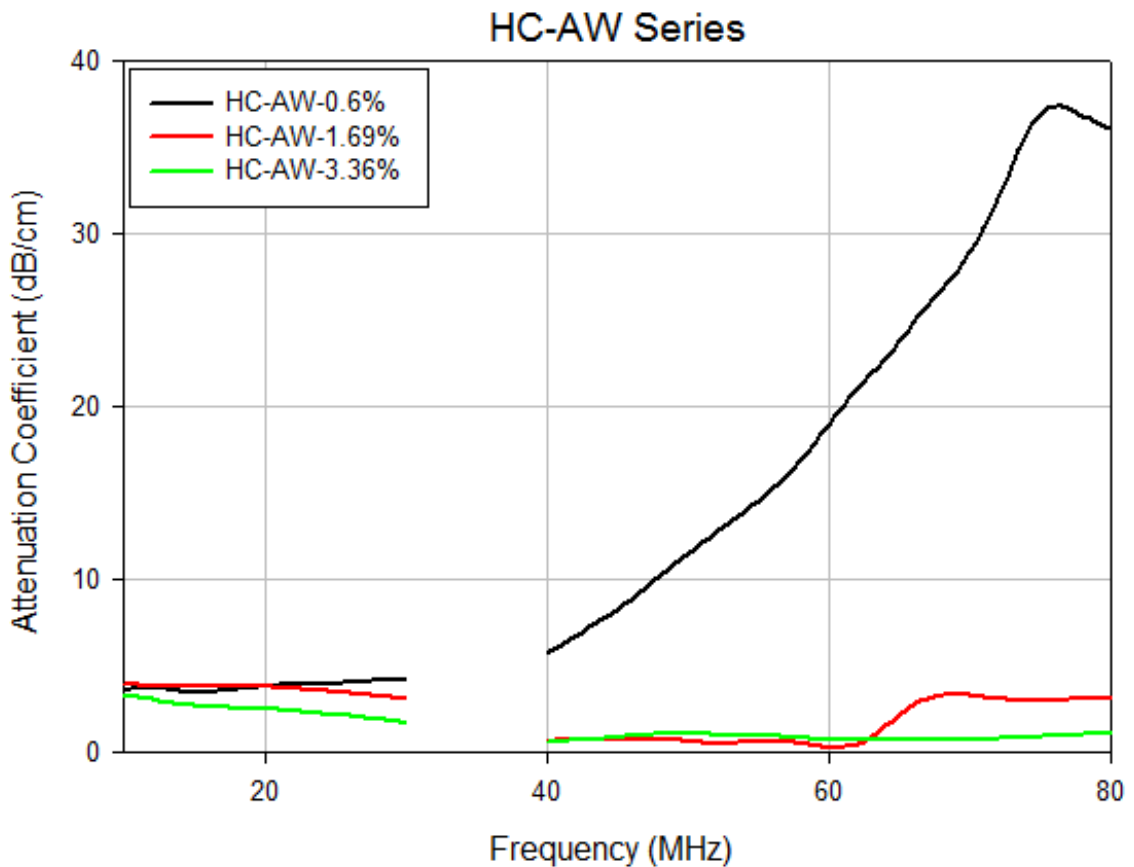


Figure 69. HC-AW-Series ultrasound attenuation spectra

6. Conclusions

6.1. Microstructure

It is clear that the oxygen content of silicon carbide powders has a number of effects on the microstructure of dense silicon carbide ceramics produced by spark plasma sintering.

Density: When keeping the composition constant, increasing the oxygen content of the SiC powder lowers the density of the sintered body. This can be due to the inhibition of densification which results in a more porous microstructure as seen in the SG-AW-Series, or by the formation of a less dense secondary phase as seen in the HC-AW-Series. When the oxygen content is modified by changing the amount of carbon added as in the SG-LB, SG-PR, HC-LB, and HC-PR-Series samples, similar effects are seen. At low carbon amounts (higher oxygen), the densified bodies show inhibited densification and an increase in porosity. With higher carbon additions (lower oxygen), the porosity is eliminated, but the presence of residual carbon inclusions serves to reduce the overall density.

Grain Size: When keeping the composition constant, the oxygen content of the powder affects the grain size differently depending on how much oxygen is present and which of the two SiC powders was used. With the SG-SiC powder, using low oxygen content powder results in a fine average grain size of 5.43 μm . Increasing the oxygen content to an intermediate amount results in much more extreme grain growth and an average grain size of 13.80 μm and a much wider size distribution. When oxygen content is increased even further, the sample again shows a fine average grain size of 4.18 μm where further grain growth is inhibited by residual porosity. With the HC-SiC powder,

lower oxygen content powders result in similar grain sizes, with averages of 2.89 μm and 2.28 μm for the lowest and intermediate oxygen contents. At the highest oxygen content, the average grain size drops to 1.21 μm as grain growth appears to be inhibited by the presence of a secondary phase between the SiC grains. When the oxygen content is modified by the addition of different amounts of carbon in both particulate and resin forms, there is not much difference in grain size between samples. This is likely due to the presence of carbonaceous inclusions blocking the growth of the SiC grains.

Grain Shape: The shape of SiC grains can vary dramatically when the powder oxygen content is changed and the composition is held constant. In the SG-AW-Series, the lowest and highest oxygen content samples maintained fairly equiaxed grains and small grain size. However, at intermediate oxygen content, a majority of the grains by volume became very large and elongated, with aspect ratios of 10:1 or more in some cases. In the case of the HC-AW-Series, the samples with low and intermediate oxygen contents had similar grain morphologies, showing a mix of primarily smaller, more equiaxed grains with aspect ratios of 2:1 or 3:1 at most and fewer large, elongated grains with higher aspect ratios. At the highest oxygen content, the grains became much smaller and equiaxed with few grains with higher than 2:1 aspect ratio. When modifying the oxygen content by adding varying amounts of carbon, there was not much difference in grain shape seen between most of the samples with the exception of the HC-SiC samples with the lowest amounts of added carbon. When using lampblack as the carbon source, the lowest carbon sample showed a mixture of equiaxed and elongated grains while the samples with more carbon displayed grains that were predominantly equiaxed. When using the phenolic resin as the carbon source, the lowest carbon sample showed small,

equiaxed grains with a microstructure similar to the highest oxygen HC-AW sample while the increased carbon samples showed mixed morphology microstructures like the lower oxygen content HC-AW samples. Since the additional carbon serves to eliminate additional oxygen, this is in agreement with the behavior seen in the HC-AW-Series.

Polytype Transformation: In all cases, the densified samples showed higher concentrations of the 4H polytype of silicon carbide than the starting powders. However, the ratio of 4H to 6H was much higher in the samples that showed increased grain growth and elongation. In most cases, these large, elongated grains were found to be of the 4H polytype while equiaxed grains tended to be primarily 6H polytype.

6.2. Mechanical Properties

Because the mechanical properties of a material are often highly dependent on the microstructure of that material, and because the oxygen contents of silicon carbide powders affect the microstructure of dense silicon carbide in a number of ways, it is clear that the oxygen content also affects the mechanical properties.

Elastic Moduli: The effect of oxygen content on the elastic properties of silicon carbide ceramics is directly tied to the effect that oxygen content has on the density of the material. The differences in elastic properties are caused by the increase in either porosity or secondary phase inclusions in the silicon carbide microstructures caused by the variation of oxygen content. As such, the elastic moduli of samples that showed higher porosity or increased concentrations of secondary phase inclusion tended to be lower than those that were denser and had lower inclusion concentrations.

Acoustic Attenuation: The effect of the oxygen content on the acoustic attenuation of silicon carbide ceramics remains unclear. Unlike the alumina samples

examined by Bottiglieri which showed very clear power-law type scattering behavior at high frequencies, the silicon carbide samples displayed much more erratic attenuation spectra. While some of this behavior can be attributed to the nonspherical grain structure in some of the samples, the samples that showed more equiaxed grains did not show this kind of power-law type attenuation either. It is likely that several types of attenuation mechanisms are active in these samples which are not easily deconvoluted, making it impossible to accurately determine the scattering prefactors to predict microstructural features like grain size in this system.

Hardness: As with the elastic moduli, the influence of oxygen content on the hardness of the silicon carbide samples was related to its influence on the density and concentration of secondary phases in the dense bodies. When increasing the oxygen content increased the amount of porosity or generated a softer secondary phase, the hardness values decreased compared to those with lower oxygen contents. When more carbon was added to reduce the oxygen content, carbonaceous inclusions served to lower the hardness of the material. As such, the hardness of silicon carbide can be maximized by treating the powder to reduce oxygen content so that fully dense materials can be produced with a minimum of carbon additives, producing ceramics that are free of porosity and inclusions that reduce hardness.

Fracture: Despite the large differences in microstructure between samples made with powders of varying oxygen contents, there did not appear to be much of a difference in the fracture behavior seen in the SG-AW and HC-AW Series samples. While quantitative measurements of the fracture toughness were not performed, qualitative assessments of the fracture surfaces of broken samples showed very similar fracture

behavior. While large, elongated grains can often act as a toughening mechanism in some ceramics, the large grains seen in some of the SiC samples tended to fracture in a transgranular fashion. In other materials, having a weaker secondary phase at the grain boundaries can cause crack deflection and produce completely intergranular fracture, in the case where there was a significant amount of secondary phase material in the microstructure of HC-AW-3.36%, this type of behavior did not appear to be case. However this is likely due to the second phase material appearing mainly at triple points between grains and therefore not providing a continuous path for cracks to travel around the SiC grains.

7. Future Work

1. Pressureless sintering of silicon carbide powders with varied oxygen contents. Similar experiments should be conducted with samples densified by pressureless sintering to see if the microstructure and mechanical properties are affected in the same way as in SPS. It has been shown that pressure can stabilize other phases and increase the solution of aluminum impurities in SiC which may contribute to the stabilization of the 4H polytype. Pressureless sintering would also be of more interest commercially as spark plasma sintering is much more difficult to scale up.

2. High resolution transmission electron microscopy. High resolution TEM should be performed on the SiC samples with varied oxygen contents to look more closely at the grain boundaries. This may be able to shed more light on whether a transient liquid phase is forming or not. It would also be interesting to examine the grain boundary complexions as they may provide some clues as to why the different faces of the large plate-like grains grow at such different speeds in the intermediate oxygen content samples. TEM analysis should also be performed on the oxidized powders to determine whether the oxygen forms silica or an oxycarbide glass on the surface.

3. Sample size scale-up. The samples made for this work were all fairly small disks 20 mm in diameter and roughly 6 mm in thickness. Making larger samples with varied shapes would be of interest to see if the oxygen content has the same effects as in the smaller samples and if there are gradients in the properties as a result of larger distances for the removal of oxygen.

4. Produce samples with more varied oxygen contents. The work on the AW-Series samples focused on the extreme ends of the oxygen content spectrum with an

intermediate level in between. Samples with more varied intermediate oxygen contents should be made to see if there are additional transitions in behavior at levels between the low and intermediate oxygen levels and intermediate and high oxygen levels examined in this work.

5. Modeling of ultrasound interactions with non-ideal microstructures. More investigation should be done to better understand the acoustic physics at work in ceramic systems and their interactions with ultrasound energy. The SiC materials investigated in this work did not closely follow the expected ultrasound behavior for ceramic materials as described by Portune and Bottiglieri. This was likely due to the presence of non-spherical grains with varying size distributions as well as the presence of secondary phases of various sizes, shapes, concentrations, and compositions. More work must be done to understand how these factors, both individually and when taken together, contribute to the attenuation behavior in order to enable useful nondestructive characterization.

8. References

- [1] E. G. Acheson, "Production of Artificial Crystalline Carbonaceous Materials," USA Patent 492767, 1893.
- [2] R. Munro, "Material properties of a sintered α -SiC," *Journal of Physical and Chemical Reference Data*, vol. 26, pp. 1195-1203, 1997.
- [3] J. D. Kiser, S. R. Levine, and J. A. Dicarlo, "Ceramics for Engines," *Aeropropulsion 1987*, pp. 91-103, 1987.
- [4] M. Bhatnagar and B. J. Baliga, "Comparison of 6H-SiC, 3C-SiC, and Si for power devices," *Electron Devices, IEEE Transactions on*, vol. 40, pp. 645-655, 1993.
- [5] P. Shaffer, "A review of the structure of silicon carbide," *Acta Crystallographica Section B: Structural Crystallography and Crystal Chemistry*, vol. 25, pp. 477-488, 1969.
- [6] C. B. Carter and M. G. Norton, *Ceramic materials : science and engineering*. New York: Springer, 2007.
- [7] H. Tanaka, "Silicon carbide powder and sintered materials," *Journal of the Ceramic Society of Japan*, vol. 119, pp. 218-233, 2011.
- [8] D. Lundqvist, "On the crystal structure of silicon carbide and its content of impurities," *Acta Chemica Scandinavica*, vol. 2, p. 177, 1948.
- [9] S. Nakashima and H. Harima, "Raman investigation of SiC polytypes," *physica status solidi (a)*, vol. 162, pp. 39-64, 1997.
- [10] S. i. Nakashima, M. Higashihira, K. Maeda, and H. Tanaka, "Raman Scattering Characterization of Polytype in Silicon Carbide Ceramics: Comparison with X-ray Diffraction," *Journal of the American ceramic society*, vol. 86, pp. 823-829, 2003.
- [11] J. Ruska, L. Gauckler, J. Lorenz, and H. Rexer, "The quantitative calculation of SiC polytypes from measurements of X-ray diffraction peak intensities," *Journal of materials science*, vol. 14, pp. 2013-2017, 1979.
- [12] A. L. Ortiz, F. L. Cumbreira, F. Sánchez-Bajo, F. Guiberteau, H. Xu, and N. P. Padture, "Quantitative Phase-Composition Analysis of Liquid-Phase-Sintered Silicon Carbide Using the Rietveld Method," *Journal of the American Ceramic Society*, vol. 83, pp. 2282-2286, 2000.
- [13] A. Ortiz, F. Sánchez-Bajo, N. Padture, F. Cumbreira, and F. Guiberteau, "Quantitative polytype-composition analyses of SiC using X-ray diffraction: a critical comparison between the polymorphic and the Rietveld methods," *Journal of the European ceramic society*, vol. 21, pp. 1237-1248, 2001.
- [14] H. Tanaka, N. Hirotsuki, T. Nishimura, D. W. Shin, and S. S. Park, "Nonequiaxial Grain Growth and Polytype Transformation of Sintered α -Silicon Carbide and β -Silicon Carbide," *Journal of the American Ceramic Society*, vol. 86, pp. 2222-2224, 2003.
- [15] X. F. Zhang, Q. Yang, and L. C. De Jonghe, "Microstructure development in hot-pressed silicon carbide: effects of aluminum, boron, and carbon additives," *Acta materialia*, vol. 51, pp. 3849-3860, 2003.
- [16] Y. W. Kim, M. Mitomo, and H. Hirotsuru, "Grain growth and fracture toughness of fine-grained silicon carbide ceramics," *Journal of the American Ceramic Society*, vol. 78, pp. 3145-3148, 1995.

- [17] Y. W. Kim, M. Mitomo, and H. Hirotsumi, "Microstructural development of silicon carbide containing large seed grains," *Journal of the American Ceramic Society*, vol. 80, pp. 99-105, 1997.
- [18] Y. W. Kim, M. Mitomo, H. Emoto, and J. G. Lee, "Effect of initial α -phase content on microstructure and mechanical properties of sintered silicon carbide," *Journal of the American Ceramic Society*, vol. 81, pp. 3136-3140, 1998.
- [19] W. F. Knippenberg, "Growth Phenomena in Silicon Carbide," *Philips Research Reports*, vol. 18, pp. 161-274, 1963.
- [20] J. Quanli, Z. Haijun, L. Suping, and J. Xiaolin, "Effect of particle size on oxidation of silicon carbide powders," *Ceramics international*, vol. 33, pp. 309-313, 2007.
- [21] G. ERVIN, "Oxidation behavior of silicon carbide," *Journal of the American Ceramic Society*, vol. 41, pp. 347-352, 1958.
- [22] P. J. Jorgensen, M. E. Wadsworth, and I. B. Cutler, "Oxidation of silicon carbide," *Journal of the American Ceramic Society*, vol. 42, pp. 613-616, 1959.
- [23] D. Das, J. Farjas, and P. Roura, "Passive-Oxidation Kinetics of SiC Microparticles," *Journal of the American Ceramic Society*, vol. 87, pp. 1301-1305, 2004.
- [24] Z. Zheng, R. E. Tressler, and K. E. Spear, "Oxidation of Single-Crystal Silicon Carbide Part I. Experimental Studies," *Journal of The Electrochemical Society*, vol. 137, pp. 854-858, 1990.
- [25] Z. Zheng, R. E. Tressler, and K. E. Spear, "Oxidation of Single-Crystal Silicon Carbide Part II. Kinetic Model," *Journal of The Electrochemical Society*, vol. 137, pp. 2812-2816, 1990.
- [26] S. Baik and P. F. Becher, "Effect of oxygen contamination on densification of TiB₂," *Journal of the American Ceramic Society*, vol. 70, pp. 527-530, 1987.
- [27] M. Johnson, M. Zvanut, and O. Richardson, "HF chemical etching of SiO₂ on 4H and 6H SiC," *Journal of Electronic Materials*, vol. 29, pp. 368-371, 2000.
- [28] S. Dhar, O. Seitz, M. D. Halls, S. Choi, Y. J. Chabal, and L. C. Feldman, "Chemical properties of oxidized silicon carbide surfaces upon etching in hydrofluoric acid," *Journal of the American Chemical Society*, vol. 131, pp. 16808-16813, 2009.
- [29] S. W. King, R. J. Nemanich, and R. F. Davis, "Wet Chemical Processing of (0001) Si 6H-SiC Hydrophobic and Hydrophilic Surfaces," *Journal of The Electrochemical Society*, vol. 146, pp. 1910-1917, 1999.
- [30] S. A. Corrêa, C. Radtke, G. V. Soares, I. J. Baumvol, C. Krug, and F. C. Stedile, "Presence and resistance to wet etching of silicon oxycarbides at the SiO₂/SiC interface," *Electrochemical and Solid-State Letters*, vol. 11, pp. H258-H261, 2008.
- [31] W. D. Callister, *Materials science and engineering : an introduction*, 5th ed. New York: Wiley, 2000.
- [32] J. S. Reed and J. S. Reed, *Principles of ceramics processing*, 2nd ed. New York: Wiley, 1995.
- [33] M. W. Barsoum, *Fundamentals of ceramics*. New York: McGraw Hill, 1997.
- [34] L. Stobierski and A. Gubernat, "Sintering of silicon carbide I. Effect of carbon," *Ceramics international*, vol. 29, pp. 287-292, 2003.

- [35] W. J. Clegg, "Role of Carbon in the Sintering of Boron-Doped Silicon Carbide," *Journal of the American Ceramic Society*, vol. 83, pp. 1039-1043, 2000.
- [36] K. Biswas, "Solid state sintering of SiC-ceramics," in *Materials Science Forum*, 2009, pp. 71-89.
- [37] S. PROCHAZKA and R. M. SCANLAN, "Effect of boron and carbon on sintering of SiC," *Journal of the American Ceramic Society*, vol. 58, pp. 72-72, 1975.
- [38] R. Alliegro, L. Coffin, and J. Tinklepaugh, "Pressure-Sintered Silicon Carbide," *Journal of the American Ceramic Society*, vol. 39, pp. 386-389, 1956.
- [39] K. Negita, "Effective sintering aids for silicon carbide ceramics: reactivities of silicon carbide with various additives," *Journal of the American Ceramic Society*, vol. 69, pp. C-308-C-310, 1986.
- [40] L. Stobierski and A. Gubernat, "Sintering of silicon carbide II. Effect of boron," *Ceramics international*, vol. 29, pp. 355-361, 2003.
- [41] W. v. Rijswijk and D. J. Shanefield, "Effects of carbon as a sintering aid in silicon carbide," *Journal of the American Ceramic Society*, vol. 73, pp. 148-149, 1990.
- [42] R. Hamminger, "Carbon inclusions in sintered silicon carbide," *Journal of the American Ceramic Society*, vol. 72, pp. 1741-1744, 1989.
- [43] M. Rączka, G. Górny, L. Stobierski, and K. Rożniatowski, "Effect of carbon content on the microstructure and properties of silicon carbide-based sinters," *Materials characterization*, vol. 46, pp. 245-249, 2001.
- [44] R. Aalund, "Spark plasma sintering," *Ceramic industry*, vol. 158, pp. 24-26, 2008.
- [45] Z. Munir, U. Anselmi-Tamburini, and M. Ohyanagi, "The effect of electric field and pressure on the synthesis and consolidation of materials: a review of the spark plasma sintering method," *Journal of Materials Science*, vol. 41, pp. 763-777, 2006.
- [46] F. Guillard, A. Allemand, J.-D. Lulewicz, and J. Galy, "Densification of SiC by SPS-effects of time, temperature and pressure," *Journal of the European ceramic Society*, vol. 27, pp. 2725-2728, 2007.
- [47] T. Yamamoto, H. Kitaura, Y. Kodera, T. Ishii, M. Ohyanagi, and Z. A. Munir, "Consolidation of Nanostructured β -SiC by Spark Plasma Sintering," *Journal of the American ceramic Society*, vol. 87, pp. 1436-1441, 2004.
- [48] A. Maitre, A. V. Put, J.-P. Laval, S. Valette, and G. Trolliard, "Role of boron on the Spark Plasma Sintering of an α -SiC powder," *Journal of the European Ceramic Society*, vol. 28, pp. 1881-1890, 2008.
- [49] Y. Zhou, K. Hirao, M. Toriyama, and H. Tanaka, "Silicon carbide ceramics prepared by pulse electric current sintering of β -SiC and α -SiC powders with oxide and nonoxide additives," *Journal of materials research*, vol. 14, pp. 3363-3369, 1999.
- [50] K. Inoue, "Electric-discharge sintering," USA Patent 3241956, 1966.
- [51] K. Inoue, "Apparatus for electrically sintering discrete bodies," 3250892, 1966.
- [52] J. Garay, "Current-activated, pressure-assisted densification of materials," *Annual review of materials research*, vol. 40, pp. 445-468, 2010.
- [53] D. M. Hulbert, A. Anders, D. V. Dudina, J. Andersson, D. Jiang, C. Unuvar, *et al.*, "The absence of plasma in "spark plasma sintering"," *Journal of Applied Physics*, vol. 104, p. 033305, 2008.

- [54] D. M. Hulbert, A. Anders, J. Andersson, E. J. Lavernia, and A. K. Mukherjee, "A discussion on the absence of plasma in spark plasma sintering," *Scripta Materialia*, vol. 60, pp. 835-838, 2009.
- [55] Z. A. Munir, D. V. Quach, and M. Ohyanagi, "Electric current activation of sintering: a review of the pulsed electric current sintering process," *Journal of the American Ceramic Society*, vol. 94, pp. 1-19, 2011.
- [56] R. M. German, *Liquid phase sintering*: Springer Science & Business Media, 1985.
- [57] M. Balog, K. Sedlackova, P. Zifcak, and J. Janega, "Liquid phase sintering of SiC with rare-earth oxides," *Ceramics- Silikaty*, vol. 49, pp. 259-262, 2005.
- [58] S. Sōmiya, *Advanced technical ceramics*. Tokyo ; San Diego: Academic Press, 1989.
- [59] M. A. Ealey and G. Q. Weaver, "Developmental history and trends for reaction-bonded silicon carbide mirrors," in *SPIE's 1996 International Symposium on Optical Science, Engineering, and Instrumentation*, 1996, pp. 66-72.
- [60] ASTM, "Standard Practice for Measuring Ultrasonic Velocity in Materials," vol. E494-10, ed, 2010.
- [61] ASTM, "Standard Practice for Detection and Evaluation of Discontinuities by the Immersed Pulse-Echo Ultrasonic Method Using Longitudinal Waves," vol. E1001, ed, 2011.
- [62] A. R. Portune, "Nondestructive Ultrasonic Characterization of Armor Grade Silicon Carbide," PhD, Materials Science and Engineering, Rutgers University, 2011.
- [63] S. Bottiglieri, "The Effect of Microstructure in Aluminum Oxide Ceramics on Acoustic Loss Mechanisms," PhD, Materials Science and Engineering, Rutgers University, 2012.
- [64] L. W. Schmerr, *Fundamentals of Ultrasonic Nondestructive Evaluation: A Modeling Approach*: Springer US, 1998.
- [65] N. Jepps and T. Page, "Polytypic transformations in silicon carbide," *Progress in crystal growth and characterization*, vol. 7, pp. 259-307, 1983.
- [66] H. Tanaka, H. N. Yoshimura, S. Otani, Y. Zhou, and M. Toriyama, "Influence of Silica and Aluminum Contents on Sintering of and Grain Growth in 6H-SiC Powders," *Journal of the American Ceramic Society*, vol. 83, pp. 226-28, 2000.
- [67] M. I. Mendelson, "Average Grain Size in Polycrystalline Ceramics," *Journal of the American Ceramic Society*, vol. 52, pp. 443-446, 1969.
- [68] J. B. Wachtman, W. R. Cannon, and M. J. Matthewson, *Mechanical properties of ceramics*: John Wiley & Sons, 2009.
- [69] P. Šajgalík, J. Sedláček, Z. Lenčėš, J. Dusza, and H. T. Lin, "Additive-free hot-pressed silicon carbide ceramics—A material with exceptional mechanical properties," *Journal of the European Ceramic Society*, vol. 36, pp. 1333-1341, 2016.
- [70] R. W. Rice, C. C. Wu, and F. Boichelt, "Hardness–Grain-Size Relations in Ceramics," *Journal of the American ceramic society*, vol. 77, pp. 2539-2553, 1994.